The influence of Hall currents, plasma viscosity and electron inertia on magnetic reconnection solutions

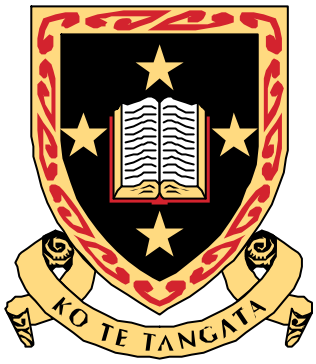

The University of Waikato

Te Whare Wānanga o Waikato

A thesis presented to

The University of Waikato

in fulfilment of the thesis requirements

for the Degree of Doctor of Philosophy

by

Tissa Senanayake

2007

Abstract

This thesis examines magnetic reconnection in the solar corona. Magnetic reconnection is the only mechanism which allows the magnetic topology of magnetized plasmas to be changed. Many of the dynamic processes in the Sun's atmosphere are believed to be driven by magnetic reconnection and studying the behaviour of such phenomena is a key step to understanding the reconnection mechanism. In Chapters 1 to 3, we discuss the physical and mathematical framework on which current magnetohydrodynamic reconnection models are based.

The aim of the thesis is to investigate theoretical models of magnetic reconnection using variety of analytic and numerical techniques within the theoretical frame work of magnetohydrodynamics (MHD).

In Chapter 4 we use a line-tied X-point collapse model for compressible plasmas to investigate the role of viscosity on the energy release mechanism. This model also provides the basis for the investigation of Chapter 5 which explores the impact of Hall currents in the transient X-point energy dissipation.

Chapter 6 is concerned with how reconnection is modified in the presence of generalized Ohm's law which includes both Hall current and electron inertia contributions. In contrast to the "closed" X-point collapse geometry adopted for compressible plasmas previously, we find it more convenient to explore this problem using an "open" incompressible geometry in which plasma is continually entering and exiting the reconnection region. Specially, we find the scaling of the Hall-MHD system size analytically, rather than numerically as in the X-point problem of Chapter 5. Chapter 7 summarizes the results of investigations in Chapters 4, 5 and 6.

Acknowledgements

This thesis would never have reached completion without the help and support of a number of people who I would now like to thank.

Firstly, I would like to express my deepest gratitude and appreciation to my chief supervisor Professor Ian Craig. His insightful comments based on a very wide and deep knowledge about plasma physics and magnetic reconnection has improved my understanding. Without his guidance, none of this would be possible. His invaluable advice during writing and reading of the draft is gratefully acknowledged.

Next I would like to thank my second supervisor Professor Alfred Sneyd for his knowledgeable, expert guidance and advices during the proof reading of the thesis.

I would also like to express my appreciation to the Department of Mathematics for providing me with a good research environment. The supports from all the staff in the department are gratefully acknowledged.

I am particularly grateful to Doctor Yuri Litvinenko, University of New Hampshire, for his contribution to my thesis in his role as a research collaborator.

I must also express my gratitude for the scholarships provided by the University of Waikato and New Zealand Institute of Mathematics and its Applications (NZIMA).

Special gratitude goes to my friends Dr Sivajah Somasundaram and Dr Jacob Heerikhuisen, University of California, Riverside, for their kind support during my thesis works.

Also, special thanks must go to post doctoral fellow David Pontin for general comments and suggestions and assisting with spelling and grammar.

Finally, on the personal level, I would like to give a special mention to my dear wife Mahima for her kind guidance and encouragement to complete this thesis.

Contents

Chapter 1

Introduction

1.1 The solar atmosphere

The Sun is a ball of hot gas made up of roughly 92% hydrogen and 8% Helium. Nuclear reactions taking place within the Sun drive its surface temperature to over $6,000\,K$. Although the light from the Sun seems constant to us, telescopes reveal that the Sun is far from stable. The strong magnetic field associated with Sun causes a number of unexpected phenomena. For example, sunspots are several hundred degrees cooler than the surrounding areas and contain intense magnetic fields. The number of sunspots varies periodically, and this 11-year cycle of solar activity is one of the most mysterious properties of the Sun (Micheel, 1989).

The solar atmosphere, above the surface of the Sun, is divided into three distinct regions (Figure 1.2). The thin layer closest to the surface is known as the photosphere. This region is still relatively dense and emits most of the solar radiation. The chromosphere is a thin layer trapped between the photosphere, and the corona. The layer between the relatively cool ($\simeq 10^4 K$) chromosphere and the hot ($\simeq 10^6 K$) corona is called the transition region. The corona is the outermost atmosphere of the Sun, consisting of highly rarefied gas (Leon & Jay, 1997). A great deal of observational and theoretical effort has been expended in trying to

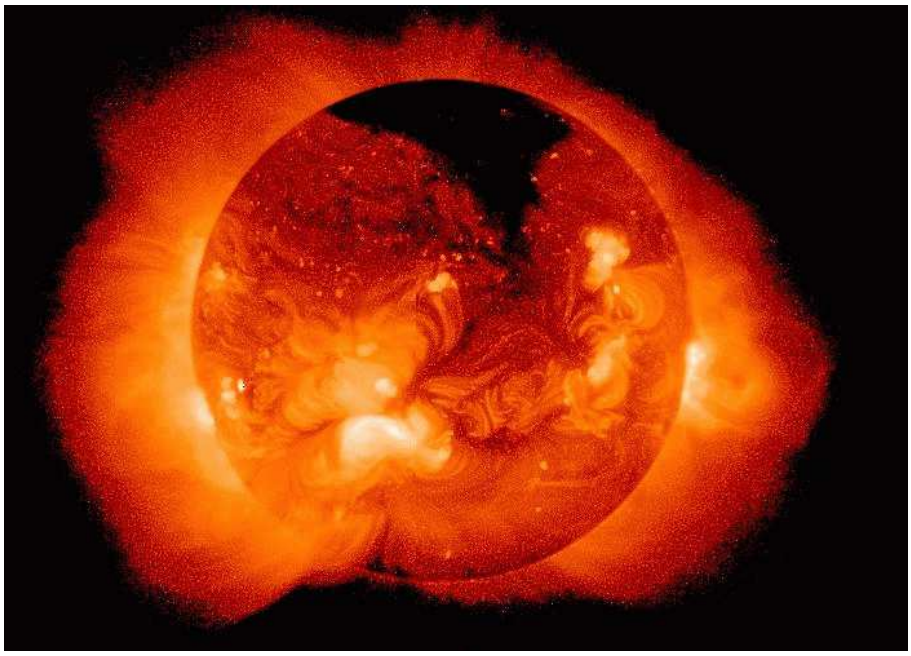

Figure 1.1: A soft X-ray image of the sun taken by the Yohkoh satellite. Reconnection is thought to play a role in coronal heating (Image from http//mrx.pppl.gov/).

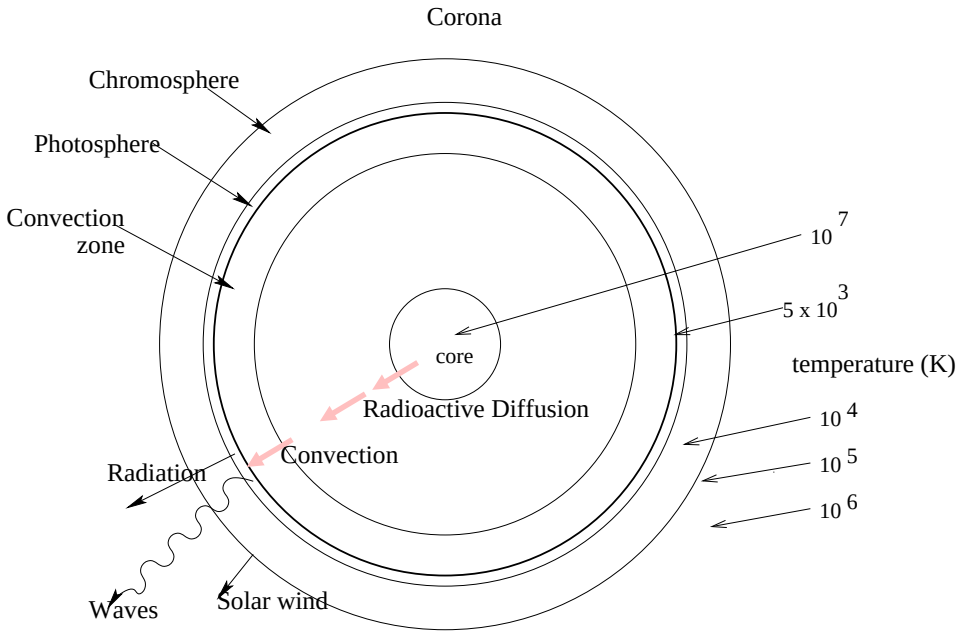

Figure 1.2: The Sun, indicating the size of the different regions and their temperatures (Priest, 1984).

understand the physical nature of coronal plasmas. For example, one can observe large sudden explosions in the corona known as solar flares (see Figure 1.1). A solar flare is thought to occur when magnetic energy, built up slowly in the solar atmosphere, is explosively released within time scales of a few minutes. The satellite data from *Yohkoh* (Bentley & Mariska, 1996) confirm that the length scale of the flare is comparable with the diameter of the Earth (i.e. 10^4km). In a large flare, an energy release of the order of 10^{32} ergs may occur in a hundred seconds. This is the equivalent to a 100-megaton hydrogen bomb exploding over the same time interval. Although astronomers have studied flares for over a century, many aspects of solar flares are still mysterious. In particular, it is difficult to describe how to release a large amount of energy sufficiently fast to explain a flare. Because cosmic plasmas are highly conducting, typical plasmas can release energy only very slowly, over a period of several months rather than a few hundred seconds (Priest & Forbes, 2000).

There are typically three stages to a solar flare. In the first stage (called the *precursor* stage), the release of magnetic energy is triggered, and soft x-rays are emitted. Secondly, there is the *impulsive* stage, where protons and electrons are accelerated to energies exceeding 1 MeV. In this stage, radio waves, hard X-ray, and gamma ray emissions are detected. During the final *decay* stage, decay of soft X-rays can be detected.

Solar flares occur in the corona in areas of strong magnetic field, called "active regions". Sunspots are intimately related to active regions. Both sunspots and X-ray bright coronal regions are caused by the emergence of magnetic fields from inside the Sun. It is now accepted that flare activity is closely associated with magnetic energy in a strong active region field.

It is widely believed that the Sun's magnetic field is generated by an internal magnetic dynamo. The fact that the global magnetic field changes cyclically over eleven years, indicates that the magnetic field is continually generated within the

Sun.

At high temperatures, active regions seem to consist of loops and arches. Soft X-ray images of the corona show that loops have a temperature of $3-5\times10^6K$ with a very small variation (Priest, 1984). This thesis will focus on the issue of heating the corona both in quiescent active regions and flares.

It is interesting that, despite intense investigation, the mechanism by which the corona is heated remains unknown. In 1973, Parker suggested a mechanism for heating closed magnetic loops (Parker, 1973) based on the dissipation of magnetic energy at specialized sites in the corona. To date, Parker's hypothesis remains undecided. Our aim will be to incorporate knowledge of the underlying reconnection mechanism—to be discussed in subsequent chapters—into a theoretical model, which predicts event parameters such as the relationship between "build-up" time, and flare energy decay. A mathematical description of established reconnection mechanisms will be discussed in Chapter 3.

Solar coronal plasma is highly conducting, and this very low electrical resistivity creates difficulties when we attempt to solve the physical equations of the system. The low resistivity makes it difficult to release energy quickly through the reconnection process. Reconnection is essentially a topological restructuring of the magnetic field causing a change in the connectivity of its field lines. Our main problem is, given that the resistivity is very small, how can we rapidly change the topological structure and liberate excess magnetic energy in the plasma?

Magnetic reconnection has been invoked to explain astrophysical phenomena such as solar flares since the 1940s. Figure 1.3 shows the process of magnetic reconnection, first suggested by Giovanelli (1946) and Hoyle (1949), that magnetic X-type null points can serve as locations for plasma heating in solar flares. Field lines are pushed together by fluid motions in the horizontal direction and repeatedly "cut" and "rejoined" at the neutral point. Field lines have both tension and pressure asso-

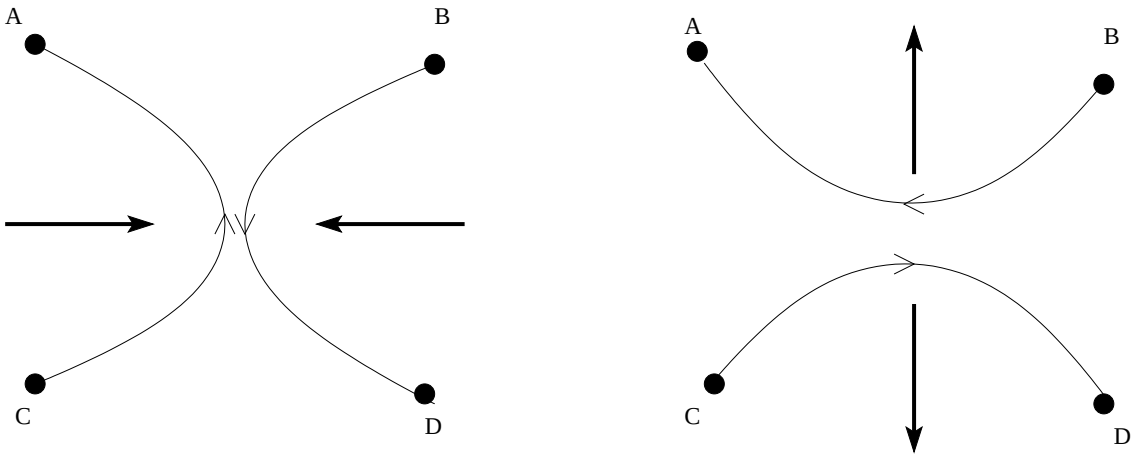

Figure 1.3: The left figure represents the initial magnetic field in which two antiparallel magnetic field lines are pushed together and reconnected. The right figure shows reconnected field line pulls them a part and changes the topology.

ciated with them. In particular, field lines rejoined at the neutral point "spray out" in the outflow direction, providing a magnetic sling shot and transferring magnetic energy into the kinetic energy of mass motion. X-point configurations such as this form the basis of most reconnection models.

Carrying out a full mathematical analysis of magnetic reconnection is extremely difficult. As described in Chapter 3 early reconnection models such as the Sweet-Parker model, were steady-state time independent descriptions. Their goal was to develop a simple magnetohydrodynamic (MHD) model for reconnection in a current sheet formed at a null point. By contrast current reconnection models tend to be time dependent. They attempt to describe the observed rapid variation associated with flare emission in the solar corona.

Traditionally, reconnection solutions have been developed using a simplified collisional resistive form of Ohm's law. These models may allow a more rapid energy dissipation rate by reducing the effective dissipation length-scale. A key aim of the present study is to investigate how various effects—Hall currents, electron inertia

and finite viscosity—influence reconnection solutions in "closed", line-tied X-point geometries. However in later chapters, we will also consider reconnection in "open" geometries, where plasma is free to enter and leave the reconnection site. A discussion of reconnection in open and closed geometries is given in Chapter 3.

1.2 Thesis overview

As already explained, understanding the solar flare mechanism with resistive, Hall, inertial and viscous effects is the prime aim of this thesis. We do this by invoking an Ohm's law that includes Hall current and plasma inertial contributions. We also perform an analysis of the effects of viscous dissipation—an effect that missing from most previous studies.

In the following chapter, we introduce the MHD equations with the effects of the Hall current, electron inertia and viscosity included. Maxwell's equations for an electric field $\mathbf{E}$ and magnetic field $\mathbf{B}$ are introduced . These equations are then non-dimensionalized by scaling all the quantities with respect to typical coronal parameters.

The original studies of steady state models, specifically Parker (1957), Sweet (1958), Petschek (1964), Syrovatskii (1971), Sonnerup & Priest (1975) and Craig & Henton (1995) are reviewed in the first half of Chapter 3. Next, studies of time-dependent X-point collapse are reviewed particularly with regard to the reconnection rate and its underling eigenfunction description.

The original work in this thesis is contained in Chapters 4, 5 and 6. The purpose of Chapter 4 is to demonstrate that the viscosity can indeed have a profound effect on the dynamics of magnetic reconnection at magnetic X-points. The dissipation of the kinetic and magnetic energy in the plasma is examined. This leads to the demonstration of a new phenomena, involving visco-resistive coupling, which could be important in the general context of coronal energy dissipation.

Models for the X-type reconnection problem are developed using a generalized version of Ohm's law in Chapter 5, which includes collisionless quantities such as Hall currents. In particular, we will examine the impact of Hall current effects on magnetic reconnection solutions.

Chapter 6 investigates the transient merging solution of incompressible plasmas with Hall currents, as well as inertial effects, by performing numerical merging simulations in an "open" geometry. Although electron inertial effects are neglected in traditional magnetic reconnection models, we will find analytical and computational evidence that inertial effects are important for plasma resistivities typical of the solar corona.

Finally, in Chapter 7, we summarize the main conclusions of the work in this thesis, and discuss possible applications and extensions. Note that all the results presented in Chapters 4, 5 and 6 have been computed by the present author using specialized codes described in Appendix A and B.

Chapter 2

Magnetohydrodynamic equations

In this chapter we consider equations that describe the effects of magnetic and electric fields on the behavior of partially ionized gases (plasmas). The resulting specialization of the collision-dominated fluid equations are called the magneto-hydrodynamic (MHD) equations. In what follows the MHD equations are non-dimensionalized, and some of their properties explored. We will discuss a relation, referred to as the "Generalized Ohm's Law", which describes how a current flows in a gas in response to electric and magnetic fields. We will also investigate the influence of plasma viscosity as well as Hall current and electron inertial effects.

The equations derived in this chapter will provide the theoretical framework for the reconnection models described in the remainder of this thesis.

2.1 Properties of solar plasma

Although early reconnection models were developed using a simplified "collisional resistive" form of Ohm's law, reconnection often occurs in collisionless plasmas. Therefore when we derive the MHD equations for the solar plasma, it is important to know the key parameters of the plasma. Table 2.1 gives us some typical coronal values based on cgs units (short for centimeter-gram-second).

Magnetic field	$B_c = 10^2\,\mathrm{G}$
Length	$l_c = 10^{9.5}\,\mathrm{cm}$
Number density	$n_c = 10^9\,\mathrm{cm}^{-3}$
Corona temperature	$T_c = 10^6\,\mathrm{K}$
Alfvén speed	$v_A = B_c/\sqrt{4\pi\rho_c} = 10^9\,\mathrm{cms}^{-1}$
Alfvén time	$\tau_A = l_c/v_A \simeq 3\,\mathrm{s}$
Coulomb logarithm	$\ln\Lambda = 19$
Electron thermal speed	$v_{T_e} = 3.9 \times 10^8\,\mathrm{cms}^{-1}$
Proton thermal speed	$v_{T_p} = 1 \times 10^7\,\mathrm{cms}^{-1}$
Mean free path	$\lambda = 5.6 \times 10^6\,\mathrm{cm}$
Proton plasma frequency	$\nu_p = 4.15 \times 10^7\,\mathrm{rads}^{-1}$
Electron plasma frequency	$\nu_e = 1.8 \times 10^9\,\mathrm{rads}^{-1}$
Kinematic proton viscosity	$\nu = 10^{-4.5}\,\mathrm{cm}^2\mathrm{s}^{-1}$

Table 2.1: Some physical properties of the solar coronal plasma.

The mean free path of the particles—the average distance moved between successive collisions—is one important parameter of the solar plasma. The electric field accelerates particles along the magnetic field, with protons and electrons going in opposite directions. Collisions between electrons and protons occur at a rate which depends on the density and temperature of the plasma. The electron thermal speed and the proton thermal speed in a Maxwellian plasma are given by

$$v_{Te} = \left(\frac{k_B T_e}{m_e}\right)^{1/2}, \quad v_{Tp} = \left(\frac{k_B T_p}{m_p}\right)^{1/2}, \tag{2.1}$$

where m_s is mass and T_s is temperature for species s and k_B is the Boltztmann constant. The formula

$$\lambda = 3(2\pi)^{3/2}\frac{(k_B T_e)^2}{ne^4 \ln\Lambda} \text{ cm} \tag{2.2}$$

(e.g. Priest & Forbes, 2000) is the mean-free path for electron-proton collisions. Here n is number density of electrons, and $\ln\Lambda$ the Coulomb logarithm. As λ increases, the diffusion caused by collisions becomes less effective.

Consider the typical coronal parameters of Table (2.1). These give the electron thermal speed as $v_{T_e} \simeq 3.9 \times 10^8\,\mathrm{cm\,s^{-1}}$, the proton thermal speed as $v_{T_p} \simeq 1 \times 10^7\,\mathrm{cm\,s^{-1}}$ and the mean free path as $\lambda \simeq 5.6 \times 10^6$ cm. The electron-proton collision time, $\tau_c = \lambda / v_{T_p}$ is approximately one second so the electron-proton collision frequency

$$\nu_{ep} = \frac{v_{T_p}}{\lambda} \text{ s}^{-1} \tag{2.3}$$

is also of order one. The Ohmic resistivity is proportional to the electron-proton plasma frequency. The parameter λ/l_c is a measure of the plasma collisionality. This parameter for coronal plasma is therefore of order $10^{-2.5}$ which means that the solar corona is weakly collisional. More generally, when temperatures are enhanced, say in a solar flare, λ increases and the plasma may be effectively collisionless. Thus, we can be confident that Hall current and electron inertial effects should be included in solar flare models.

2.2 Governing equations

As discussed in Chapter 1, it is widely accepted that solar flares are initiated by the rapid collapse of magnetic fields in the solar corona. The MHD equations deal with the motion of an electrically conducting fluid in the presence of a magnetic field. The motion of conducting material across the magnetic field creates an electric field that causes an electric current to flow. This leads to a force acting on the plasma, the so-called Lorentz force, which influences the fluid flow.

Maxwell's equations for an electric field $\mathbf{E}$ and magnetic field $\mathbf{B}$, provide the basic equations of MHD. In addition we require continuity equations and momentum equations for two plasma species: electron (e) and proton (p). Viscosity is introduced into the proton momentum equation as viscous effects will be a major focus of the reconnection problem discussed in Chapter 4 . Then, assuming the electron density is equal to the proton density, we derive the single fluid equations with a generalized Ohm's law which includes the Hall current and electron inertial effects. Finally we non-dimensionalize all parameters with respect to typical coronal values.

2.2.1 Maxwell's equations

In the cgs units system, Maxwell's equations take the following form:

$$\nabla \cdot \mathbf{E} = 4\pi\bar{q}, \tag{2.4}$$

$$\nabla \cdot \mathbf{B} = 0, \tag{2.5}$$

$$\frac{4\pi}{c}\mathbf{J} + \frac{1}{c}\frac{\partial \mathbf{E}}{\partial t} = \nabla \times \mathbf{B}, \tag{2.6}$$

$$\frac{\partial \mathbf{B}}{\partial t} = -c\,\nabla \times \mathbf{E}. \tag{2.7}$$

The four equations express, how electric charges produce electric fields (2.4); the experimental absence of magnetic monopoles (2.5); how currents and changing electric fields produce magnetic fields—the Ampere-Maxwell law (2.6); and how changing

Symbol	Meaning
$\mathbf{E}$	electric field
$\mathbf{B}$	magnetic field
c	speed of light in a vacuum
$\mathbf{J}$	current density
$\bar{q}$	electric charge density
$\nabla\cdot$	the divergence operator
$\nabla\times$	the curl operator

Table 2.2: The meaning of symbols presented in Maxwell's equations.

magnetic fields produce electric fields—Faraday's law of induction (2.7). Table (2.2) provides the meaning of each symbol. In MHD the displacement current $\partial\mathbf{E}/\partial t$, from the left hand side of the equation (2.6) is generally ignored on the grounds that the time scale of the variation in the field is long compared with l_c/c, where l_c is length scale of the system. Hence the current density is given by

$$\mathbf{J} = \frac{c}{4\pi}\nabla \times \mathbf{B}. \tag{2.8}$$

In the rest of this section, the generalized form of Ohm's law will be established to formulate Hall current and electron inertial effects. The viscosity term which has been omitted in many previous studies (e.g. Cravens, 1997) will also be included in the proton momentum equation. We shall however, consider only the isotropic shear viscosity, which neglects the bulk viscosity and the influence of stratifications introduced by a strong magnetic field (Braginskii, 1965).

2.2.2 Two-fluid plasma

We introduce the compressible two-fluid MHD equations by considering the plasma to consist of two species: electrons of mass m_e and charge $-e$, and protons of mass

m_p and charge $+e$. The continuity equations for electrons and protons are given by

$$\frac{\partial n_e}{\partial t} + \nabla \cdot (n_e \mathbf{v}_e) = 0, \tag{2.9}$$

and

$$\frac{\partial n_p}{\partial t} + \nabla \cdot (n_p \mathbf{v}_p) = 0, \tag{2.10}$$

where $n_e, n_p, \mathbf{v}_e, \mathbf{v}_p$ are number density and flow velocity respectively for species e and p. The respective mass densities can be expressed as $\rho_e = m_e n_e$ and $\rho_p = m_p n_p$. Applying the momentum conservation law (e.g. Cravens, 1997) for electrons and protons, the electron and proton momentum equations are given by

$$n_e m_e \left[\frac{\partial}{\partial t} + \mathbf{v}_e \cdot \nabla\right] \mathbf{v}_e = -n_e e[\mathbf{E} + \frac{1}{c}\mathbf{v}_e \times \mathbf{B}] - \frac{1}{c}\nabla p_e + n_e m_e \mathbf{g} - \sum_{t \neq e} n_e m_e \nu_{et}(\mathbf{v}_e - \mathbf{v}_t)$$
$$+ n_e m_e \nu_e \left[\nabla^2 \mathbf{v}_e + \frac{1}{3}\nabla(\nabla \cdot \mathbf{v}_e)\right] \tag{2.11}$$

and

$$n_p m_p \left[\frac{\partial}{\partial t} + \mathbf{v}_p \cdot \nabla\right] \mathbf{v}_p = +n_p e[\mathbf{E} + \frac{1}{c}\mathbf{v}_p \times \mathbf{B}] - \frac{1}{c}\nabla p_p + n_p m_p \mathbf{g} - \sum_{t \neq p} n_p m_p \nu_{pt}(\mathbf{v}_p - \mathbf{v}_t)$$
$$+ n_p m_p \nu_p \left[\nabla^2 \mathbf{v}_p + \frac{1}{3}\nabla(\nabla \cdot \mathbf{v}_p)\right], \tag{2.12}$$

where $\mathbf{g}$ is the acceleration due to gravity, e is the charge of the electron, and ν_{st} is the effective momentum transfer collision frequency between species s and t. The symbol ν_s is the classical "gas dynamic" form of the kinematic shear viscosity for species s (Priest & Forbes, 2000). The p_e and p_p are electron and proton gas pressures respectively. Here, p is isotropic, but more generally, the pressure term is $\nabla \cdot \mathbf{p}_s$ where, $\mathbf{p}_s$ is the pressure tensor associated with each species. Bhattacharjee, Ma and Wang (1999) simplified the $\nabla \cdot \mathbf{p}_e$ as ∇p_e by treating the electron stress tensor $\mathbf{p}_e$ as isotropic and diagonal. This simplification is accurate only for a collision dominated, Maxwellian plasma.

The five terms on the right hand side of (2.11 & 2.12) represent the electric, pressure, gravity, friction and viscous forces for species e and p respectively. The

"frictional" term includes a sum over all species but does not include self-collisions (i.e.,$s \neq t$).

The electron viscosity terms will be neglected (see §2.2.3 for our studies of reconnection models) but electron viscosity can dominate ion viscosity under the right set of plasma conditions (Whitney et al., 2006). For example, Velikovich et al. (2001) show that the electron viscosity substantially affects the structure of strong shock waves in a fully ionized plasma.

So far we have been using equations which treat the electron and proton gas separately. A useful simplification can be made combining the electron and proton equations to obtain a "single fluid" plasma equation.

2.2.3 The single-fluid equations and generalized Ohm's law

An electric field, $\mathbf{E}$ is created in the plasma when the electrons and protons are separated. We are dealing with a plasma in which $l_c > \lambda$ (see §2.1), so that the plasma is quasi-neutral on scales $l >> \lambda$. It follows that the region contains an almost equal numbers of electrons and protons and hence net charge imbalance can be ignored:

$$n_e \simeq n_p = n. \tag{2.13}$$

One consequence of (2.13) is that we do not need separate continuity equations for the electron and proton gases; a single continuity equation suffices. The viscosity of plasma is due primarily to protons while viscous effects due to the electrons are generally negligible (Spitzer, 1962).

Solving equation (2.11) for $\mathbf{E}$, and neglecting the effects of electron viscosity, we obtain a form of "generalized Ohm's law," namely

$$\mathbf{E} = -\frac{1}{c}\mathbf{v}_e \times \mathbf{B} - \frac{1}{nec}\nabla p_e + \frac{m_e}{ne}\mathbf{g} - \frac{m_e}{e}\nu_{ep}(\mathbf{v}_e - \mathbf{v}_p) - \frac{m_e}{e}\left[\frac{\partial \mathbf{v}_e}{\partial t} + \mathbf{v}_e \cdot \nabla \mathbf{v}_e\right], \tag{2.14}$$

where $\nu_{ep} = 1/\tau_c$ (see 2.3) is the electron-proton Coulomb collision frequency and τ_c

is the collision time. Equation (2.14) specifies the electric field required to maintain quasi-neutrality in a plasma due to electron-proton collisions. The electric field given by (2.14) is written in terms of $\mathbf{v}_e$, but we really need it in terms of the variables $\mathbf{v}$ and $\mathbf{J}$ where $\mathbf{v}$ is the flow velocity of the center of mass and $\mathbf{J}$ is current density. The velocity of the center of mass is given by

$$\mathbf{v} = \frac{m_e\mathbf{v}_e + m_p\mathbf{v}_p}{m_e + m_p} \simeq \mathbf{v}_p \tag{2.15}$$

since $m_e/m_p << 1$. The definition of the current density for a single ion species is given by

$$\mathbf{J} = ne(\mathbf{v}_p - \mathbf{v_e}). \tag{2.16}$$

Substituting (2.15) and (2.16) into (2.14) and ignoring the gravitational force, we convert (2.14) into a form which involves $\mathbf{v}$ and $\mathbf{J}$

$$\mathbf{E} = -\frac{1}{c}\mathbf{v}\times\mathbf{B} + \frac{1}{nec}(\mathbf{J}\times\mathbf{B} - \nabla p_e) + \frac{m_e\nu_{ep}}{ne^2}\mathbf{J} + \frac{m_e}{ne^2}\left\{\frac{\partial\mathbf{J}}{\partial t} + \nabla\cdot[\mathbf{Jv} + \mathbf{vJ}]\right\}. \tag{2.17}$$

This is the generalized Ohm's law we shall employ in this thesis. We will refer to the five terms on the right hand side of (2.17) as motional, Hall, ambipolar, resistive and electron inertia terms respectively. The Ohmic resistivity is given by

$$\bar{\eta} = \frac{m_e\nu_{ep}}{ne^2} = \frac{1}{\sigma} \tag{2.18}$$

where $\sigma \simeq 10^7\, T^{3/2}$ cgs is the collisional conductivity (Spitzer, 1962). The discussion and application of the generalized Ohm's law for plasma can be found for example in Bhattacharjee, Ma & Wang (1999), Priest & Forbes (2000) and Craig & Watson (2003). The aim of these studies was to investigate Hall current effects rather than electron inertial effects because the electron inertia term is typically small relative to other terms in equation (2.17). Combining equations (2.17) and (2.7), we obtain the induction equation,

$$\frac{\partial\mathbf{B}}{\partial t} = \nabla\times(\mathbf{v}\times\mathbf{B}) - \bar{\eta}\, c\nabla\times\mathbf{J} - \bar{d}_i\nabla\times(\mathbf{J}\times\mathbf{B} - \nabla p_e) - \bar{d}_e\nabla\times\left(\frac{\partial\mathbf{J}}{\partial t} + \nabla\cdot[\mathbf{Jv} + \mathbf{vJ}]\right), \tag{2.19}$$

where

$$\bar{d}_i = \frac{1}{ne}, \quad \bar{d}_e = \frac{m_e c}{ne^2},$$

define Hall term and electron inertia term respectively. The single-fluid mass continuity equation is found by mass-weighting the electron (2.9) and proton (2.10) continuity equations,

$$\frac{\partial \rho}{\partial t} + \nabla \cdot (\rho \mathbf{v}) = 0. \tag{2.20}$$

Now we derive the single-fluid momentum equation by adding together the electron (2.11) and (2.12) proton momentum equations. The electric field ($\mathbf{E}$) cancels during this operation (i.e $n_p \simeq n_e$). Also the electron viscosity term has been neglected. Then we have

$$\rho \frac{D\mathbf{v}}{Dt} = -\frac{1}{c}\nabla p + \frac{1}{c}\mathbf{J} \times \mathbf{B} + \bar{\nu}\left\{\nabla^2 \mathbf{v} + \frac{1}{3}\nabla(\nabla \cdot \mathbf{v})\right\}, \tag{2.21}$$

where $D/Dt = (\partial/\partial t + \mathbf{v}.\nabla)$ is the advective derivative, $\rho = nm_p$ is mass density, $p = p_e + p_p$ is total thermal pressure and $\bar{\nu} = \nu_p$. Here

$$\nu_p = 2.21 \times 10^{-15} \frac{T^{5/2}}{\ln \Lambda} \ \mathrm{cm^2 s^{-1}} \tag{2.22}$$

is the proton kinematic viscosity of the plasma (Spitzer, 1962).

2.2.4 Non-dimensionalisation

It is very convenient to work with a non-dimensional form of the above equations. We non-dimensionalize with respect to the following typical coronal values of Table (2.1), namely $B_c \simeq 10^2 \mathrm{G}$, $l_c \simeq 10^{9.5}\,\mathrm{cm}$, $n_c \simeq 10^9\,\mathrm{cm^{-3}}$, $T = 10^6\,\mathrm{K}$. The Alfvén speed and the Alfvén time are given by

$$v_A = \frac{B_c}{\sqrt{4\pi\rho_c}} \simeq 10^9 \mathrm{cms^{-1}}, \tag{2.23}$$

$$\tau_A = \frac{l_c}{v_A} \simeq 3s, \tag{2.24}$$

where the plasma mass density ρ_c corresponds to a number density of n_c, and these are used to define speeds and times respectively.

The non-dimensional equations of generalized MHD are the continuity equation (2.20),

$$\frac{\partial \rho}{\partial t} + \nabla \cdot (\rho \mathbf{v}) = 0, \tag{2.25}$$

the momentum equation (2.21),

$$\rho \left(\frac{\partial \mathbf{v}}{\partial t} + (\mathbf{v} \cdot \nabla)\mathbf{v} \right) = -\nabla p + \mathbf{J} \times \mathbf{B} + \nu \left[\nabla^2 \mathbf{v} + \frac{1}{3} \nabla (\nabla \cdot \mathbf{v}) \right], \tag{2.26}$$

and the induction equation (2.19),

$$\frac{\partial \mathbf{B}}{\partial t} = \nabla \times (\mathbf{v} \times \mathbf{B}) - \eta \nabla \times \mathbf{J} - d_i \nabla \times (\mathbf{J} \times \mathbf{B} - \nabla p_e) - d_e \nabla \times \left(\frac{\partial \mathbf{J}}{\partial t} + \nabla \cdot [\mathbf{J}\mathbf{v} + \mathbf{v}\mathbf{J}] \right). \tag{2.27}$$

Note also that

$$\mathbf{J} = \nabla \times \mathbf{B}, \quad \nabla \cdot \mathbf{B} = 0. \tag{2.28}$$

According to the our dimensionless units

$$d_i = \frac{c}{l_c \, \omega_{pi}} \simeq 10^{-6.5}, \quad d_e = \left(\frac{c}{l_c \, \omega_{pe}} \right)^2 \simeq 10^{-16} \tag{2.29}$$

where $\omega_{pi} = \sqrt{4\pi n e^2 / m_p}$ and $\omega_{pe} = \sqrt{4\pi n e^2 / m_e}$ are the proton and electron plasma frequencies respectively (Table 2.1). The forcing terms in the momentum equation (2.26) describe respectively, "gas pressure", "Lorentz" and viscous damping of the plasma. Dimensionless dissipation coefficients ν and η are given by

$$\nu = \frac{\nu_p}{\rho v_A l_c}, \qquad \eta = \frac{c^2}{4\pi \sigma l_c v_A} \tag{2.30}$$

where ν is an inverse Reynolds number (viscosity), and η is an inverse Lundquist number (resistivity) for the plasma. Alternatively

$$\nu \equiv \frac{\tau_A}{\tau_\nu}, \quad \eta \equiv \frac{\tau_A}{\tau_\eta} \tag{2.31}$$

where τ_ν is the global viscous diffusion time-scale and τ_η is the resistive diffusion time-scale of the background plasma. Adopting the coronal values given in Table 2.1

and assuming a temperature of 10^6 K, gives the values the viscosity and resistivity of plasma $\nu \simeq 10^{-4.5}$ and $\eta \simeq 10^{-14.5}$ respectively (Spitzer, 1962). These small numbers indicate that steep gradients must develop in the magnetic and velocity fields if significant dissipation is to occur. It also suggests that viscous effects can be of paramount importance in flare-related reconnection, given that $\nu \gg \eta$ (Hollweg, 1986).

2.2.5 Ohmic and viscous dissipation rates

The energy stored in the magnetic field may provide a source of heating, either *via* Ohmic dissipation in regions where electric currents are strong, or viscous dissipation where fluid vorticities are strong. The Ohmic dissipation rate is given by

$$W_\eta = \eta \int_v J^2 dV. \tag{2.32}$$

For the viscous dissipation rate we have

$$W_\nu = \nu \int_v \Omega^2 dV \tag{2.33}$$

where

$$\Omega = \nabla \times \mathbf{v} \tag{2.34}$$

is the vorticity of the fluid plasma and V the plasma volume. Since $\nu >> \eta$, significant viscous dissipation may be easier to achieve than significant Ohmic dissipation. In any case, since η is small, very large current densities are required to make W_η significant (that is approaching order unity).

The magnetic reconnection models described in the next chapter, give two distinct classes of solutions, called "fast" and "slow" reconnection, based on whether the Ohmic dissipation rate scales as a positive or negative power of η. If the Ohmic dissipation rate $W_\eta \sim \eta^k$, where $k \leq 0$, we say that a solution represents fast dissipation. All other solutions are categorized as "slow".

The rate of reconnection is a key issue in most magnetic merging models. In two dimensions, (with $\hat{\mathbf{z}}$ ignorable) the rate of reconnection can be defined quite simply as the rate which field lines move through a magnetic neutral point. Writing $\mathbf{B}$ in terms of the planar flux function $\psi = \psi(x, y)$ so that $\mathbf{B} = \nabla\psi \times \hat{\mathbf{z}}$ the flux transfer rate (or reconnection rate) is given by

$$\frac{\partial \psi}{\partial t} = -\eta J_0 \tag{2.35}$$

at the neutral point. In the next chapter we provide a summary of these reconnection models and investigate their properties. We will see in Chapters 3 and 4, that both the reconnection rate and dissipation rate can in some circumstances be largely independent of the electrical resistivity.

2.3 Summary

In this chapter we have given only a brief summary of the MHD equations. More detailed derivations can be found in many publications (e.g. Roberts, 1967; Priest & Forbes, 2000). We have however described generalized MHD equations which include Hall currents, electron inertia and viscosity. In the chapter that follow we will discuss traditional MHD merging solutions that depend only on the classical resistive form of Ohm's law. Our aim is to investigate how these solutions are affected by the introduction of a generalized Ohm's law as well as viscous effects. The non-dimensionalized equations of the present chapter, namely (2.26-2.27), will provide the basic framework for all these investigations.

Chapter 3

Flare reconnection models

3.1 Introduction

Flare reconnection models are studied in this chapter. Our aim is to set the scene for the development of reconnection solutions in the remainder of this thesis by highlighting the strengths and weaknesses of historical reconnection models. In particular, we examine steady state reconnection models, typified by the classical Sweet–Parker (1958) merging solution, as well as transient solutions associated with X-point collapse.

There are many approximations that are commonly used in early reconnection models. For example, the solutions discussed in §3.2, are both incompressible and steady state. The classical Sweet–Parker model, for instance, assumes an "open" geometry in which plasma, entering the reconnection region, is expelled along the current sheet. In §3.3 we look at theories for time-dependent reconnection, based on X-point collapse models for compressible plasmas, which provide new perspectives on the merging problem. In this thesis, we find it convenient to use both approaches in order to study reconnection in the presence of resistive, Hall current, electron inertial and viscous effects.

3.2 Steady state reconnection

We first discuss the Sweet-Parker current sheet model (Sweet,1958a, 1958b and Parker, 1957, 1963), Petschek's mechanism (Petschek, 1964), the Syrovatskii solution (Syrovatskii, 1971) and the Sonnerup & Priest annihilation solution (Sonnerup & Priest, 1975). We then go on to discuss the more recent exact reconnection solution of Craig & Henton (1995), which includes the Sonnerup & Priest annihilation model as a special case. The construction of velocity and magnetic fields in the transient merging solutions developed in Chapter 6, is based on the Craig & Henton model.

3.2.1 History of steady-state models

In a plasma with finite resistivity, magnetic reconnection can convert magnetic energy into kinetic energy and heat. Early researchers tried to explain the mechanism underlying the breaking and rejoining of field lines and to quantify the rate at which the reconnection occurs. Sweet (1958a, 1958b) and Parker (1957, 1963) put forward a reconnection model that consisted of a simple diffusion region sandwiched between oppositely directed magnetic fields (§3.2.3). A resistive current layer is then present along the whole boundary between the opposing magnetic fields. In this region the field lines may diffuse, break and reconnect (see Figure 1.3 in Chapter 1). The length, L, of the diffusion layer is therefore associated with the global length-scale of the plasma and the reconnection rate is equal to the speed at which field lines are swept by the flow into the diffusion region (see (2.35) in Chapter 2). Unfortunately the reconnection rate of the Sweet-Parker model is much too slow to explain the energy release in solar flare. Accordingly, many other researchers have sought to develop models that enhance the reconnection rate.

A key development was provided by Petschek (1963). Petschek suggested that the Sweet-Parker model would reconnect faster if the diffusion region were shorter

and thinner. According to Petschek, this could be accomplished by standing, slow-mode MHD shocks propagating from the diffusion region. The shock waves were the main sites of energy conversion, with the inflow magnetic energy being converted to the heat and kinetic energy. For the next few years Petschek's mechanism—despite some questionable analytic assumptions—was widely accepted as the answer to fast flare energy release. However, Sonnerup (1970) suggested an alternative reconnection model that could operate at any rate up to the Alfvén speed, while Sonnerup & Priest (1975) managed to formulate an exact solution to resistive merging that modeled the magnetic annihilation of straight field lines. Their solution requires a stagnation point flow coupled with a one-dimensional anti-parallel magnetic field. The Sonnerup & Priest solution has now been recognized as a special case of a more general family of reconnection solutions (Craig & Henton, 1995). Unlike the previous reconnection models, the Craig & Henton approach is based on an exact analytic solution of the momentum and induction equations.

The Craig & Henton solution has recently been extended in several ways. For example, Fabling & Craig (1996) included viscosity, Craig et al. (1997) extended it to a three-dimensional sheared stagnation-point flow and were therefore able to model the "fan reconnection" regime discussed kinematically by Priest and Titov (1996). In a similar way, Craig & Fabling (1996) have discovered solutions for 3D "spine reconnection" which allows reconnection via quasi-cylindrical current tubes. Of interest to the present study is the fact that the generalized Ohm's law can be incorporated in this broad class of exact 2D and 3D reconnection solutions. Here we consider only the simplest, steady-state planar solution of Craig & Henton (1995). However, this solution is generalized in Chapter 6 to include the Hall current and electron inertial effects in transient merging solutions.

3.2.2 The steady-state MHD equations

The solutions outlined above are based on the steady-state, resistive MHD equations for an incompressible plasma. Taking $\nabla \cdot \mathbf{v} = 0$ and setting $\rho = 1$, we note that the dimensionless induction equation reduces to

$$\mathbf{E} + \mathbf{v} \times \mathbf{B} = \eta \mathbf{J}, \qquad \mathbf{J} = \nabla \times \mathbf{B}, \tag{3.1}$$

where $\mathbf{E}$ is an uniform electric field which we take to the aligned normal to the (x, y) plane. We must also include the steady-state momentum equation (2.26) in the absence of viscosity,

$$(\mathbf{v} \cdot \nabla)\mathbf{v} = -\nabla p + \mathbf{J} \times \mathbf{B}. \tag{3.2}$$

The assumption is now made that reconnection occurs when oppositely directed magnetic field lines are driven together by an externally imposed flow. In particular, there is an advection region where ηJ is negligible, in which the field is "frozen into" the plasma. Diffusion of the field then occurs only in a narrow current layer where the inflow velocity is small and according to (3.1), $\mathbf{E} \simeq \eta \mathbf{J}$.

3.2.3 Sweet-Parker model

As already mentioned, the Sweet-Parker model consists of a simple diffusion region of length $2L$ and width $2l$, sandwiched between oppositely directed magnetic fields (Figure 3.1). The basic Sweet-Parker model (Sweet 1958, Parker 1957, 1963) has an outflow speed (v) equal to the Alfv́en speed (v_A) and the length of the diffusion region is of order the global length-scale L. Mass conservation implies

$$Lu = lv, \tag{3.3}$$

where u is inflow speed. The assumption that $\mathbf{E} = E\,\hat{\mathbf{z}}$ in (3.1) implies that $uB \sim \eta J$, so that field lines move with speed

$$u = \frac{\eta}{l} \tag{3.4}$$

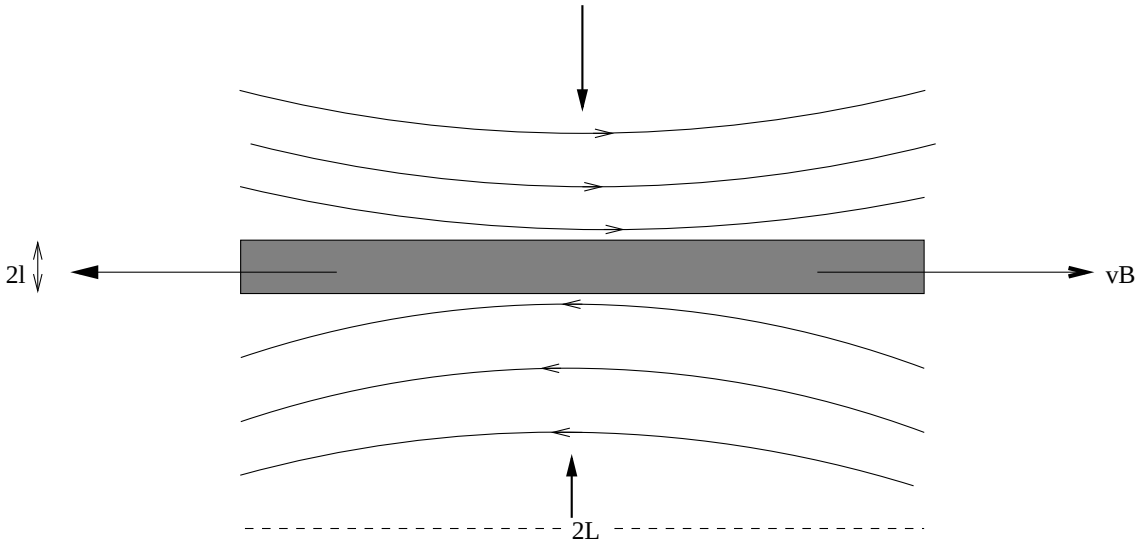

Figure 3.1: Sketch of the Sweet-Parker reconnection. The anti-parallel magnetic field reconnects in the shaded region with length $2L$ and width $2l$ which depends on the resistivity η.

into the diffusion region. Here we have used the approximation $J \sim B/l$. Along the inflow axis (3.2) gives

$$\frac{d}{dy}\left(\frac{1}{2}u^2 + p + \frac{1}{2}B_x^2\right) = 0, \tag{3.5}$$

while along the outflow axis it implies

$$\frac{d}{dx}\left(\frac{1}{2}v^2 + p + \frac{1}{2}B_y^2\right) = 0. \tag{3.6}$$

Integrating the above equations and putting $p = p_0,\ v = u = B_x = 0$, and $B_y = 0$ at the origin, we have

$$p_0 - p_{in} = \frac{1}{2}u^2 + \frac{1}{2}B_{in}^2 \tag{3.7}$$

$$p_0 - p_{out} = \frac{1}{2}v^2 + \frac{1}{2}B_{out}^2 \tag{3.8}$$

where $B_{in} = O(1)$ is global magnetic field, while p_{in} and p_{out} are inflow and outflow pressures respectively. Eliminating l from equations (3.3) and (3.4), we obtain the square of the inflow speed

$$u^2 = \frac{\eta v}{L}. \tag{3.9}$$

The inequality $u << v$ follows from the fact that $\eta << 1$ in the plasma, remembering that $L = O(1)$. Similarly, conservation of magnetic flux namely,

$$vB_{out} = uB_{in},$$

implies $B_{out} << B_{in}$. According to the above inequalities, the quantities u and B_{out} in (3.7) & (3.8) are very small compared to the other values. Hence we have

$$p_0 \simeq v^2/2, \quad v \simeq B_{in}. \tag{3.10}$$

Substituting these results into equation (3.3) yields

$$l \sim \frac{uL}{B_{in}}. \tag{3.11}$$

Remembering that L and B_{in} are both by hypothesis order unity, (3.11) and (3.4) imply that

$$l \sim \eta^{1/2}, \qquad u \sim \eta^{1/2}. \tag{3.12}$$

It follows that corresponding Ohmic dissipation rate W_η and current density scale as

$$W_\eta \sim \eta^{1/2}, \quad J \sim \eta^{-1/2}. \tag{3.13}$$

These scalings confirm that the Sweet-Parker model allows only a slow energy conversion rate.

Finally, let us observe that although the dissipation rate is slow, $W_\eta \sim 10^{-7}$, the dimensionless current density, $J \simeq 10^7$, is still very high for $\eta \simeq 10^{14}$. Recall that the unit of current density is defined by

$$\frac{c}{4\pi}\frac{B_c}{l_c} \simeq 10^2 \text{ (cgs units)}.$$

It follows that the dimensional Sweet-Parker current density is $J_{sp} \simeq 10^9$ (cgs units). Note that a plausible upper limit for the current density is based on the proton sound speed c_s that is

$$J_s = nec_s \simeq 10^7 \text{ (cgs units)}$$

where $c_s = \sqrt{\gamma RT}$ (Priest & Forbes, 2000) and $\gamma = 0(1)$ is the specific heat ratio. Thus the dimensional current density is two orders of magnitude greater than the current density $J = nec_s$ based on the (proton) sound speed $c_s \simeq \sqrt{p/\rho}$. Such high current densities can lead to ion-acoustic turbulence in the plasma (Litvinenko & Craig, 2000). Hence, even though the Sweet-Parker model provides only slow merging, it predicts current densities which may be too high to be physically plausible.

3.2.4 Alternative reconnection theories

The Petschek mechanism

The Sweet-Parker model has been extended by several researchers over the years. Petschek (1964) developed a model in which both length L and width l of the diffusion region are smaller than the global length scale. This modification—shown on Figure 3.2—allows fast Ohmic dissipation rate and fast reconnection scalings. According to the Petschek reconnection mechanism slow mode shocks are set up along the separatrices i.e. the field lines that thread the neutral point as illustrated in Figure 3.2. The inflow region now consists of slightly curved field lines brought together in a narrow X-point. The effect of the shocks is to provide a normal field component which is associated with the distortion of the inflow magnetic field B_{in}.

We shall not consider the Petschek model further, other than to note that the approximately derived scalings (Priest & Forbes, 2000)

$$L \sim l \sim \eta, \tag{3.14}$$

are consistent with fast merging. That is, the Ohmic dissipation rate and reconnection rate scale as

$$W_\eta \sim \eta^0, \quad \eta J_0 \sim \eta^0 \tag{3.15}$$

as required for a “fast” mechanism.

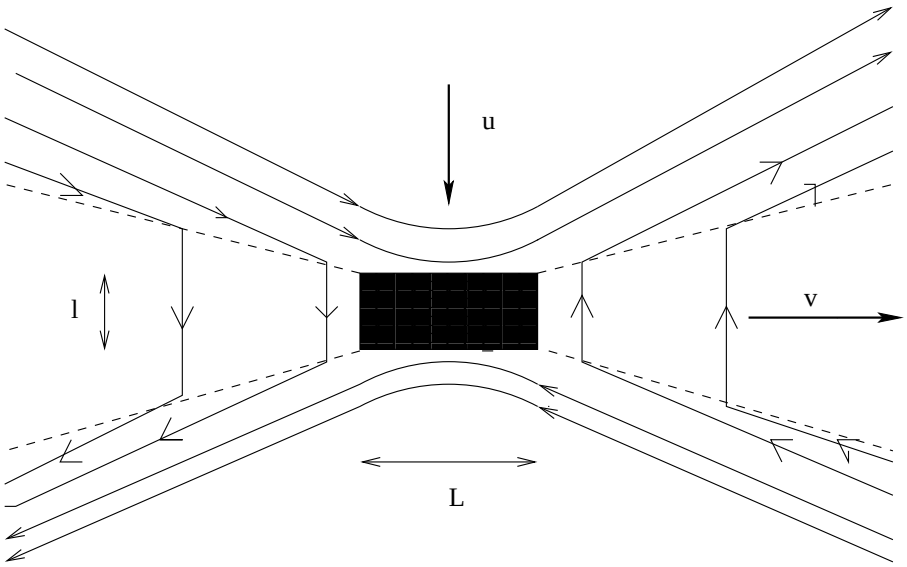

Figure 3.2: In the Petschek mechanism, the X-point angle is large, so that flux is readily evacuated from the neutral point. The dashed lines represent slow mode shocks which will also accumulate current.

Twenty years after Petschek's solution, a new generation of computational solutions was explored which questioned the validity of the Petschek model (see Biskamp, 2000). In particular, the development of a localized diffusion region based on uniform resistivity does not seem to be reproduced—the current tends to spread out uniformly along the magnetic separatrices (Biskamp, 2000). Hence Petschek-type models seem inappropriate for the diffusion region. A correct reconnection theory evidently requires a more detailed solution for the inner resistive region.

A related problem is the massive current density ($J \sim 10^{16}$ cgs units) required to flow through the very small rectangular area $O(l^2)$. These current densities are considered even more problematic than the Sweet-Parker values. They cannot be physically realistic since they exceed the light speed current density limit $J_c = nec$!

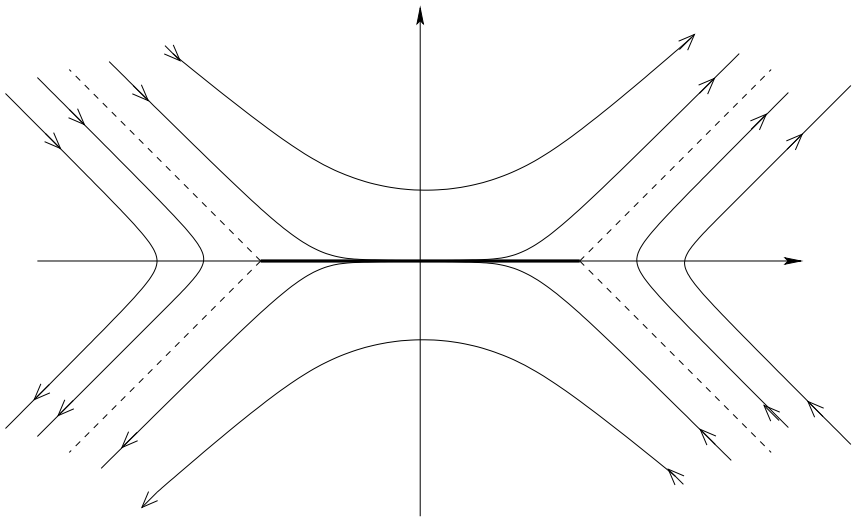

Figure 3.3: Field line structure of Syrovatskii solution. The bold line represents a branch cut current sheet and dashed lines are the separatrices.

The Syrovatskii solution

Syrovatskii & coworkers have also explained the formation of current sheets in a plasma (Syrovatskii, 1971). The Syrovatskii model is based on the ideal MHD equations. Syrovatskii points out that, at least for compressible plasmas, the MHD equations lead to current singularities which occur as either singular points or singular lines (see Figure 3.3). The theory does not describe real reconnection dynamics, but it suggests many important features of the reconnection solution. The main assumption is that currents in the system are highly localized in isolated sheets and outside these layers

$$\nabla^2 \psi = 0. \tag{3.16}$$

Here $\psi(x, y)$ is planar flux function so that $\mathbf{B} = \nabla\psi \times \hat{\mathbf{z}}$ (see equation 3.17). If ψ varies sufficiently slowly with time then $\psi(x, y, t)$ is determined by a steady-state singular boundary value problem. In the Syrovatskii solution ψ is described by a complex potential which contains a branch cut of finite length to model the current singularity (Biskamp, 2000).

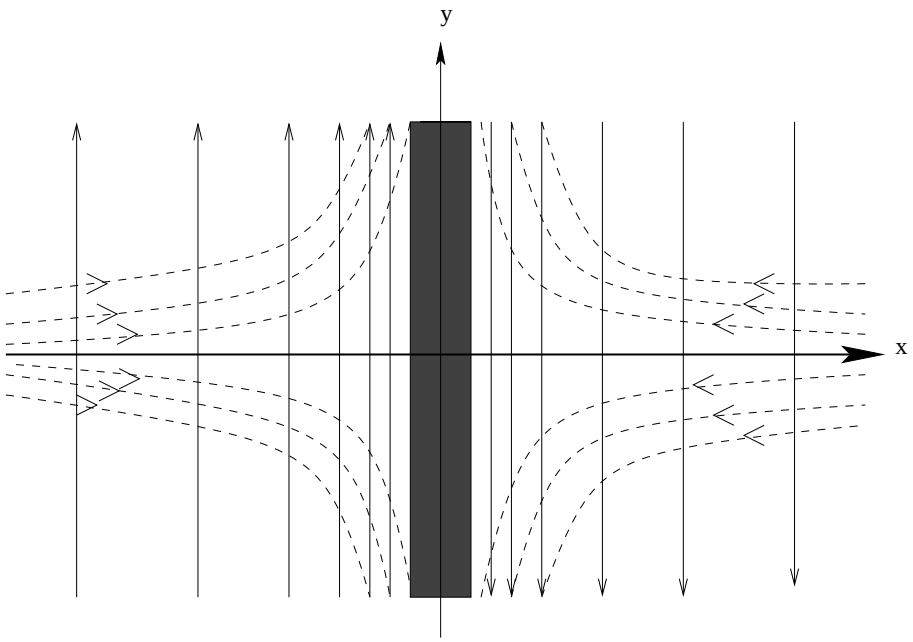

Figure 3.4: The steady-state Sonnerup & Priest solution for anti-parallel magnetic merging. The dashed lines represent the stagnation point flow and solid lines represent the anti-parallel magnetic field lines. The magnetic field lines annihilate along a neutral line aligned to the y-axis.

Sonnerup and Priest solution

The Sonnerup & Priest (1975) solution is closely related to the Sweet-Parker model, but assumes a stagnation point flow velocity field to drive together anti-parallel magnetic field lines ($\psi = \psi(x)$). Figure 3.4 shows these features, and illustrates how the magnetic flux piles up at the edge of the current sheet.

We shall not discuss this model in more detail since it is incorporated in the more general reconnection solution derived below in §3.2.5. However, it is worth noting that the resistive scalings for the model are

$$B_{sheet} \sim \eta^{-1/2}, \quad l \sim \eta^{1/2}.$$

These correspond to a super fast Ohmic dissipation rate, $W_\eta \sim \eta J^2 \Delta V$, since

$$W_\eta = \eta \left(\frac{B_{sheet}}{l} \right)^2 \eta^{1/2} \sim \eta^{-1/2}.$$

Note that the Sonnerup & Priest solution describes magnetic annihilation rather than reconnection, as the magnetic field is strictly one dimensional.

3.2.5 Exact solution of Craig and Henton

Unlike the previous models, the Craig & Henton (1995) approach is based on an exact analytic solution of the induction and momentum equations, (3.1) and (3.2) respectively. The Craig & Henton analysis naturally incorporates the Sonnerup & Priest (1975) magnetic annihilation model, and can be used to explore the impact of the Hall currents and and electron inertia on planar merging solutions of Chapter 6. In particular, we shall adopt the time-dependent forms of the Craig & Henton solution, taking into account both electron inertial and Hall effects within a generalized Ohm's law.

By writing the magnetic and velocity fields in planar two-dimensional geometry in terms of a magnetic flux function (ψ)

$$\mathbf{B} = \nabla\psi(x,y) \times \hat{\mathbf{z}} \tag{3.17}$$

and a stream function (ϕ)

$$\mathbf{v} = \nabla\phi(x,y) \times \hat{\mathbf{z}}, \tag{3.18}$$

we find that (3.1) and the curl of (3.2) reduce to

$$E + [\psi, \phi] = \eta \nabla^2 \psi, \tag{3.19}$$

$$\left[\nabla^2\phi, \phi\right] = \left[\nabla^2\psi, \psi\right]. \tag{3.20}$$

Here the Poisson bracket notation $[f,g] = f_x g_y - f_y g_x$ where $f_x = \partial f/\partial x$ has been introduced. We take the flux function ψ and velocity function ϕ to have the forms

$$\psi = g(x) + G(x,y), \quad \phi = f(x) + F(x,y), \tag{3.21}$$

where F and G are harmonic functions. The choice

$$F(x,y) = \alpha H(x,y), \quad G(x,y) = \beta H(x,y), \tag{3.22}$$

reduces the momentum brackets to

$$(\alpha f''' - \beta g''')H_y = 0 \tag{3.23}$$

which provided that $H_y \neq 0$, implies

$$f(x) = \frac{\beta}{\alpha} g(x) + q(x), \tag{3.24}$$

where $q(x)$ is an arbitrary quadratic function which for simplicity is set to zero. The induction equation (3.19) is consistent with the form for ψ only if H_y is a function of x. The only harmonic function satisfying this condition is $H \sim xy$. Taking $H = -xy$, the solutions for ψ and ϕ become

$$\psi(x,y) = -\beta xy + g(x), \qquad \phi(x,y) = -\alpha xy + \frac{\beta}{\alpha} g(x). \tag{3.25}$$

The velocity stream lines (ϕ) and magnetic field lines (ψ) can be seen in Figure 3.5. Note that the Craig & Henton solution with $\beta = 0$ is the Sonnerup & Priest annihilation solution, as described earlier.

Craig & Henton (1995) choose $q(x) = \frac{1}{2}\gamma x^2$ and obtained the homogeneous solution for $\gamma = 0$ by using the Dawson integral namely

$$\mathbf{B} = \beta x \hat{\mathbf{x}} - \left[\beta y + \frac{E}{\eta\mu} \mathrm{daw}(\mu x) \right] \hat{\mathbf{y}}, \tag{3.26}$$

$$\mathbf{v} = \alpha x \hat{\mathbf{x}} - \left[\alpha y + \frac{\beta}{\alpha} \frac{E}{\eta\mu} \mathrm{daw}(\mu x) \right] \hat{\mathbf{y}}, \tag{3.27}$$

where

$$\mathrm{daw}(x) = \int_0^x \exp(t^2 - x^2) dt.$$

We must take $0 \leq |\beta| < \alpha$ so that $\mu^2 > 0$ and the solution describes fluid washing flux into a current sheet aligned with the y-axis.

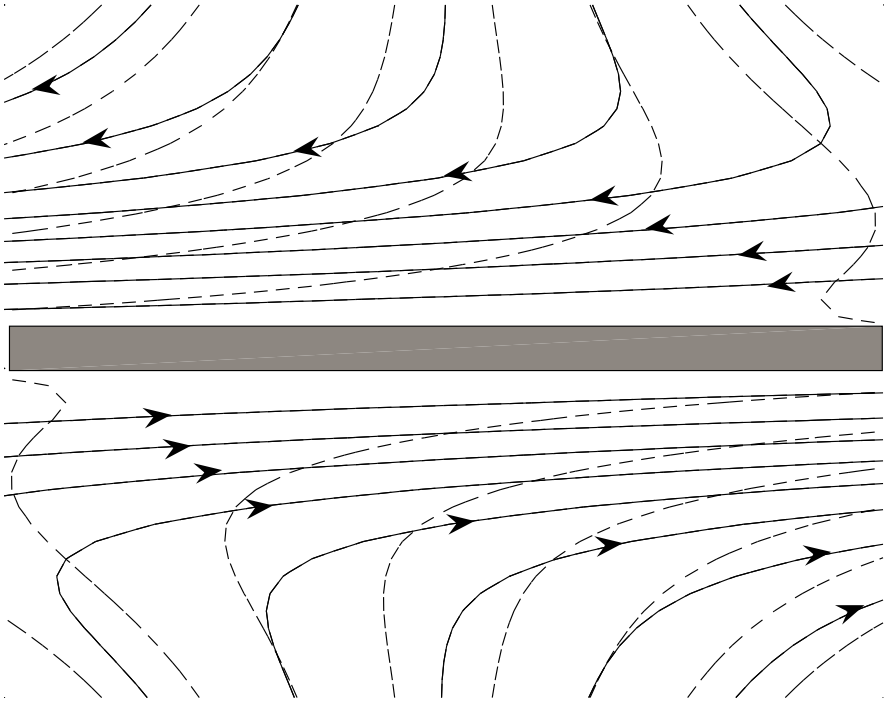

Figure 3.5: The steady-state Craig & Henton solution for anti-parallel magnetic merging. The dashed lines represent the stagnation point flow and solid lines represent the anti-parallel magnetic field lines. The solid lines represent the anti-parallel magnetic field lines. The magnetic field lines are reconnected along a neutral line aligned to the x-axis. Here we have used $\alpha = 1$, $\beta = 0.5$. The velocity stream lines move toward the diffusion region.

This solution can be more simply interpreted by noting that the induction equation (3.1) is reduced to

$$E - \alpha^* x g' = \eta g'' \,, \qquad \alpha^* = \frac{\alpha^2 - \beta^2}{\alpha^2} \tag{3.28}$$

where $g'(x) = dg/dx$. In the outer region where diffusion is negligible the field is given by $g' \simeq E/\alpha^* x$ whereas in the diffusion region $g' \simeq Ex/\eta$. Equating these expression defines the sheet-thickness

$$x_s^2 \simeq \frac{\eta}{\alpha^*} \tag{3.29}$$

and the disturbance field at the edge of the current layer

$$g'(x_s) \simeq \frac{E}{(\alpha^* \eta)^{1/2}} \,. \tag{3.30}$$

Note that the sheet is again very thin with $x_s \sim \eta^{1/2}$, and that the reconnection field piles up at the edge of the current layer. These expressions define what is known as a flux pile-up reconnection model. The reconnection rate and the Ohmic dissipation rate are both fast

$$\eta J_0 \sim \eta^0, \qquad W_\eta \sim \eta^0, \tag{3.31}$$

but a huge field has to build up at the edge of the current layer for sufficiently small resistivities η.

3.2.6 Limitation of steady-state merging solutions

We have considered a number of models describing steady-state magnetic reconnection. At first sight some of these models seem to give a complete description of fast magnetic merging. A recurring problem with all the solutions, however, is the very narrow current layer and the large current densities required to achieve a significant merging rate. In Chapter 6 we explore to what extent these difficulties can be overcome by using a more general form of Ohm's law that includes Hall current and plasma inertial contributions.

3.3 Time-dependent X-point collapse

To complete our discussion we now outline a completely different approach to the problem of constructing magnetic reconnection solutions. The approach is based on the transient collapse of a line-tied X-point field and the solution is constructed using the compressible MHD equations in bounded geometry. This model forms the basis of our reconnections studies in Chapters 4 and 5. Specifically in Chapter 4 we demonstrate that viscosity can have a profound effect on the dynamics of magnetic reconnection at magnetic X-points. In Chapter 5 we use the collapse model to investigate the influence of Hall currents on the X-point reconnection rate. Of interest to the present study is the recent analysis of McClements et al. (2004), who included electron inertial effects in the X-point collapse solution.

3.3.1 History of X-point collapse

The X-point collapse model, first considered by Dungey (1953), appears to provide the earliest analysis of magnetic reconnection. Dungey imposed a uniform, small current perturbation at a current-free Y-point and argued that the initial perturbation would grow with time and rapidly lead to the formation of a current sheet at the X-point. Cowling (1953) argued that the growth of the current density would violate Lenz's Law, but Dungey (1958) pointed out key the role of the $\mathbf{v} \times \mathbf{B}$ term in the evolution of the plasma to resolve the objection. Later on, Imshennik & Syrovatskii (1967) put Dungey's work on a firm mathematical foundation but, neither gas pressure nor electric resistivity was included in any of these early works. The effect of pressure in the MHD equations was assessed by Chapman & Kendall (1963, 1966) and Uberoi (1963, 1966). These studies suggested that in an incompressible plasma, the current density grows exponentially with time, and—at least for an unbounded geometry—the collapse could not be stopped by pressure.

None of these early solutions included the effects of the plasma resistivity. This

situation was remedied by the linear reconnection studies of Craig & McClymont (1991) and Hassam (1992). Below we give a detailed summary of the linearized X-point solutions.

3.3.2 The linearized X-point collapse model

The analysis is based on a bounded plasma-field geometry. The effects of gas pressure and viscosity are neglected and we assume constant resistivity in a uniform density background plasma. The equations to be used are the compressible MHD equations with Hall and electron inertial effects neglected. The analysis is performed in a plane cylindrical geometry and the field lines are anchored to a circular boundary at $r = 1$.

The X-point collapse model is based on current-free equilibrium field given by

$$\nabla^2 \psi_E = 0 \tag{3.32}$$

where ψ_E defines a background potential field. Solutions of (3.32) are given by the real and imaginary parts of z^n where $z = x + iy$. The $n = 2$ solution evidently provides the simplest model that can be used as a base state for exploring magnetic reconnection and so we take

$$\psi_E = -\frac{1}{2} r^2 \cos(2\theta). \tag{3.33}$$

We suppose that the equilibrium field ψ_E is constantly perturbed by low-amplitude disturbances, caused by photospheric motions. Figure 3.6 shows how ψ_E is perturbed by altering the separatrix angle, through the addition of the disturbance field

$$\Delta\psi = A(1 - r^2), \tag{3.34}$$

with amplitude $A = 0.2$. The effect of the disturbance field is to raise the energy of the X-point by changing the connections of the field lines. The equilibrium state can be regained only by reconnecting field lines through the neutral point.

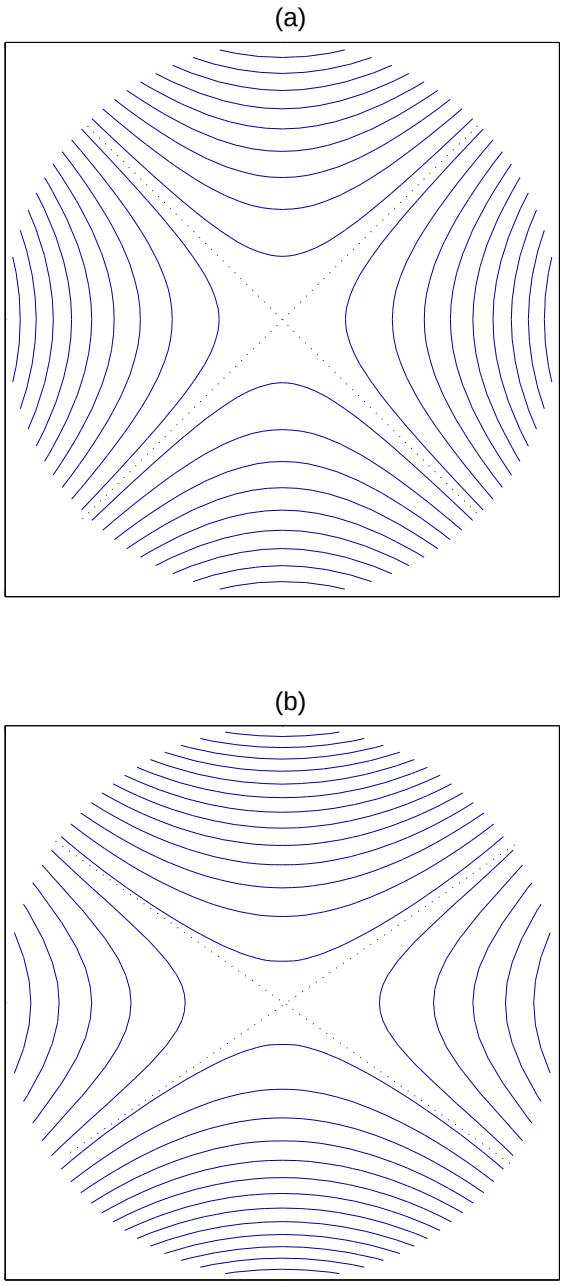

Figure 3.6: (**a**) The potential background field, $\psi_E = -0.5(r^2\cos(2\theta))$ in the circular domain. (**b**) The disturbance field $\Delta\psi = 0.2(1 - r^2)$ has the effect of altering the reconnections between the equilibrium field lines.

3.3.3 The linearized system

The equations describing the evolution of the X-point are the linearized momentum and induction equations:

$$\frac{\partial \mathbf{v}}{\partial t} = -\mathbf{J} \times \mathbf{B}_E = -\nabla^2 \psi \nabla \psi_E, \tag{3.35}$$

$$\frac{\partial \psi}{\partial t} + \mathbf{v} \cdot \nabla \psi = \eta \nabla^2 \psi, \tag{3.36}$$

where ψ describes the first order variation of the flux function. These combine to give

$$\psi_{tt} = \eta \nabla^2 \psi_t + r^2 \nabla^2 \psi, \tag{3.37}$$

where $\psi = \psi(r, \theta, t)$ and $\psi_t = \partial_t \psi$. The two terms on right hand side of equation (3.37) are the diffusion term and the advection term respectively.

Solutions of (3.37) can be found by taking (Craig & McClymont, 1991; Hassam, 1992)

$$\psi(r, \theta, t) = e^{im\theta} \psi_m(r, t) \tag{3.38}$$

where $\psi_m(r, t)$ is the azimuthal component and m is integer. In the case $m = 0$, the solution ψ is function of r and t only. The azimuthal components ψ_m satisfy (3.37) with ψ replaced by ψ_m. The equation for magnitude of the current density reduces to

$$\nabla^2 \psi_m = \frac{\partial^2 \psi_m}{\partial r^2} + \frac{1}{r} \frac{\partial \psi_m}{\partial r} - \frac{m^2}{r^2} \psi_m. \tag{3.39}$$

The boundary conditions at $r = 0$ follow from the boundedness of the current density: for $m = 0$, a finite displacement is allowed at the origin where

$$\frac{\partial}{\partial r} \psi_0(0, t) = 0, \tag{3.40}$$

but in all other cases

$$\psi_m(0, t) = 0 \quad \text{for} \quad m > 0. \tag{3.41}$$

It follows that finite currents at the origin are possible only for $m = 0$ modes—and that higher azimuthal modes are intrinsically non-reconnective. On the outer

boundary, the field is line-tied and so the normal component of the field, $\partial\psi/\partial\theta$ must vanish. Therefore we can always take $\psi(1,t) = \text{const.} = 0$, consistent with line-tying.

Oscillation frequency and decay rate

Solutions for $\psi_m(r,t)$ can be constructed in a variety of ways. By taking

$$\psi_m(r,t) = e^{\lambda t} f(r), \quad \lambda = \alpha + i\omega, \tag{3.42}$$

we obtain a complex eigenvalue equation which can be solved analytically, either by matched asymptotic expansions or by taking the small η limit of the formal hypergeometric function solution (Craig, 1994). Here ω is the oscillation frequency and α is the decay rate of the decaying eigenmode. In the case $m = 0$, ω and α are given by Craig & Watson (1992).

$$\omega = \frac{\pi}{|\ln\eta|}, \quad \alpha = -\frac{1}{2}\omega^2, \tag{3.43}$$

with approximate oscillation period

$$T \simeq \frac{2\pi}{\omega} \simeq -2\ln\eta. \tag{3.44}$$

Craig & McClymont (1993) show that higher order modes ($m > 0$) correspond to fast dissipation at the rate

$$\alpha = -\frac{1}{|\ln\eta|^3}.$$

Higher azimuthal modes ($m > 0$) are not associated with reconnection, but it is possible for higher modes to decay by non-resistive mechanisms such as viscous damping as discussed in Chapter 4.

Current properties and Ohmic dissipation rate

The X-type neutral point evolution will drive current density

$$\mathbf{J} = -\nabla^2\psi\,\hat{\mathbf{z}}, \tag{3.45}$$

only in the $\hat{\mathbf{z}}$ direction. The current localization is limited only by resistive diffusion at the neutral point and from this we may deduce the scalings (Craig & Watson, 1992)

$$J_0 \sim \frac{1}{\eta}, \quad r_s^2 \sim \eta \tag{3.46}$$

where r_s^2 is the area enclosing the cylindrical wave. The scaling laws of Ohmic dissipation and reconnection rates are given by

$$W_\eta = \eta J_0^2 r_s^2 \simeq \eta^0, \quad \eta J_0 \simeq \eta^0, \tag{3.47}$$

and both rates are formally fast. However gas pressure has been neglected, as have axial components in the structure of the equilibrium field. Both these effects are known to reduce the merging rate (McClymont & Craig, 1996).

Self-similar mode

One curiosity is that a self-similar mode is obtained by neglecting ψ_{tt} in (3.37). In this case the current density takes the form $J(r,t) \simeq J(r,0)\exp(-r^2 t/\eta)$. This mode is not representable by a superposition of eigensolutions (Hassam, 1992). However, since the self-similarity becomes apparent only after the discrete modes have damped out and the current is localized in the diffusion region, it is energetically insignificant (Hassam, 1992; Craig & McClymont, 1993). Therefore the proof, based on the discrete eigenmode analysis, that all global azimuthal modes damp resistively on a fast Alfvénic timescale, remains uncompromised. We return to a discussion of the self-similar mode in Chapter 4.

To summarize, the linearized X-point model, provides both fast Ohmic decay and a fast reconnection rate, as equation (3.47) confirms. However, in addition to non-linear effects, the analysis neglects gas pressure as well as the possible influence of non-planar components of the background X-point field. Finite amplitude studies (McClymont & Craig, 1996) suggest that finite gas pressure can inhibit the

merging rate at least for the strongly localized current regions associated with small resistivities typical of the solar plasma.

3.4 Summary

In this chapter we have considered a number of magnetic merging solutions based on two distinct approaches. The first approach, which describes steady-state incompressible merging in "open geometry", has been developed by several authors (Sweet, 1958; Parker, 1957,1963; Petschek, 1964; Syrovatskii, 1971; Craig & Henton, 1995). Although the Sweet-Parker model provides a simple approximate description of quasi-steady merging, we have noted that exact solutions are now available that describe steady-state reconnection in planar geometry. In particular it is the solution of Craig & Henton (1995) that we shall develop in explaining the role of Hall current and electron inertia in Chapter 6.

A second approach to the reconnection problem is provided by X-point collapse models. These have been systematically developed since the early treatment of Dungey (1953). In contrast to the quasi-steady treatment, typified by Sweet-Parker current sheets, these models can describe transient, compressible reconnection in closed magnetic geometries. The advantage of this approach is that a bounded, planar region is considered in which the magnetic field topology is well defined. As yet no exact description of X-point collapse has been developed, and the most complete description is probably provided by the linearized, X-point solutions of Craig & McClymont (1991, 1993) and Hassam (1992) which although neglecting the effects of gas pressure, provides fast reconnection for arbitrary resistivities. It is these models we invoke when studying the influence of viscosity and Hall currents in Chapters 4 and 5 respectively.

Chapter 4

Viscous effects in planar magnetic X-point reconnection

4.1 Introduction

In the previous chapter (§3.3), we presented analytical reconnection solutions for the case of small disturbances of line-tied $2D$ magnetic X-points with negligible plasma pressure. Specifically, we noted that an eigenfunction description can be used to show that the reconnection rate is "fast," in the sense that the dissipation rate is dependent only logarithmically on the plasma resistivity η (Craig & McClymont, 1991; Craig & Watson, 1992; Hassam, 1992; Craig & McClymont, 1993; Craig, 1994). Note that a typical value of η in the solar corona is of order 10^{-12} or smaller, and the weak dependence of the dissipation rate on resistivity is essential in providing significant energy release rates in flares.

We note that X-point reconnection models have been developed using a simplified "collisional resistive" form of Ohm's law. They have however, been extended to include gas pressure, axial field components and plasma inertial effects (Ofman et al., 1993; Craig & McClymont, 1997; McClements et al., 2004). What has not been

considered is the influence of Hall currents and plasma viscosity.

It is perhaps puzzling at first sight that viscous plasma effects are often neglected in reconnection studies. One justification is that "topological energy"—that is, energy bound up in the magnetic field topology—can be released only by reconnection. However, viscous dissipation is expected to be significant compared to resistive effects in the solar corona since the plasma viscosity may be many orders of magnitude larger than the resistivity (see §2.2.4). Therefore, viscous effects can be expected to play an important role. Recent observational studies of solar flares (McKenzie & Hudson, 1999; McKenzie, 2000; Asai et al., 2004) also give some evidences of the effects of viscosity in the solar plasma.

Park, Monticello & White, (1984) modified the Sweet-Parker and Petschek scalings of the magnetic reconnection rate to include the effect of plasma viscosity. The modified scaling shows that viscous effects can be important in high-β plasmas, because viscosity is known to lead to slower inflows and outflows in steady-state magnetic reconnection models. Fabling & Craig (1996) discussed the possibility that viscosity could undermine the fast reconnection of incompressible exact solutions introduced by Craig & Henton (1995). What seems to have escaped attention is a detailed analysis of viscous dissipation in the context of X-point collapse models.

The goal of this chapter is to study the influence of viscosity on the dynamics of X-point collapse. We use two different perturbation fields; a "non-reconnection" disturbance field and a "reconnection" disturbance field, which play different roles depending on the resistivity η and viscosity ν. Specifically, in the absence of resistive reconnection, viscous dissipation can remove only kinetic energy from the fluid but cannot release topological energy bound up in the structure of the magnetic field. Even so, we point out that viscosity can generally be expected to dissipate a significant fraction of the total energy in a dynamically evolving plasma. We also demonstrate that the visco-resistive coupling can produce significant new energy

dissipation mechanisms. These points were first emphasized by Craig, Litvinenko & Senanayake (2005). All the results presented in that paper were computed by the present author: these results are extended and discussed comprehensively in this chapter.

The chapter is organized as follows. In §4.2 we introduce the equations describing the visco-resistive X-point plasma, taking care to distinguish between reconnective and non-reconnective perturbations. Specifically the linearized momentum and induction equations are examined in order to investigate the global energy evolution in the presence of viscous and resistive effects. In §4.3, resistive X-point solutions are explored in several ways: oscillatory and monotonic decay of the magnetic and kinetic energy, oscillation frequency and damping rate, current sheet properties and Ohmic dissipation rate. We compare some of our results with previous work of X-point collapse discussed in §3.3. The viscous X-point disturbance problem will be discussed in §4.4 using the two different perturbation modes. The effects of visco-resistive coupling are examined in §4.5. Quantitative scaling laws describing visco-resistive dissipation are explained in §4.6. Finally in §4.7, we summarize our results.

4.2 The linearized X-point reconnection equations

We begin by considering the theory of §2.2.4 which summarizes the influence of viscous and resistive effects on the momentum and induction equations. The non-dimensional continuity (2.25), momentum (2.26) and induction (2.27) equations reduce to

$$\frac{\partial \rho}{\partial t} + \nabla \cdot (\rho \mathbf{v}) = 0, \tag{4.1}$$

$$\frac{\partial \mathbf{v}}{\partial t} + (\mathbf{v} \cdot \nabla)\mathbf{v} = \mathbf{J} \times \mathbf{B} + \nu \left[\nabla^2 \mathbf{v} + \frac{1}{3} \nabla (\nabla \cdot \mathbf{v}) \right], \tag{4.2}$$

$$\frac{\partial \mathbf{B}}{\partial t} = \nabla \times (\mathbf{v} \times \mathbf{B}) - \eta \nabla \times \mathbf{J}, \tag{4.3}$$

where plasma pressure, Hall currents and electron inertial effects are neglected.

We follow the linearized X-point collapse problem as formulated by Craig & McClymont (1991) and Hassam (1992), but, generalized to include the effects of fluid viscosity. That is, we assume two-dimensional plasma of negligible pressure contained within a rigid boundary (with $\partial_z = 0$). Writing the magnetic field as $\mathbf{B} = \nabla(\psi_E + \psi) \times \hat{\mathbf{z}}$, and linearizing equations (4.1), (4.2) and (4.3) we get

$$\partial_t \rho = -\rho_0 \nabla \cdot \mathbf{v} \quad (\rho_0 = 1), \tag{4.4}$$

$$\partial_t \mathbf{v} = -\nabla^2 \psi \nabla \psi_E + \nu \left[\nabla^2 \mathbf{v} + \frac{1}{3} \nabla \left(\nabla \cdot \mathbf{v} \right) \right], \tag{4.5}$$

$$\partial_t \psi = -\mathbf{v} \cdot \nabla \psi_E + \eta \nabla^2 \psi. \tag{4.6}$$

Here $\mathbf{v}$ denotes the velocity and ψ denotes the perturbation of the flux function with respect to the equilibrium ψ_E. When the resistivity, η, and viscosity, ν, are zero, equations (4.5) and (4.6) imply that total energy of the disturbance is preserved, and that there is a continual interchange of magnetic and kinetic energies in the plasma (see 4.2.2 below).

4.2.1 Boundary conditions

The governing equations (4.5) and (4.6) become very complex when viscosity is added to the linear relaxation problem, because viscous effects can alter the X-point problem through their influence on the global velocity field of the plasma. Since fluid acceleration is no longer constrained to be perpendicular to the equilibrium field lines, it is not possible to describe the system analytically as can be done in the case of an inviscid plasma.

In particular, we dispense with the cylindrical mode decomposition (see §3.3) and assume that the reconnection region is defined over the square region $-1 \leq x, y \leq 1$. The imposition of a highly conducting rigid boundary implies that there is no flux out of the source volume, and that we can take ψ and $\mathbf{v}$ to vanish on the bounding

surface. That is

$$\mathbf{v} = \frac{\partial \psi}{\partial t} = 0 \quad \text{on } S \tag{4.7}$$

where S is the boundary surface. These conditions make it straightforward to compute the global energy losses of the fluid. Introducing the global magnetic and kinetic energies

$$M = \int \frac{1}{2} B^2 dV, \quad K = \int \frac{1}{2} v^2 dV \tag{4.8}$$

we now establish a relation describing the global energy losses of the fluid in the presence of viscous and resistive dissipation, namely

$$\frac{\partial}{\partial t} \int (M + K) dV = - \int \left(\eta (\nabla^2 \psi)^2 + \nu (\mathbf{\Omega} \cdot \mathbf{\Omega} + \frac{4}{3} (\nabla \cdot \mathbf{v})^2 \right) dV. \tag{4.9}$$

Here we assume (4.7) and introduce

$$\mathbf{\Omega} = \nabla \times \mathbf{v} \tag{4.10}$$

as the vorticity of the plasma.

4.2.2 An expression for global energy dissipation

To prove (4.9) we take the dot product of (4.2) with $\mathbf{v}$

$$\mathbf{v} \cdot \mathbf{v}_t = -\mathbf{v} \cdot \nabla^2 \psi \nabla \psi + \nu \mathbf{v} \cdot \left\{ \nabla^2 \mathbf{v} + \frac{1}{3} \nabla (\nabla \cdot \mathbf{\Omega}) \right\}. \tag{4.11}$$

Combining equations (4.3) and (4.11), and integrating over the volume then gives

$$\frac{\partial}{\partial t} \int (K + M) dV = - \int \eta (\nabla^2 \psi)^2 dV + \int \nu \mathbf{v} \cdot \left(\nabla^2 \mathbf{v} + \frac{1}{3} \nabla (\nabla \cdot \mathbf{v}) \right) dV. \tag{4.12}$$

Using the vector relation $\nabla^2 \mathbf{v} = \nabla (\nabla \cdot \mathbf{v}) - \nabla \times (\nabla \times \mathbf{v})$ we have

$$\frac{\partial}{\partial t} \int \frac{1}{2} \left(\mathbf{v} \cdot \mathbf{v} + \mathbf{B} \cdot \mathbf{B} \right) dV = - \int \eta (\nabla^2 \psi)^2 dV + \int \nu \mathbf{v} \cdot \left(\frac{4}{3} \nabla (\nabla \cdot \mathbf{v}) - \nabla \times \mathbf{\Omega} \right) dV, \tag{4.13}$$

with $\mathbf{\Omega} = \nabla \times \mathbf{v}$. Considering vector analysis identities we note that

$$\int \nabla \cdot (\mathbf{v} \times \mathbf{\Omega}) dV = \int (\mathbf{\Omega} \cdot \mathbf{\Omega}) dV - \int \mathbf{v} \cdot (\nabla \times \mathbf{\Omega}) dV, \tag{4.14}$$

and

$$\int \nabla \cdot ((\nabla \cdot \mathbf{v})\mathbf{v})\, dV = \int (\nabla \cdot \mathbf{v})^2 dV + \int \mathbf{v} \cdot \nabla(\nabla \cdot \mathbf{v}) dV. \tag{4.15}$$

According to our boundary conditions ($\mathbf{v} = \mathbf{0}$ on S), the divergence theorem implies that the left hand side of equations (4.14) and (4.15) vanish. Hence the rate of the change of global energy is given by (4.9). The two terms of the right hand side of (4.9),

$$W_\eta = \int \eta(\nabla^2 \psi)^2 dV, \quad W_\nu = \nu \int (\mathbf{\Omega} \cdot \mathbf{\Omega} + \frac{4}{3}(\nabla \cdot \mathbf{v})^2) dV \tag{4.16}$$

indicate the Ohmic dissipation rate, and the viscous dissipation rate respectively. This expression makes explicit the resistive and viscous contributions to the decay of the total energy, but does not isolate the separate magnetic and kinetic energy components.

4.2.3 The X-point reconnection simulation

Recall that chapter 3 introduced a flux function ψ_E for the background potential field using the cylindrical coordinates:

$$\psi_E = -\frac{1}{2} r^2 \cos(2\theta). \tag{4.17}$$

The initial X-point ψ_E is perturbed by superposing onto it a small magnetic perturbation $\Delta\psi(r, \theta, t)$. We now explore dynamic reconnection by studying the behavior of perturbations of the flux function using a rectangular coordinate system, in which

$$\psi_E = -\frac{1}{2}(x^2 - y^2), \tag{4.18}$$

for $-1 \leq x,\, y \leq 1$. In the present study, two types of perturbed X-point configurations ($\Delta\psi = \Delta\psi(x, y, t)$) are considered:

1. a non-reconnection perturbation field which always maintains the original X-point topology. This defines the non-topological mode,

2. a reconnection perturbation field which changes the connections between the equilibrium field lines. This defines the topological mode.

The initial background field ψ_E represented in Figure 4.1a is perturbed by each of the above fields. Figure 4.1b shows the total field $\psi_E + \Delta\psi$ when a non-reconnection disturbance field

$$\Delta\psi(x, y, 0) = (1 - x^2)(1 - y^2)e^{-s^2}, \qquad s = \frac{1}{2}\ln(x^2 + y^2) \tag{4.19}$$

is applied. Note that $\Delta\psi$ raises the magnetic energy of the X-point but maintains the topology inherent in the equilibrium field. Each of four lobes of the field contains the same amount of magnetic flux and they are separated by dashed lines (the separatrices). This non-topological disturbance field $\Delta\psi$ initially vanishes both at the boundary and at the neutral point. This mode is not associated with reconnection and so it is possible for the non-reconnection mode to decay by non-resistive mechanisms such as damped fluid motions, as discussed in this chapter.

Figure 4.1c represents the total field when a reconnection disturbance field

$$\Delta\psi(x, y, 0) = (1 - x^2)(1 - y^2) \tag{4.20}$$

is added. The field perturbation at the boundary vanishes for all time and alters the topology at the X-point. The original flux function ψ_E has been perturbed in a way that changes the topology by altering the angle between the separatrices. The excess flux in the left and right lobes has to be reconnected through the X-point so that the equilibrium configuration can be regained. This implies that the initial displacement in ψ at the origin has to decay resistively as the system evolves.

4.2.4 Computational diagnostics

We demonstrate resistive and viscous effects on the X-point collapse using diagnostics for

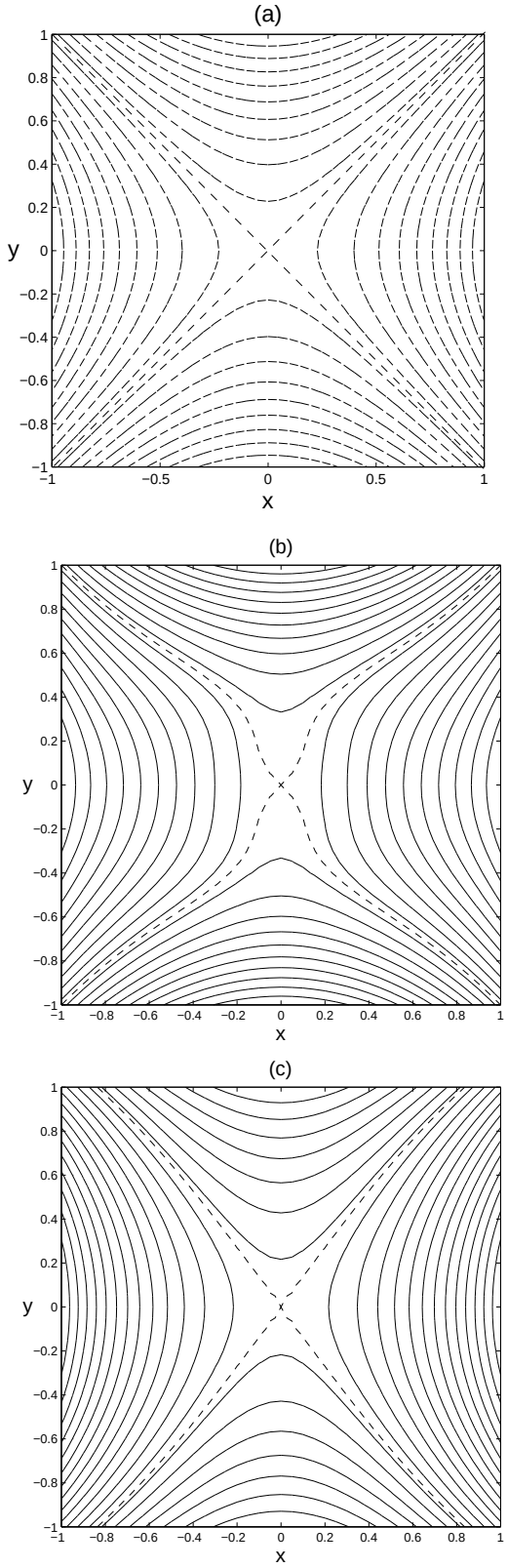

Figure 4.1: (**a**) Field lines of background field $\psi_E = -0.5(x^2 - y^2)$. In (**b**) ψ_E has been perturbed by disturbance field (4.19) which maintains the original X-point topology. In (**c**) however, the disturbance field (4.20) has the effect of altering the connections between the equilibrium field lines.

- the global energy decay based on the magnetic energy M and kinetic energy K;
- the oscillation frequency ω and damping rate α of the disturbance;
- the scaling properties of the current sheet, namely the magnitude of the current density J and the area of the sheet A_s;
- the non-oscillatory decay as $t \to \infty$.

As our prime diagnostic is the global energy, we discuss magnetic and kinetic energy dissipation and the relative contributions of viscous and Ohmic dissipation. We demonstrate in particular, that the system generally depends on the nature of the perturbation field; whether or not the mode is topological or non-topological; and the magnitude of the plasma viscosity and resistivity.

4.2.5 Numerical methods

We simulate the momentum and induction equations over the square region $-1 \leq x, y \leq 1$ to determine the evolution of the disturbance fields $\psi(x, y, t)$ and $\mathbf{v}(x, y, t)$. We shall always take $\mathbf{v} = 0$ initially so the excess initial energy resides in the magnetic field. We use Newton forward and backward difference formula to achieve numerical accuracy close to the outer boundary. We chose a grid spacing ($\Delta x = \Delta y = \Delta$) so that at least 8 mesh points lie across the current layer. The computations discussed below require step sizes $\Delta < \eta^{1/2}/4$ in resistive case, $\Delta < \nu^{1/2}/4$ in viscous case and $\Delta < (\eta\nu^{1/4})/4$ in visco-resistive case to achieve satisfactory resolution. To achieve stability of the finite-difference form of equations (4.4, 4.5 & 4.6), we restrict the time step by taking the minimum of ($\Delta t_a,\ \Delta t_d$) where Δt_a is the advective limit based on CFL (Courant, Friedrichs and Lewy) condition and Δt_d is the relevant diffusive limit (Richtmyer & Morton, 1967), as discussed above.

4.3 Inviscid Resistive X-point solutions

As noted in the previous chapter, the resistive X-point collapse produces the resistive current sheet scalings

$$x_s \sim \eta^{1/2},\ J \sim 1/\eta,\ A_s \sim \eta \text{ and } W_\eta \sim \eta^0,$$

where A_s is area of the current sheet. In the case of oscillatory decay, the equipartition of kinetic and magnetic energies implies the oscillation frequency and decay rate

$$\omega = \frac{\pi}{|\ln \eta|}, \text{ and } \alpha = -\frac{1}{2}\omega^2.$$

Finally, after the oscillations have died down, a self-similar mode emerges associated with a very slow monotonic decay as $t \to \infty$.

Since we are now working with modified boundary conditions, we first investigate whether the above analytic predictions hold good. For example, does the "bounce period"

$$T_A = \frac{2\pi}{\omega}, \tag{4.21}$$

still scale as $2|\ln \eta|$ as the analytic theory (with $r_s \sim \eta^{1/2}$) would predict? The only difference is the replacement of the circular outer boundary by a rigid, square conductor. Note that the predictions of the resistive theory do not depend on the nature of the initial condition, namely whether a reconnection or non-reconnection disturbance is taken as an initial condition.

In the case $\nu = 0$, (4.5) and (4.6) reduce to a single equation for ψ, namely

$$\psi_{tt} = \eta \nabla^2 \psi_t + |\nabla \psi_E|^2 \nabla^2 \psi, \tag{4.22}$$

where $|\nabla \psi_E|^2 = x^2 + y^2 = r^2$ for the background field $\psi_E = -(x^2 - y^2)/2$. Much of the essential physical behaviour can be deduced from (4.22). The two terms on right hand side of equation (4.22) are the diffusion term and the advection term

respectively. Note that for $r << \eta^{1/2}$, in the diffusion region, (4.22) becomes

$$\psi_t = \eta \nabla^2 \psi, \tag{4.23}$$

and for $r >> \eta^{1/2}$ in the advection region, we deduce the wave equation

$$\psi_{tt} = r^2 \nabla^2 \psi, \tag{4.24}$$

with wave speed r (in units of v_A). The wave equation is second-order in time and therefore requires two initial conditions $\psi(x,0)$, $\psi_t(x,0)$.

The time taken for a localized wave launched from the outer boundary to impact the diffusion region is given by

$$\tau = \int_{r_s}^{1} \frac{1}{r} dr \tag{4.25}$$

where $r_s \sim \eta^{1/2}$ is the current sheet thickness. In the limit of small but finite η, this time reduces to $\ln r_s = \frac{1}{2} \ln \eta$, which is one quarter of the fundamental oscillation period for the disturbance (see (3.44)).

The global energy decays with the resistive damping rate α, but there is a continual exchange of magnetic and kinetic energies—equipartition—on the oscillation period of the fluid.

4.3.1 Oscillatory behaviour of magnetic and kinetic energies

We discuss here the decay of the disturbance field energy for the two initial conditions of Figures 4.1b and c. Initially, in the case of non-reconnection mode, the value of the flux function at the X-point is zero, but this is increased by the resistivity. This behaviour is summarized in Figure 4.2a. In the case of the reconnection mode, the perturbation field at the X-point is initially non-zero, and resistivity alone may alter the magnetic field via fast reconnection (Figure 4.2b). The field lines oscillate and reconnect as they pass through the origin, and resistivity is essential to this mode.

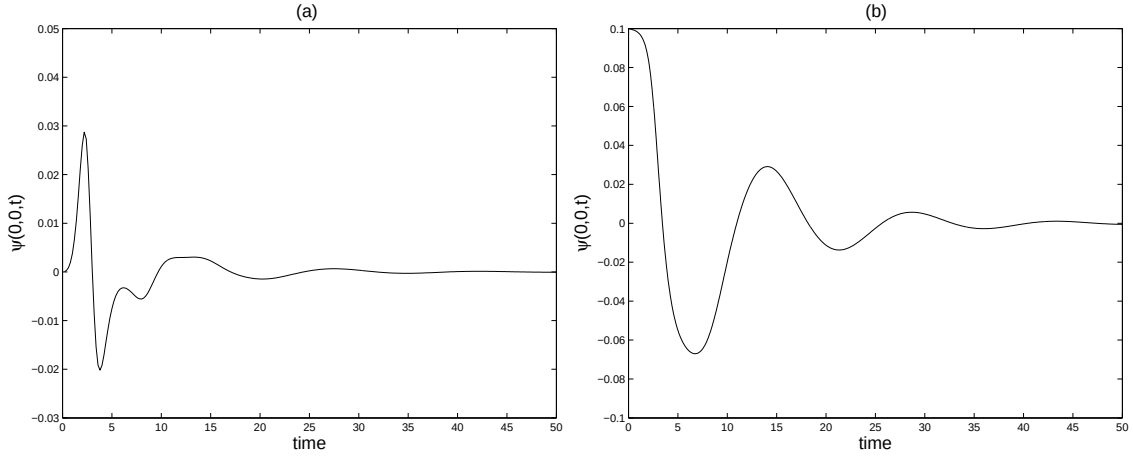

Figure 4.2: Oscillation of the magnetic flux function at the X-point for initial conditions of (**a**) Figure 4.1b and (**b**) Figure 4.1c. The plots show the evolution of ψ at the neutral point $(0, 0)$ for the case $\eta = 3 \times 10^{-3}$.

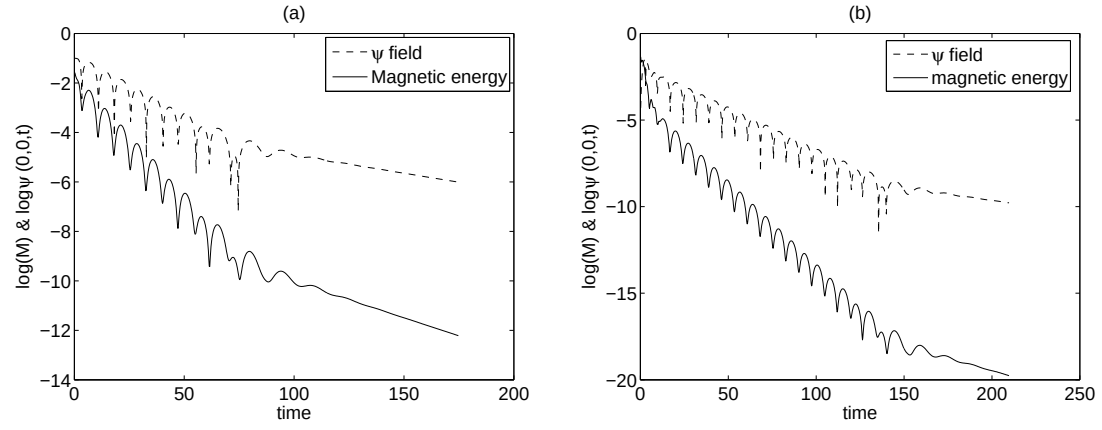

Figure 4.3: Time evolution of ψ at the neutral point (dashed line) and global magnetic energy over the region $-1 \leq x, y \leq 1$ (solid line). Figure (**a**) shows the topological disturbance field and (**b**) the non-topological disturbance field with $\eta = 0.003$, $\nu = 0$.

As summarized in Figures 4.3a and b both the topological and non-topological resistive solutions comprise three distinct evolutionary phases: there is an initial period of rapid decay, followed by a long period of oscillatory decay, and a slowly decaying asymptotic component. We know that an initial implosive stage releases the bulk of the energy associated with reconnective field disturbances. Also these figures illustrates that damping of total magnetic energy in the square domain and the oscillation of the ψ field at the origin are phase identical. The first stage, removes most of the energy from a global disturbance. Then the remaining energy is damped in the oscillatory phase. The displacement of $\psi(0,0,t)$ mimics the oscillatory decay of the global magnetic energy M (see (4.8)). The decay rate of $\psi(0,0,t)$ is exactly one half of the decay rate for global magnetic energy (i.e. $\ln B^2 = 2\ln B$). This behaviour implies that transient oscillatory reconnection occurs in all cases, even though the net magnetic flux reconnected must be zero in the case of non-topological disturbances.

A fraction of the initial magnetic energy is converted to kinetic energy until equipartition is achieved. Figures 4.4a and b show equipartition of the magnetic energy and kinetic energy with $\eta = 0.003$, $\nu = 0$. The initial rapid decline ($t < 10$) is followed by a fast oscillatory decay until $t \simeq 150$. Magnetic and kinetic energies are continuously interchanged in this stage of fast oscillatory decay. In the non-topological mode, more than 95% of the initial energy is lost very quickly during the initial phase, by resistive dissipation. However, excess kinetic energy remains after the long oscillatory decline.

4.3.2 Oscillation frequency and damping rate

Figure 4.5a indicates that the oscillation period depends only logarithmically on η. Analyzing the variation of the oscillation period with η allows us to make a

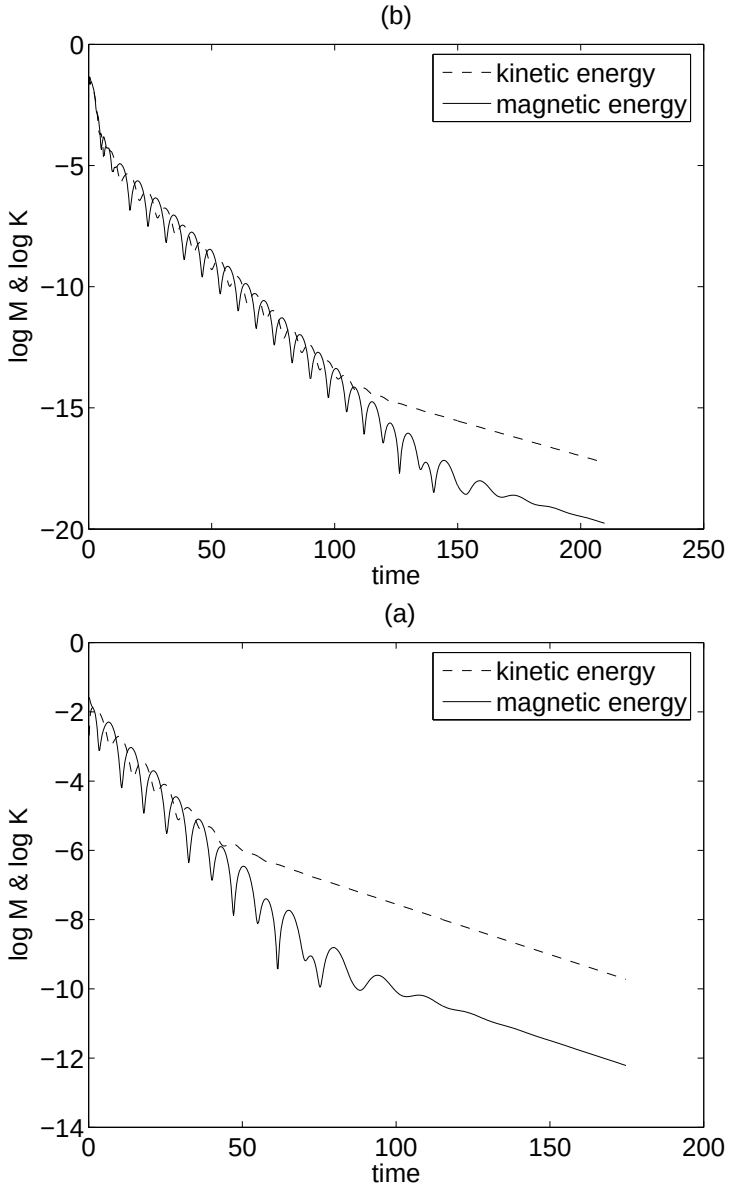

Figure 4.4: The decay of the magnetic and kinetic energies for the initial conditions of (**a**) Figure 4.1b—non-reconnection mode and (**b**) Figure 4.1c—reconnection mode. The results show the equipartition between the magnetic and kinetic fluid energies for $\nu = 0$, $\eta = 0.003$.

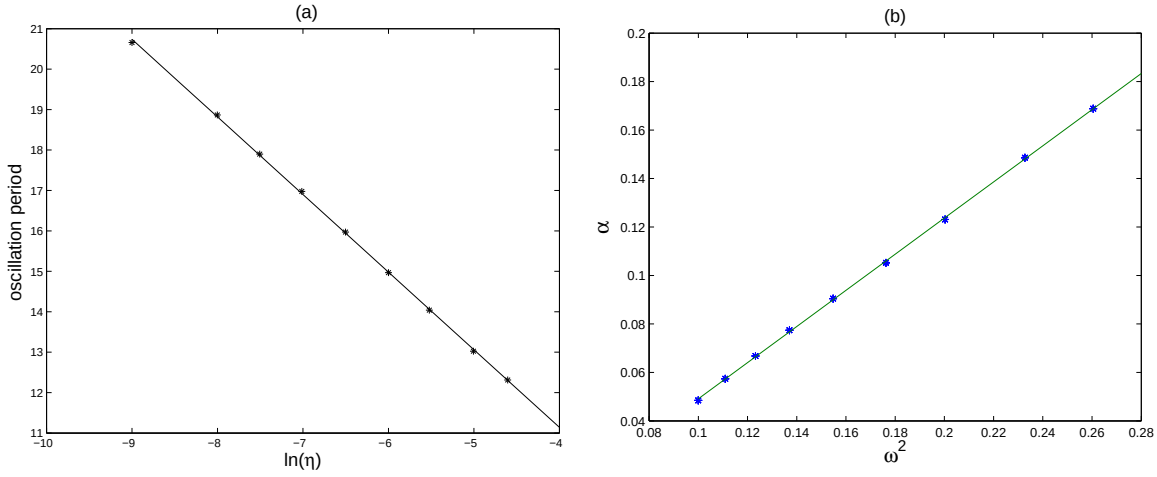

Figure 4.5: (**a**) The oscillation period versus $\ln\eta$ shows the computed oscillation period is $T = -2\ln\eta$. (**b**) Indicates the decay rate α of the ψ field against ω^2. The plot shows α and ω scale as $\alpha = \omega^2/2$.

numerical estimate of the oscillation period T as

$$T_A \simeq 2|\ln\eta| \tag{4.26}$$

which compares well with the analytic estimate of the oscillation period (T_A) of cylindrical mode (Craig & McClymont, 1991). Figure 4.5b shows our computed relation between α and ω for a rectangular boundary, which are similar to the previous analytical results of $\alpha \simeq \omega^2/2$. Hence, our numerical results for α and ω at the neutral point are broadly consistent with the eigenvalue description of the cylindrical mode.

4.3.3 Current sheet properties and Ohmic dissipation rate

We now check whether the analytic scaling predictors of the current properties

$$J_0 \sim \frac{1}{\eta}, \quad A_s \sim \eta$$

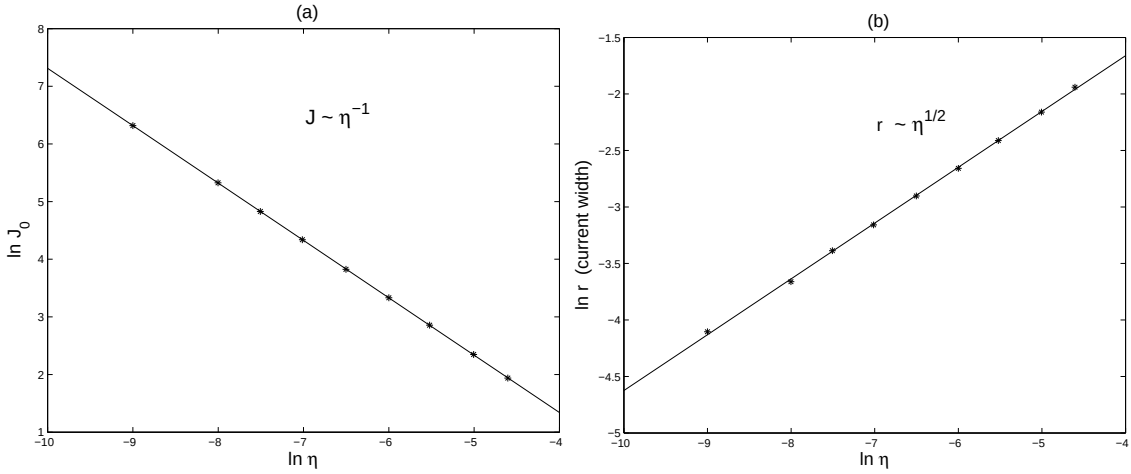

Figure 4.6: (**a**) The maximum current density at the X-point versus resistivity. The slope of the line is -0.988 ($\simeq -1.0$) and hence $J_0 \simeq \eta^{-1}$. (**b**) Current width versus resistivity. The slope of the line is 0.49 ($\simeq 0.5$), hence the current width scales as $r_s \simeq \eta^{1/2}$.

are compatible with observed results in the X-type neutral point evolution. The plot $\ln J_0$ versus $\ln \eta$ and the plot $\ln r_s$ versus $\ln \eta$ are shown in Figures 4.6a and b respectively. These figures show that the current density scales as the inverse of the resistivity ($J_0 \sim \eta^{-1}$) and the current width scales as $r_s \sim \eta^{1/2}$. The measured current width r_s is as shown in Figure 4.7. These relations suggest that the reconnection rate ηJ_0 should scale independently of resistivity. In Figure 4.8a, we show a computation of the reconnection rate, $\psi_t = \eta J_0$, during the first ten Alfvén times. It is clear that, although the time to achieve the maximum reconnection rate increases with reductions in η, the peak rates remain unchanged, in agreement with theory.

The energy decays by Ohmic dissipation and viscous dissipation. In this section, viscosity has been turned off so, the Ohmic dissipation

$$W_\eta = \eta \int J^2 dV$$

provides the only the avenue for energy release (see (3.47) in Chapter 3). Figure

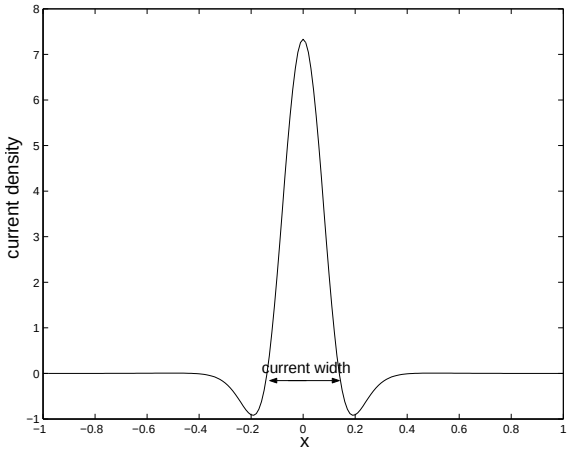

Figure 4.7: The measured current width of the current beam at the time of maximum peak current.

4.8b shows the change of Ohmic dissipation rate during the reconnection through 10 Alfvén times with various values of the resistivities. However, replacing dV by dA in our two dimensional case, substituting scale values $J \sim 1/\eta$ and $A_s \sim \eta$ into (3.47), both the analytical and computational results show no significant change of dissipation rate with resistivity.

4.3.4 Self-similar mode

After a sufficiently long time, the oscillations disappear and the system is again very close to its equilibrium neutral point configuration. The oscillatory decaying eigenmodes, which maintain equipartition between the magnetic and kinetic energies, are now absent. Figure 4.9 shows that there is clear separation between the magnetic and kinetic energies, as the oscillatory behaviour begins to weaken. Our results indicate that there is a monotonic decay of the kinetic energy but an oscillatory decay of the magnetic energy still persists (with $K >> M$).

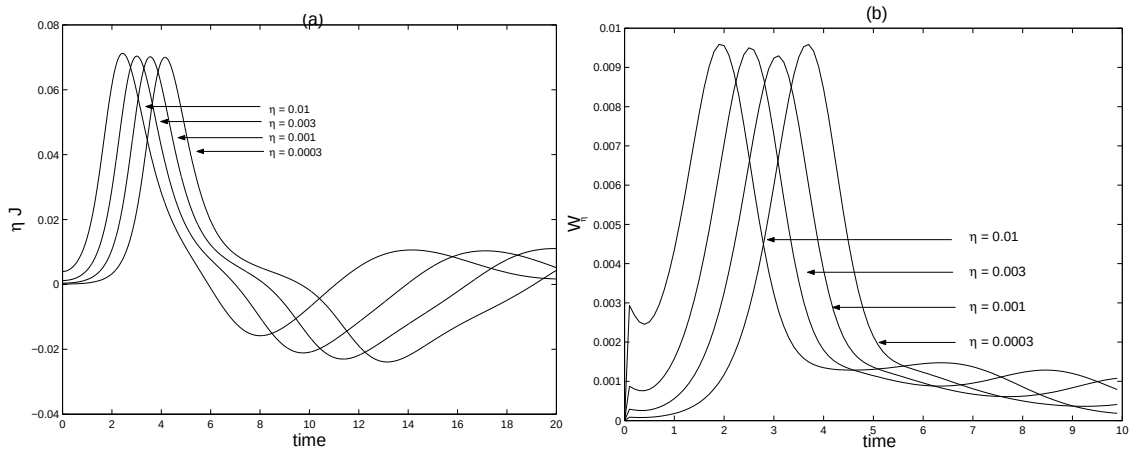

Figure 4.8: (**a**) The reconnection rate (ηJ_0) for various values of η. (**b**) The Ohmic dissipation rate over the entire domain for various values of η. The maximum dissipation rate and reconnection rate vary with time, but the peak value does not change with resistivity.

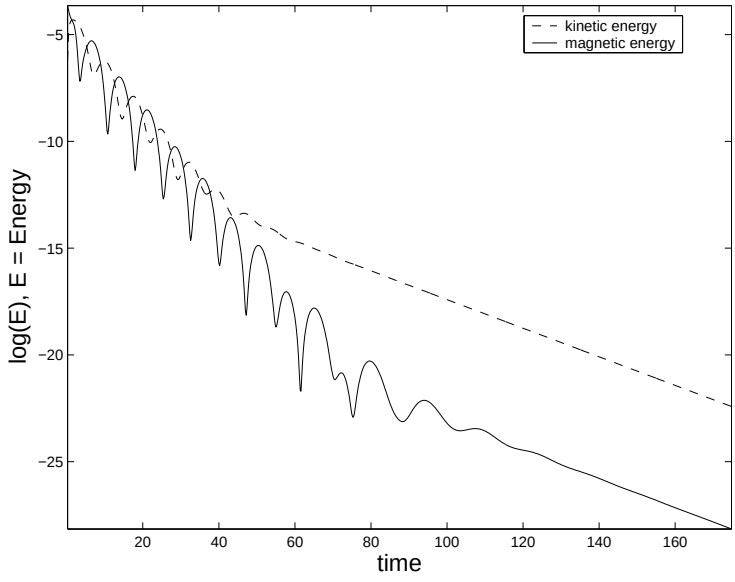

Figure 4.9: Time evolution of global magnetic energy (solid line) and kinetic energy (dashed line) over the region $-1 \leq x, y \leq 1$ for the reconnection disturbance field with $\eta = 0.003$.

A radial solution of (4.22) is given by (see (3.42) in §3.3.3)

$$\psi_m(r,t) = e^{\lambda t} f(r), \quad \lambda = \alpha + i\omega,$$

using the method of separation variables for the problem. The radial eigenmode solutions are not complete, so some other particular solutions may exit. Hence the radial eigenmode solution may not be satisfactory to describe the monotonic evolution. Hassam (1992) first presented the analysis of this large time behaviour of the perturbation field for the $n = 2$ cylindrical mode. According to Hassam, the decay of the similarity solution is slow and the similarity solution is relatively unimportant, since the bulk of the field disturbance (more than 99 percent) is generally dissipated before non-oscillatory behaviour can occur.

We demonstrate some scaling properties of the slow monotonic decay of the perturbation field. Under the assumption that $\psi_{tt} \to 0$ as $t \to \infty$, (4.22) gives

$$\nabla^2 \psi_t + \frac{\eta}{r^2} \nabla^2 \psi = 0 \tag{4.27}$$

with the solution

$$J(r,t) = J(r,0)\, \mathrm{e}^{-r^2 t/\eta}, \tag{4.28}$$

where $J(r,t) = -\nabla^2 \psi$ is current density. The linearized momentum equation (4.5) with $\nu = 0$ reduces to

$$\frac{\partial v}{\partial t} = -rJ(r,0)\, \mathrm{e}^{-r^2 t/\eta}, \tag{4.29}$$

if we set $|\nabla \psi| = r$. Integrating both sides over time t, gives

$$v = \frac{\eta}{r} J(r,0)\, \mathrm{e}^{-r^2 t/\eta} + C. \tag{4.30}$$

where C is arbitrary constant. Setting $v \to 0$, as $t \to \infty$ gives

$$v = \frac{\eta}{r} J(r,0)\, \mathrm{e}^{-r^2 t/\eta}, \tag{4.31}$$

and hence the local kinetic energy

$$\frac{1}{2} v^2 = \frac{\eta^2}{2r^2} J^2(r,0)\, \mathrm{e}^{-2r^2 t/\eta}. \tag{4.32}$$

The global kinetic energy K over the domain in the non-oscillatory phase now becomes

$$K = \int \frac{1}{2} v^2 dV = \int \frac{\eta^2}{2r^2} J^2 dV. \tag{4.33}$$

To provide a more detailed comparison for global kinetic energy in the non-oscillatory phase, $\psi_{tt} = 0$, we plot the analytic prediction (4.33) and numerical solution of (3.37) in the same Figure 4.10. The figure shows that the both plots overlap in the non-oscillatory phase. This figure also shows that only the kinetic energy contributes to the global energy during the stage of monotonic decay. The rate of change of kinetic energy over the domain from (4.33) is

$$\frac{\partial}{\partial t} \int \frac{1}{2} v^2 dV = -\eta \int J_0^2 \mathrm{e}^{-2r^2 t/\eta} \, dV = -\eta \int J^2 dV. \tag{4.34}$$

Figure 4.10 shows the total energy equal to the kinetic energy which means that the magnetic energy is completely decayed. Hence the pure resistive solution can remove magnetic energy but an excess kinetic energy component remains. These results encouraged us to examine the impact of the Hall current and viscous effects on magnetic reconnection solutions. The kinematic viscosity will be the dominant factor in removing kinetic energy from plasma and, as already noted, in solar plasmas, the kinematic viscosity is much higher than the classical collisional resistivity (Hollweg, 1986).

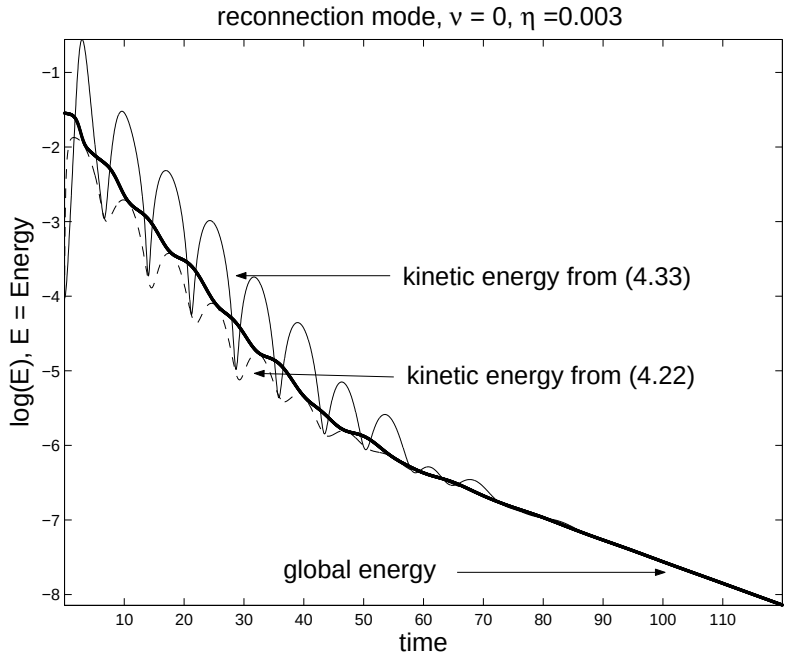

Figure 4.10: Figure shows that when $\psi_{tt} = 0$ there exists a slow decay in the non-oscillatory phase. The solid line shows the solution of (4.33). The dashed line represents the damping of kinetic energy (K) and the thick solid line gives the damping of total energy $(M + K)$ as the solution of (4.22) .

4.4 Viscous X-point solutions

The previous computations have demonstrated that the present resistive code with highly conducting square boundary can accurately reproduce the behaviour produced by the analytic cylindrical mode calculation. Our present aim is explore how effective viscosity is in removing the energy associated with X-point disturbances. The influence of the resistivity on the X-point problem, discussed in previous section, does not significantly depend on whether perturbation fields have a topological component. However in this section, it is important to distinguish between topological and non-topological modes. Although resistivity is required to account for the decay of topological components in the magnetic energy, we expect that viscosity can dissipate not only the kinetic energy, but also a significant fraction of the magnetic energy—the non-topological component—in the dynamically evolving plasma. We find that viscous damping also comprises the three phases: a period of rapid decay, a period of oscillatory decay, and finally slow monotonic decay.

We first consider the purely viscous decay of the non-reconnection mode, before considering the evolution of the reconnection mode.

4.4.1 Non-topological disturbance ($\nu > 0, \eta = 0$)

In the case of non-reconnective disturbances, viscous damping can be understood in much the same manner as resistive dissipation. Figure 4.11 compares the field strength on the x-axis at the time of maximum current density (the first 'bounce'), for various parameters. This figure displays remarkably similar ψ functions along the x-axis for both resistive and viscous damping. The main difference is the displacement of the ψ-field at the origin in the resistive case: of course, it is not possible to alter the value of ψ at the origin when only viscosity operates. For $\eta = 0$ therefore the field remains frozen in to the plasma and there can be no reconnection at any time.

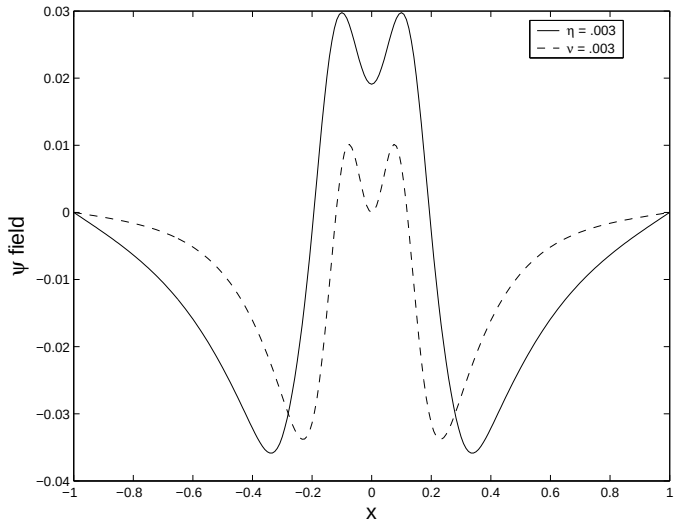

Figure 4.11: The ψ field on the x-axis at the time of maximum current for the non-topological disturbance. The solid line is for the run $\eta = 3 \times 10^{-3}$, $\nu = 0$ while the dashed line is for $\eta = 0,\ \nu = 3 \times 10^{-3}$. Note that $\psi(0, 0, t)$ field remains zero in the $\eta = 0,\ \nu = 3 \times 10^{-3}$ case. There is the same result along the y-axis.

Energy dissipation and oscillatory decay rate

Recall that the resistive theory based on the existence of cylindrical eigenfunction solutions which damp out at a rate $\alpha \simeq -\omega^2/2$, determined by the fundamental oscillation frequency $\omega \simeq \pi/|\ln \eta|$ (see §3.3). The oscillatory eigenmode solution is followed by an energetically insignificant "self-similar" mode, localized to the diffusion region (Hassam, 1992; Craig & McClymont, 1993). This solution mode is obtained by assuming that the advection of the magnetic field can be balanced by resistive energy dissipation.

Now we consider viscous energy dissipation in the case of negligible resistivity. Figure 4.12 shows that the initial rapid decline of the energy for $t < 10$ is followed by a stage of fast oscillatory decay in which the kinetic and magnetic energies continually interchange, when $10 < t < 30$. After that there is a clear separation between the magnetic and kinetic energy components of the plasma. The final phase

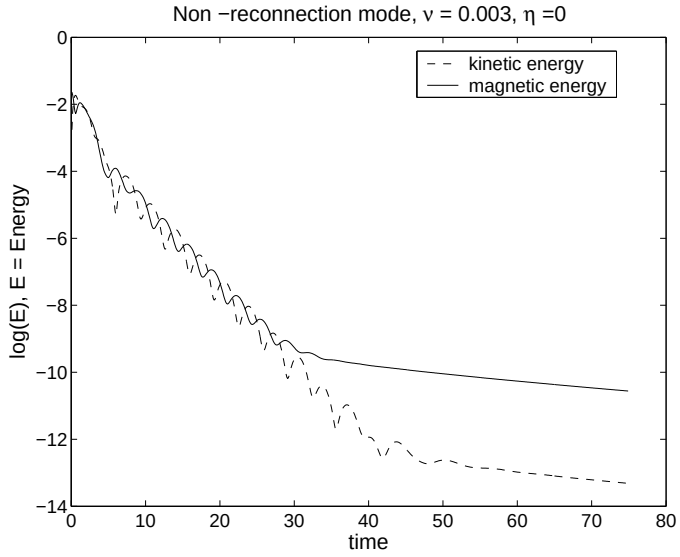

Figure 4.12: The decay of the disturbance field energy for initial conditions of Figure 4.1b. The results show the spatially integrated kinetic and magnetic energies for the fluid for $\nu = 10^{-3}, \eta = 0$.

is characterized by a slow decline involving the weak non-oscillatory separation of the kinetic and magnetic energy components of the plasma. In this phase, both fields have an equal monotonic decay rate. It is clear that viscosity resists the fluid motion, and can therefore damp kinetic energy faster than magnetic energy. Therefore excess magnetic energy remains when only viscous dissipation is present. In general, the initial rapid decay is independent of both the viscosity and resistivity but the computation of Figure 4.13 shows that in the second phase, the viscous oscillatory dissipation rate is faster than the resistive dissipation rate (for run $\eta = 0$, $\nu = 0.003$ and $\eta = 0.003$, $\nu = 0$).

Figure 4.14 shows a comparison of numerically computed viscous oscillatory decay rates with resistive oscillatory decay rates for the run of Figure 4.1b for non-reconnection mode. The plots of $\ln(\alpha_\nu)$ versus $\ln(\nu)$, and $\ln(\alpha_\eta)$ versus $\ln(\eta)$ give the same slope but faster viscous dissipation compared to resistive dissipation. In

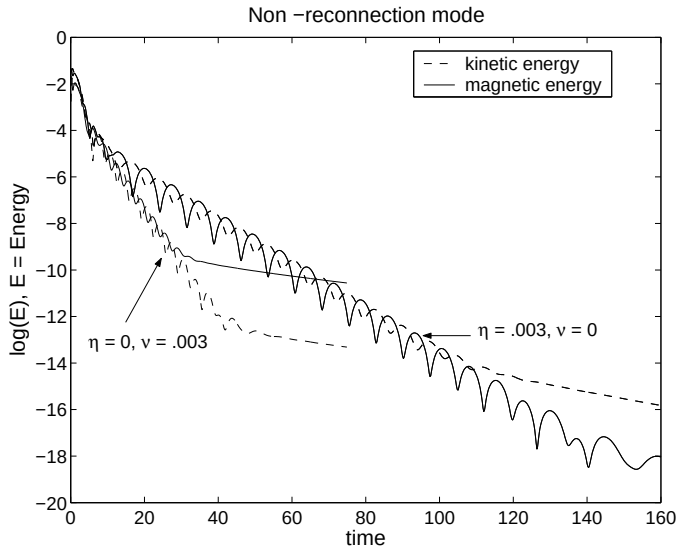

Figure 4.13: Result of the fitting process to both viscous dissipation (Figure 4.12) and resistive dissipation (Figure 4.4).

the resistive case, the field lines oscillate at the X-point but in the viscous case the field lines are tied (see Figure 4.11). It follows that $\alpha_\nu > \alpha_\eta$ where α_ν and α_η are the viscous and resistive decay rates respectively. This behaviour can be understood if we assume that viscosity acts in an analogous way to the resistivity. This interpretation holds good for non-reconnective modes typified by Figure 4.12.

4.4.2 Viscous topological disturbance

The arguments given above cannot explain the monotonic energy decline for topological disturbances. Consider Figure 4.15 which shows the viscous damping of the reconnective disturbance

$$\psi(x, y, 0) = (1 - x^2)(1 - y^2)$$

when $\nu = 0.001$, $\eta = 0$. Figure 4.16 shows, viscosity alone cannot alter the ψ function at the origin which therefore remains constant for all time. This mean that a reconnection mode gives significantly different behaviour as far as energy damping is

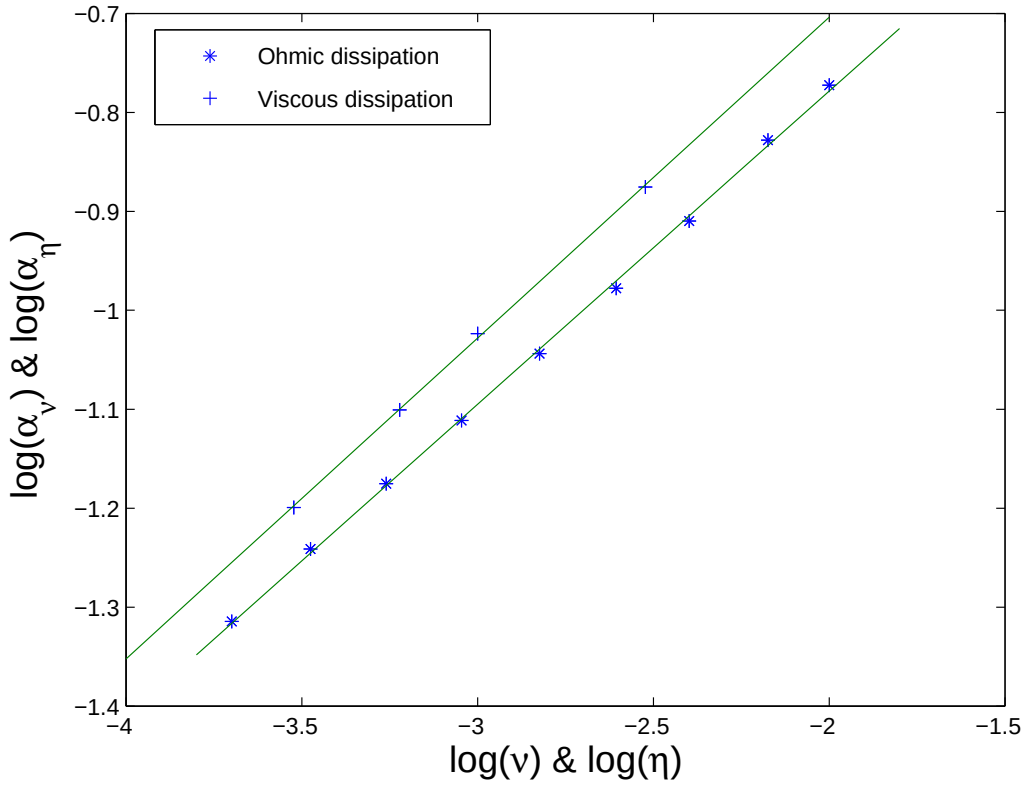

Figure 4.14: Scalings of the viscous damping rate and resistive damping rate for a non-topological mode. The set of runs depicted by '$*$' shows Ohmic dissipation and '$+$' shows viscous dissipation ($\alpha_\nu \simeq 1.4\,\alpha_\eta$).

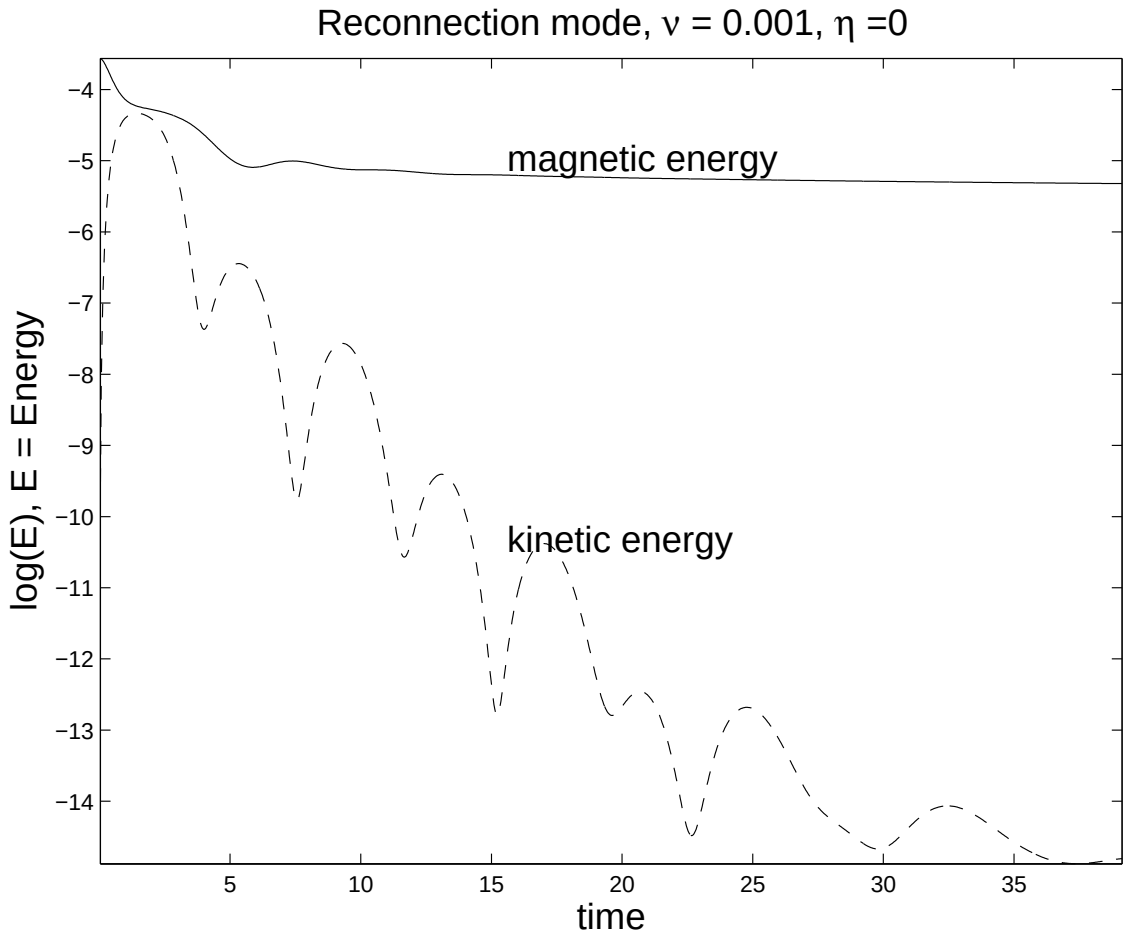

Figure 4.15: The decay of the disturbance field energy for the initial conditions of Figure 4.1c. The plot shows the spatially integrated kinetic and magnetic energies for $\eta = 0$, $\nu = 10^{-3}$. The solid line represents the damping of magnetic energy and dashed line represent the kinetic energy.

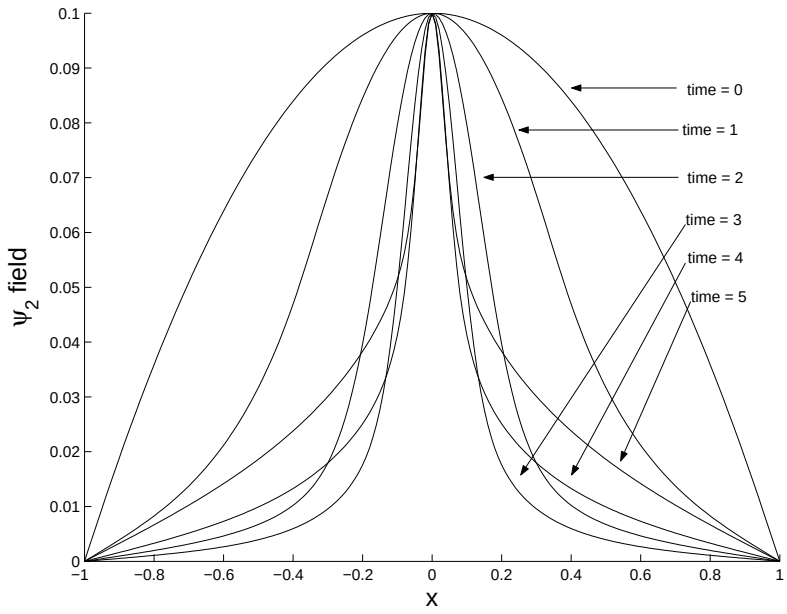

Figure 4.16: The value of ψ along the x-axis for Alfvén times $t = 0, 1, 2, 3, 4, 5$. The plot is for the run $\eta = 0$, $\nu = 3 \times 10^{-3}$ for the topological mode.

concerned. Viscous dissipation can typically remove more than half the energy from the fluid in the first phase, but in later phases, magnetic energy cannot be removed. Thus the wave motion of the fluid rapidly transfers magnetic energy into plasma kinetic energy for $t < 2$, but the later phase is characterized by non-equipartition with rapid separation of the kinetic and magnetic energy components. In particular, the constant magnetic energy contrasts with the much faster oscillatory decline of the global kinetic energy (Figure 4.15).

4.5 Visco-resistive X-point solutions

We now explore the X-point evolution when both resistivity and viscosity act together. There are three cases to consider:

$$\nu < \eta, \quad \nu \simeq \eta \quad \text{and} \quad \nu > \eta$$

for each of the two disturbance fields. We begin with a discussion of the non-topological disturbance in the presence of both viscosity and resistivity.

4.5.1 Non-topological disturbance; $\nu > 0$, $\eta > 0$

When viscosity and resistivity are both present, significant new phenomena emerge. The computational results in Figure 4.17 represent the time evolution of magnetic and kinetic energy decay for six values of η with ν fixed. Each plot displays the non-reconnective perturbation for 20 Alfvén times. In the first stage ($t < 2$), all plots show more than half of the free magnetic energy is removed by both resistive and viscous effects. In the case $\eta < \nu$, Figures 4.17a and b show that the equipartition of magnetic and kinetic energies is established in the second stage. Figures 4.17c and d, when $\eta \simeq \nu$, show that the oscillatory behaviour associated with energy equipartition has begun to disappear. The solution is characterized by the monotonic decay of both the magnetic and kinetic energies, apart from oscillations with a very small amplitude in the magnetic energy. If the resistivity is increased further, $\eta > \nu$, oscillatory behaviour and equipartition re-emerge (see Figures 4.17e and f). We also can see in Figure 4.17, an enhanced energy dissipation rate when resistivity and viscosity are of the same order. Figure 4.18 shows the oscillatory energy decay rate is increased by increasing η, and achieves its maximum rate when $\eta \simeq \nu$.

To summarize, these results show that viscous-resistive damping is very efficient at removing the most of the excess energy in the fluid within a few Alfvén times when non-reconnective modes are involved. Some separation of the energy components

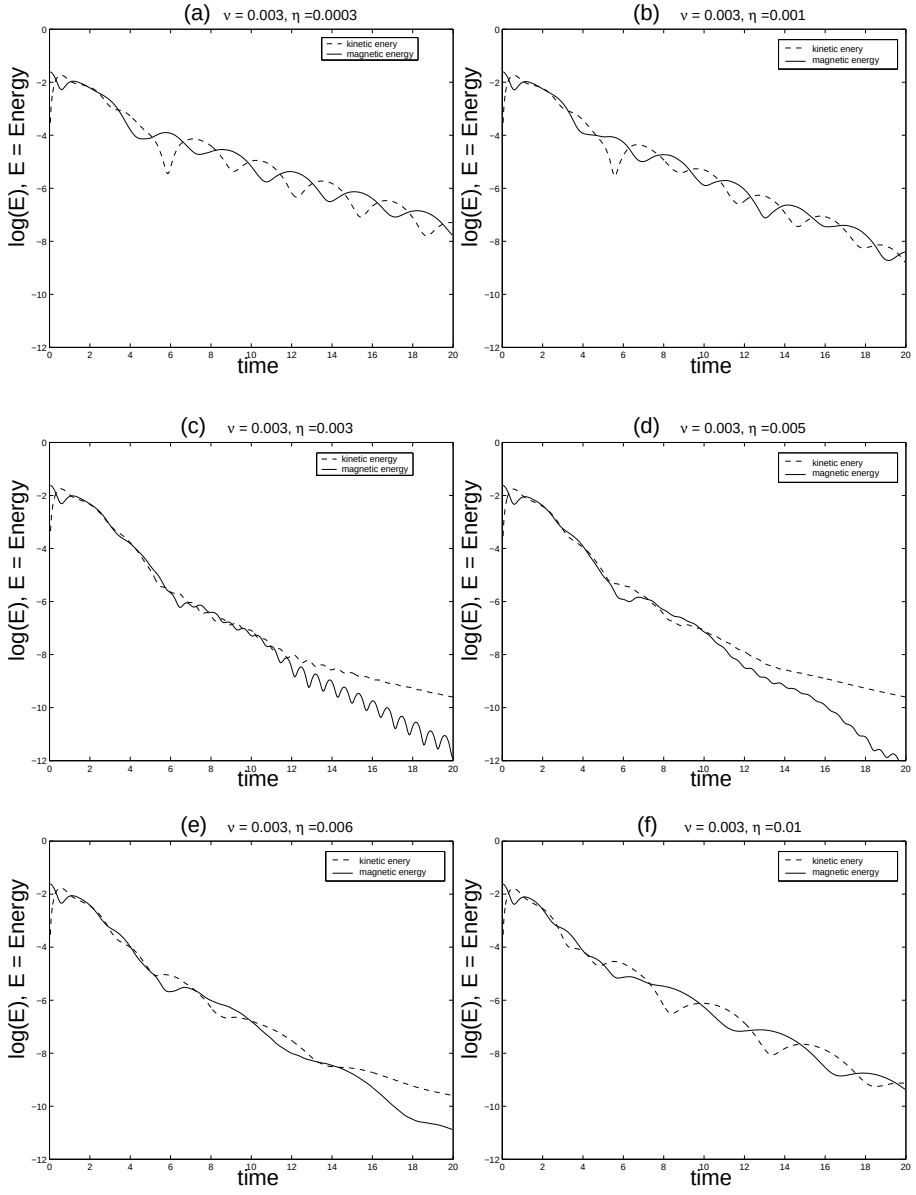

Figure 4.17: The decay of the disturbance field energy for the initial conditions of Figure 4.1b. The plots display the magnetic (solid lines) and kinetic (dashed lines) energies for various values of η with ν fixed. Figures 4.17a and b display the energy dissipation when $\eta < \nu$, Figures 4.17c and d when $\eta \simeq \nu$ and Figures 4.17e and f when $\eta > \nu$.

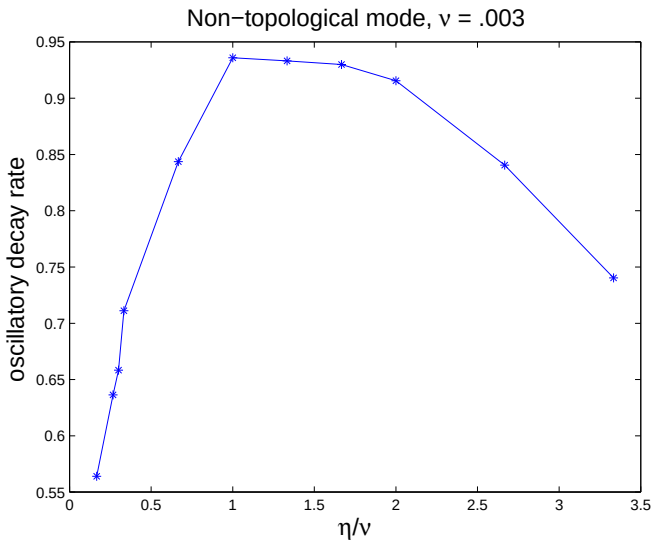

Figure 4.18: Plot of the oscillatory decay rate of magnetic energy for variety of η/ν with ν is fixed. The plot is demonstrating the maximum dissipation rate obtained when η and ν are of the same order.

does occur, but only after the initial energy has been reduced by a factor approaching 10^6.

4.5.2 Topological disturbance; $\nu > 0$, $\eta > 0$

Here we discuss the visco-resistive coupling process for the reconnection mode in two ways. First we consider a range of values of the resistivity with $\nu = 0.003$ (see Figure 4.19). The run with $\eta < \nu$, in particular, shows a slow monotonic decline of the magnetic energy, in contrast with a much faster oscillatory decline of the global kinetic energy. As η is increased, we find that the decline of the magnetic energy follows a non-oscillatory decay law of the form $\exp(-\gamma t)$, with $\gamma \simeq \eta^{1/2}$. The resulting energy separation reflects the fact that viscous damping cannot remove the topological energy of the disturbance: the separation is most apparent when $\eta \ll \nu$, but begins to break down as η increases (Figure 4.19b). The energy decay when

$\eta = \nu$ is shown in Figure 4.19b. The case $\eta \simeq \nu$ appears to be unique in the sense that the solution is characterized by the slow monotonic decay of both the magnetic and kinetic energies, apart from very small amplitude oscillations in the magnetic energy similar to the non-topological case. If the resistivity is increased further ($\eta > \nu$), the oscillatory behaviour of the magnetic energy re-emerges (Figure 4.19c). A separation of the kinetic and magnetic energies occurs at large times, $t > 40$, when the global energy is essentially insignificant. However, in this case, the bulk of the excess energy now resides in the kinetic, rather than the magnetic part of the total energy.

Figures 4.20a and b show a comparison of energy decay of the non-topological and topological perturbations respectively. Figure 4.20a provides evidence that more than 95% of the energy can be converted to heat by both Ohmic and viscous dissipation, within a short period of rapid decay. Figure 4.20b shows that for a topological perturbation only part of the initial energy is removed over the same period. In the second stage, resistivity can dissipate the remaining energy but viscosity cannot. The doted line of Figure 4.20b shows the effects of including both viscosity and resistivity; almost all magnetic and kinetic energy dissipates within 4 Alfvén times at a rate similar to that of the non-reconnection mode.

If viscosity couples with resistivity, the dashed line shows that the total energy dissipates at a similar rate to the non-topological mode.

4.6 X-point scaling laws

In §4.3 and §4.5, some qualitative properties of the X-point problem have been described using the model developed in §4.2. This section presents some quantitative predictions of scaling laws, using approximate matching arguments involving the viscosity.

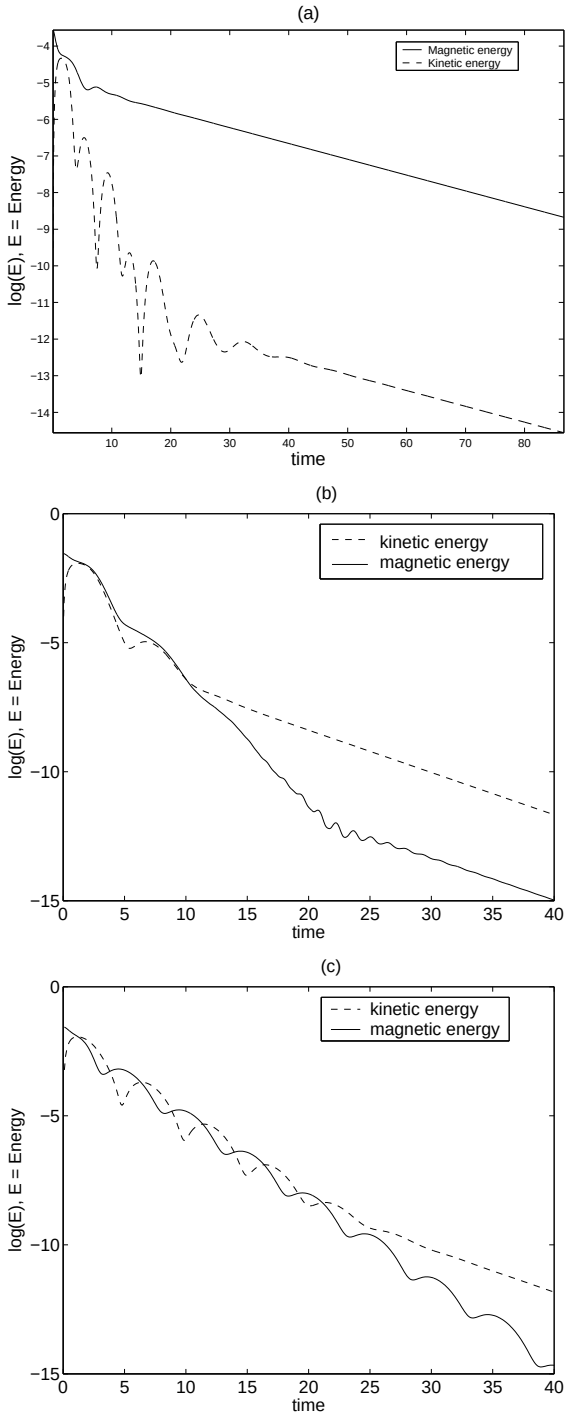

Figure 4.19: The decay of the disturbance field energy for the initial conditions of Figure 4.1c for a non-oscillatory disturbance. The decay of magnetic and kinetic energy dissipations for (**a**) $\nu = 0.003$, $\eta = 0.001$ ($\eta < \nu$), (**b**) $\nu = \eta = 10^{-3}$, (**c**) $\nu = 0.001,\ \eta = 0.003$ ($\eta > \nu$).

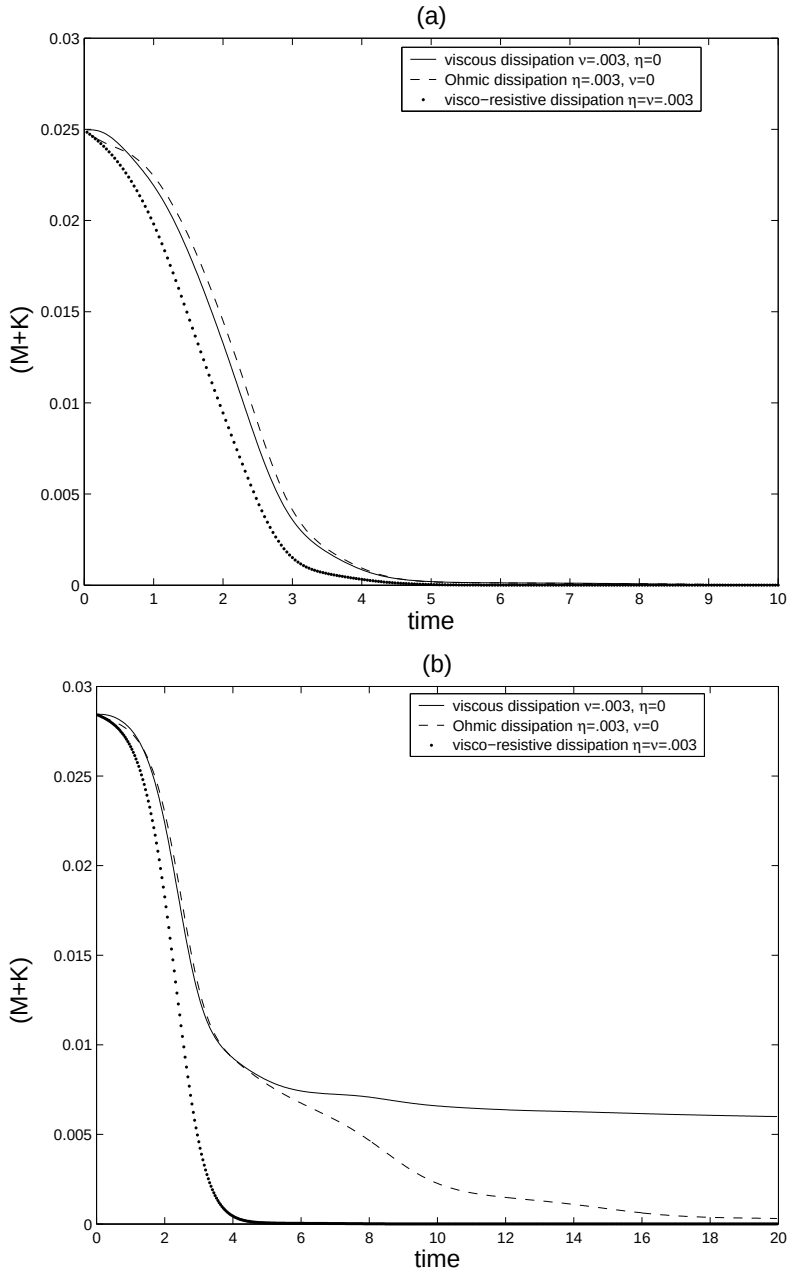

Figure 4.20: The global magnetic and kinetic energy $(M+K)$ versus time for (**a**) the non-topological perturbation field and (**b**) the topological perturbation field. The dashed lines represent the resistive dissipation, solid lines the viscous dissipation and dotted lines the visco-resistive dissipation.

4.6.1 The visco-resistive length scale

We have seen that currents originated into a quasi-cylindrical tube overlying the neutral point, can produce a rapid conversion of magnetic energy into heat via resistive dissipation. The width of the current layer is characterized by the distance to the peak of the magnetic field component aligned with the quasi-cylindrical current tube. The resistive length scale of the current layer is $r_s \sim \eta^{1/2}$; the corresponding maximum current density scales as $J_0 \sim \eta^{-1}$ at the origin and the Ohmic dissipation rate is fast, $W_\eta \sim \eta^0$ (see Figures 4.8a and b). In typical plasmas, the very large conductivity ($\eta \simeq 0$) implies that the dissipation is so small that the magnetic field is almost completely "frozen into the plasma" which implies that very small length-scales must develop in the magnetic field. However, it seems that in these circumstances, collisional conditions are likely to be violated.

The simultaneous presence of viscosity and resistivity adds another spatial scale which allows an extra channel for the energy dissipation. This is because the viscous and resistive terms are capable of balancing the Lorentz force and advection, respectively. Recall that (4.5) and (4.6) define the X-point system:

$$\begin{aligned} \partial_t \mathbf{v} &= -\nabla^2\psi\nabla\psi_E + \nu\left[\nabla^2\mathbf{v} + \frac{1}{3}\nabla\left(\nabla\cdot\mathbf{v}\right)\right], \\ \partial_t \psi &= -\mathbf{v}\cdot\nabla\psi_E + \eta\nabla^2\psi, \end{aligned}$$

with $\psi_E = -0.5(x^2 - y^2)$. Balancing the terms on the right hand sides of these equations leads to the order-of-magnitude relationships respectively:

$$\frac{\psi}{r_s} \simeq \frac{\nu v}{r_s^2}, \quad v r_s \simeq \frac{\eta\psi}{r_s^2}, \tag{4.35}$$

which gives the new visco-resistive length scale $r_s = (\eta\nu)^{1/4}$. The emergence of this scale in viscous reconnection problems has been noticed by Park et al. (1984) and Hassam & Lambert (1996).

We have investigated how viscosity affects the properties of the current localization for both reconnection and non-reconnection modes. Figures 4.21a and b

show a plot of $\log(\eta\nu)$ versus the length scale $\log(r_s)$ at the time of maximum current. We have measured the current width along the x-axis as shown in Figure 4.7. The measured slope, (0.25), confirms that the visco-resistive scale is $r_s = (\eta\nu)^{1/4}$. The current scales as $J_0 \sim (\eta\nu)^{1/4}$ which shows the combination of resistive and viscous effects when both $\eta, \nu > 0$. Our numerical results confirm that the visco-resistive coupling is most prominent when $\eta \sim \nu$. As an example, Figure 4.21 shows how closely the length scale r_s follows the scaling $r_s \sim (\eta\nu)^{1/4}$, where the range is $0.5 < \frac{\eta}{\nu} < 5$. Figure 4.22 confirms that run for non-reconnection mode, viscosity limits the thickness of current structures to scales of order $\sqrt{\nu}$ and current density to scales of order $J \sim \nu^{-1}$ when $\eta = 0$.

Figures 4.23 and 4.24 show a comparison of the viscous and resistive simulations for the non-topological mode and the reconnection mode respectively. In the non-reconnection mode, both resistive and viscous solutions give oscillatory behaviour of the current density at the neutral point (Figure 4.23). In the viscous case, the behaviour of the current density implies that the magnetic field is frozen into a purely conductive plasma. However, in the case of the topological mode, shown in Figure 4.24, the current density (dashed line) consistently increases when $\eta = 0,\ \nu = 3 \times 10^{-3}$ in the highly conductive plasma. Presumably, the final value for the current density is due to the finite numerical resolution of the computation (Pontin & Craig, 2006). Figure 4.24 illustrates that resistivity is essential in arresting this kind of singular behaviour.

4.6.2 The scalings of Ohmic and viscous dissipation rates

Recall that Ohmic and viscous dissipation rates for the X-point problem are given by (4.16). Equation (4.9) indicates that the total global energy decay rates is given by sum of the Ohmic and viscous dissipation contributions. Also note that almost all the initial energy decays within few Alfvén times. Therefore it is important to

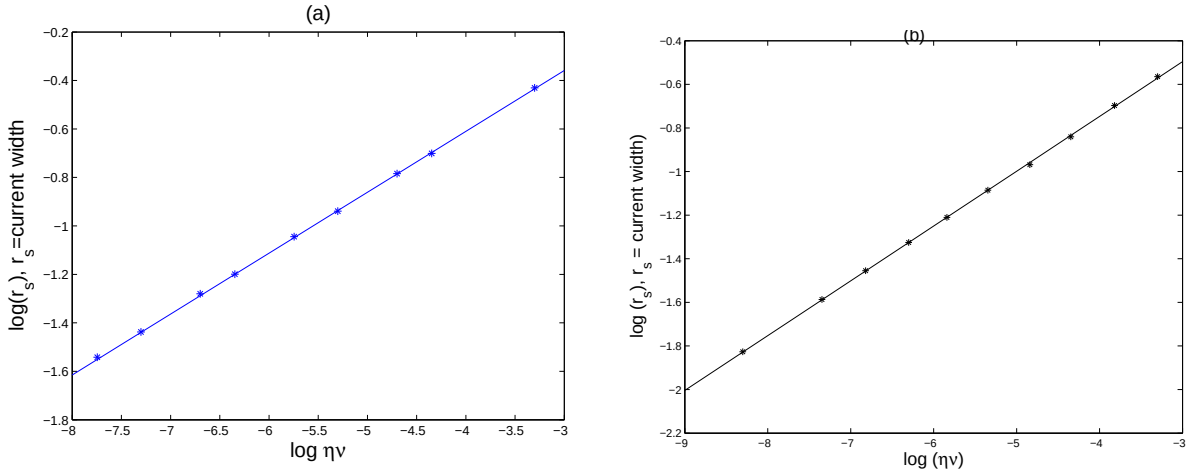

Figure 4.21: When both η and ν are greater than zero and of the same order, the length scales $r_s \sim (\eta\nu)^{1/4}$ with range of $0.5 < \eta/\nu < 5$. Figures 4.21a and b represent the reconnection mode and the non-reconnection mode respectively.

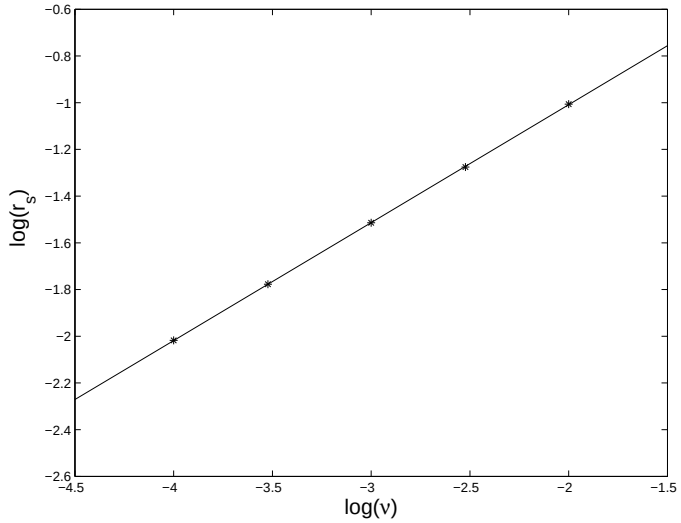

Figure 4.22: The viscous dissipation gives length scales $r_s \sim \nu^{1/2}$ when $\eta = 0$ for the non-reconnection mode.

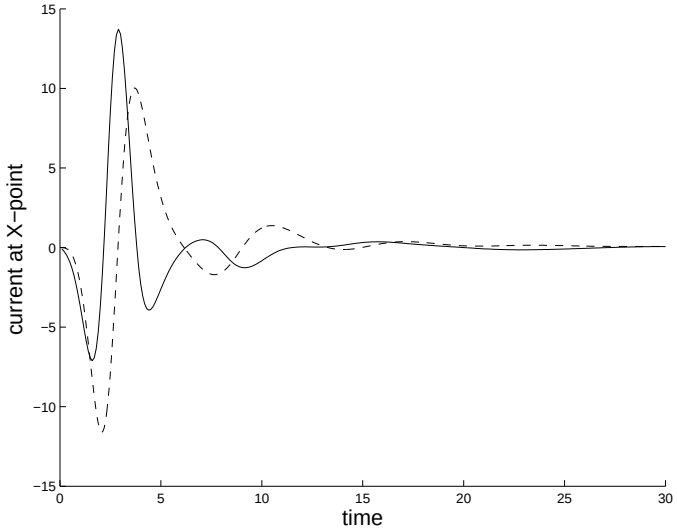

Figure 4.23: The current densities at the neutral point for initial conditions of Figure 4.1b (non-topological mode). The solid line indicates the run $\eta = 3 \times 10^{-3}, \nu = 0$, while dashed line is for $\nu = 3 \times 10^{-3}, \eta = 0$.

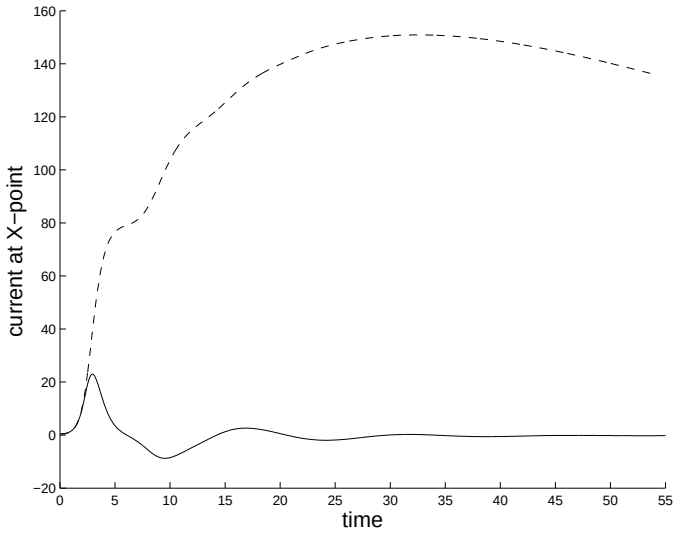

Figure 4.24: The current densities at the neutral point for initial conditions of Figure 4.1c (topological mode). The solid line indicates the run $\eta = 3 \times 10^{-3}, \nu = 0$, while dashed line is for $\nu = 3 \times 10^{-3}, \eta = 0$.

study the contribution of the resistivity and the viscosity for the energy decay during this short time period. Figure 4.25a shows that for a non-reconnection mode, the time variation of viscous dissipation and resistive dissipation rates are similar. In both cases the bulk of the perturbation energy is damped out by $t \sim 6$. However, for the reconnection mode, shown in Figure 4.25b, in the initial stage ($t < 4$) both viscosity and resistivity can dissipate energy comparable rates, but in the later stage viscous dissipation rate becomes ineffective. Resistivity can dissipate the remaining energy in the oscillatory stage, but viscosity cannot.

In Figure 4.26a and b we plot the Ohmic dissipation rate for various values of ν with η having the fixed values 0.003, for a non-topological perturbation and a topological perturbation respectively. Note that the Ohmic dissipation rate is reduced by the presence of viscosity. This effect is consistent with the scaling of the Ohmic dissipation rate when $\eta, \nu > 0$. The axial current density, given by $J = |\nabla^2 \psi|$ in the diffusion region, will scale as

$$J \sim \frac{\psi^i}{r_s}$$

where $\psi^i \sim 1$ is the inner field and $r_s = (\nu\eta)^{1/4}$ is the visco-resistive length scale (see §4.6.1). The behaviour of the Ohmic dissipation rate will be given by

$$\begin{aligned} W_\eta &\simeq \eta J^2 A_s \text{ with } A_s = \pi r_s^2 \\ &\simeq \eta \frac{\psi^2}{r_s^4} \pi r_s^2 \\ &\simeq \frac{\eta}{(\nu\eta)^{1/2}} \\ &\simeq \left(\frac{\eta}{\nu}\right)^{1/2}. \end{aligned}$$

The scale of W_η above gives the interesting results that the Ohmic dissipation rate is decreased by viscosity. Figures 4.26a and b, show this behaviour for both reconnection and non-reconnection modes. On the other hand Figures 4.27a and b show not surprisingly that the viscous dissipation rate is increased as ν increases. Figures

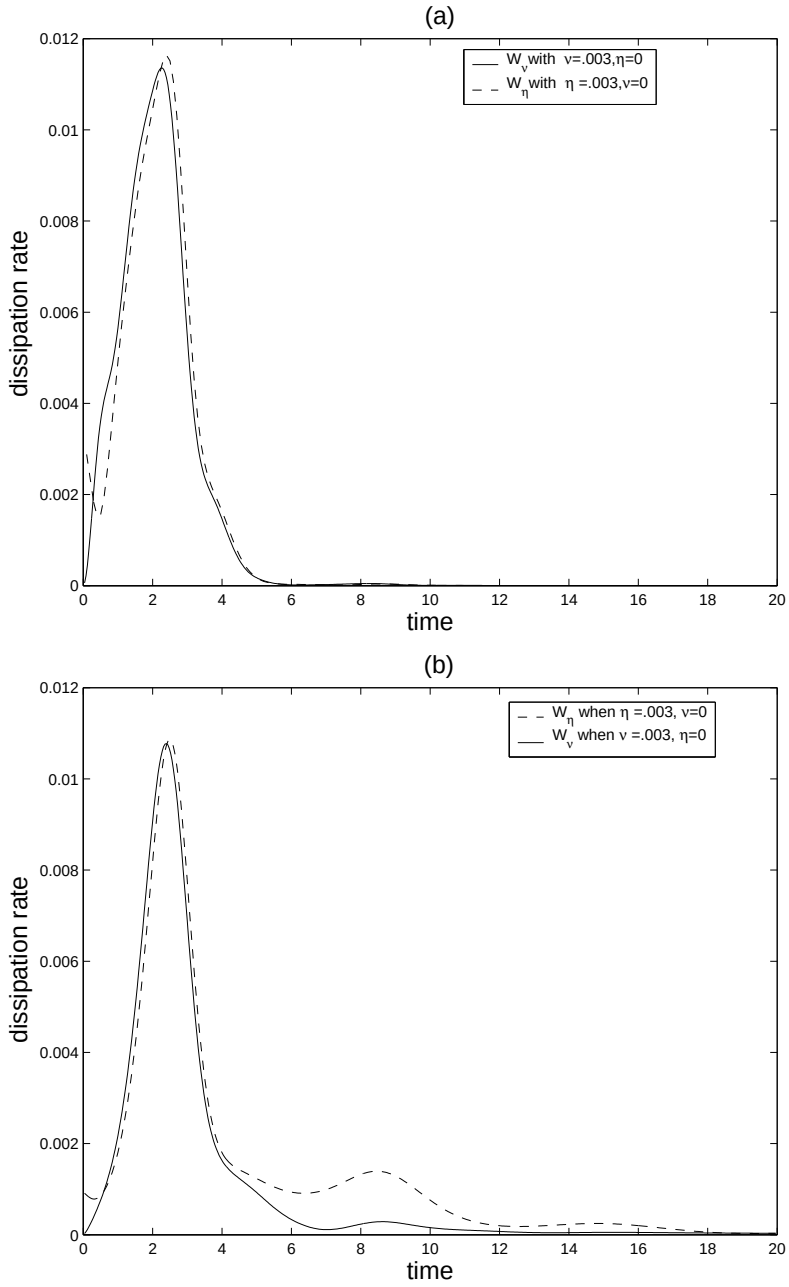

Figure 4.25: The viscous dissipation when $\nu = 0.003$, $\eta = 0$ (solid lines) and Ohmic dissipation when $\eta = 0.003$, $\nu = 0$ (dashed lines) for (**a**) the non-reconnection mode and (**b**) the reconnection mode.

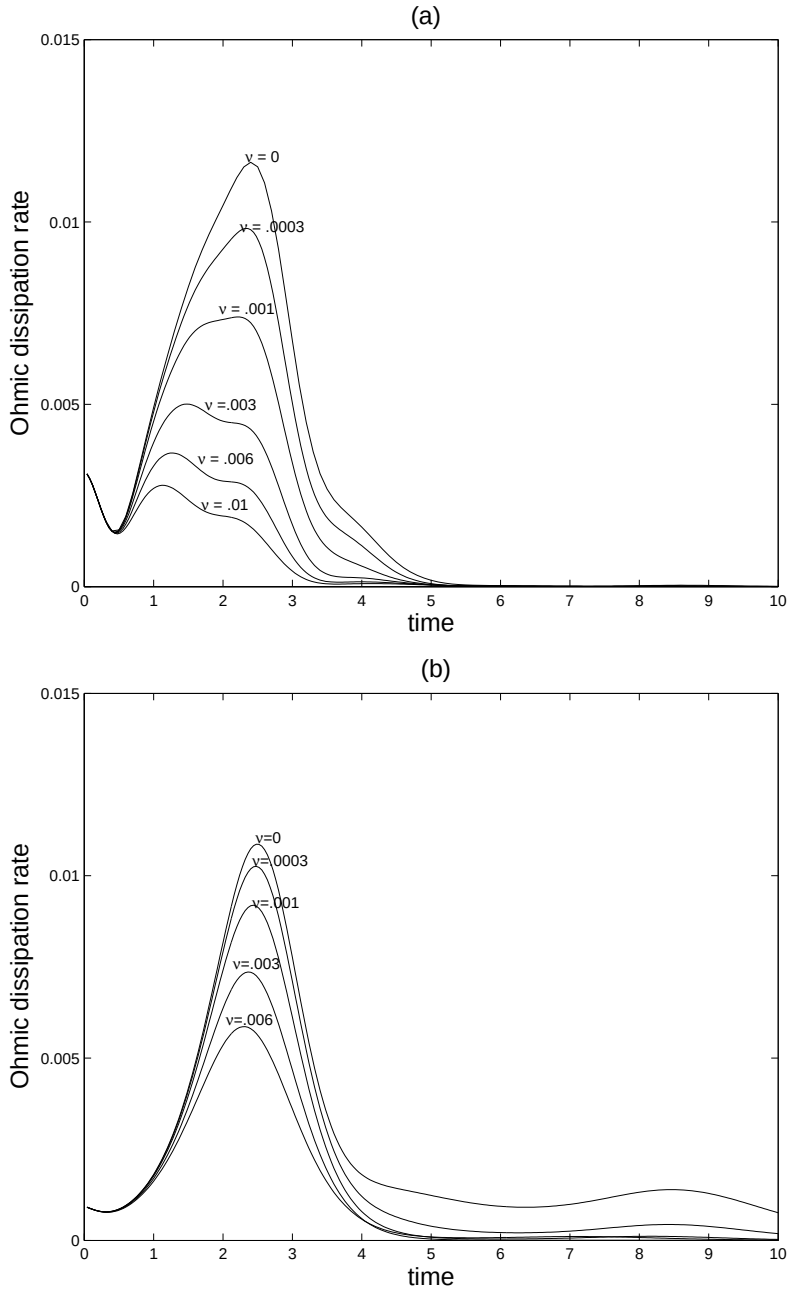

Figure 4.26: The variation of Ohmic dissipation rate with viscosity for (**a**) the non-topological perturbation and (**b**) topological perturbation with $\eta = 0.003$ is fixed.

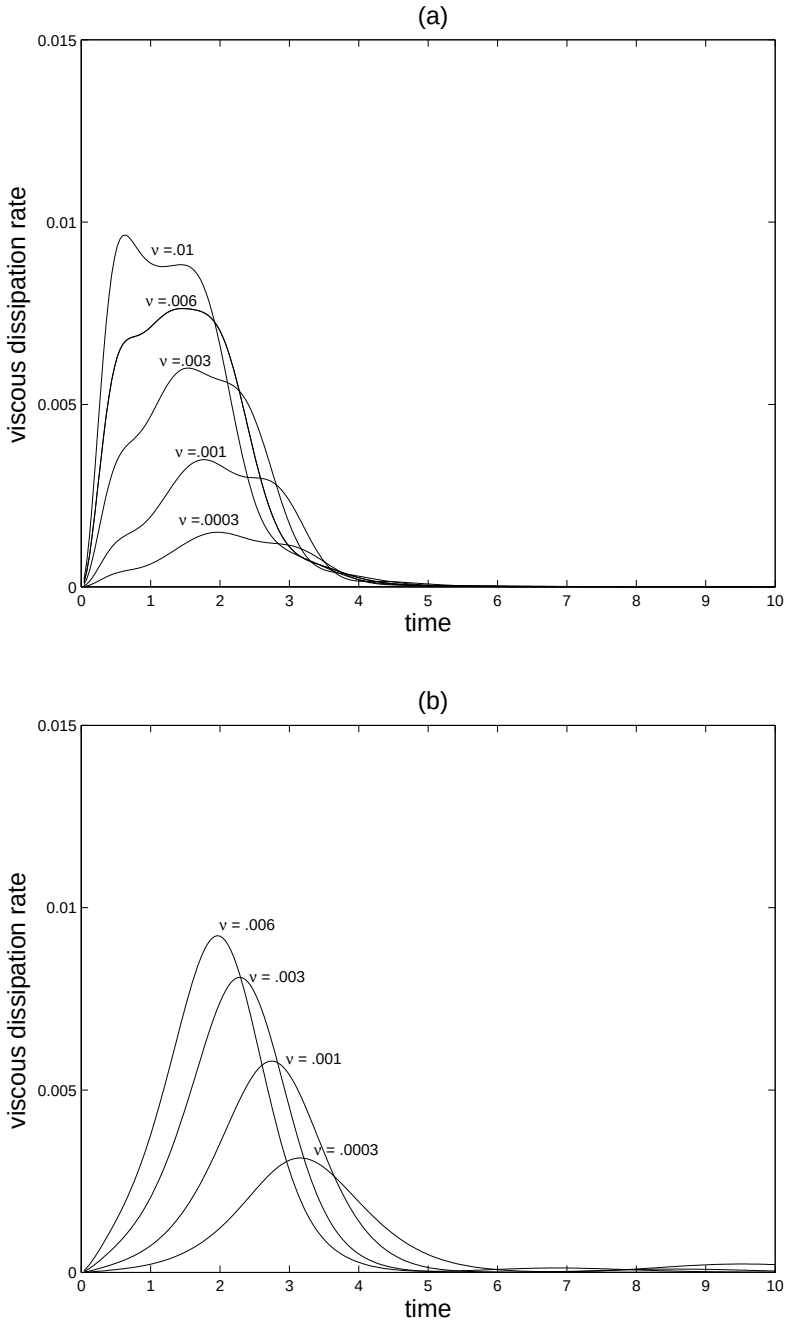

Figure 4.27: The variation of viscous dissipation rate with viscosity for (**a**) the non-topological perturbation and (**b**) topological perturbation with $\eta = 0.003$ is fixed.

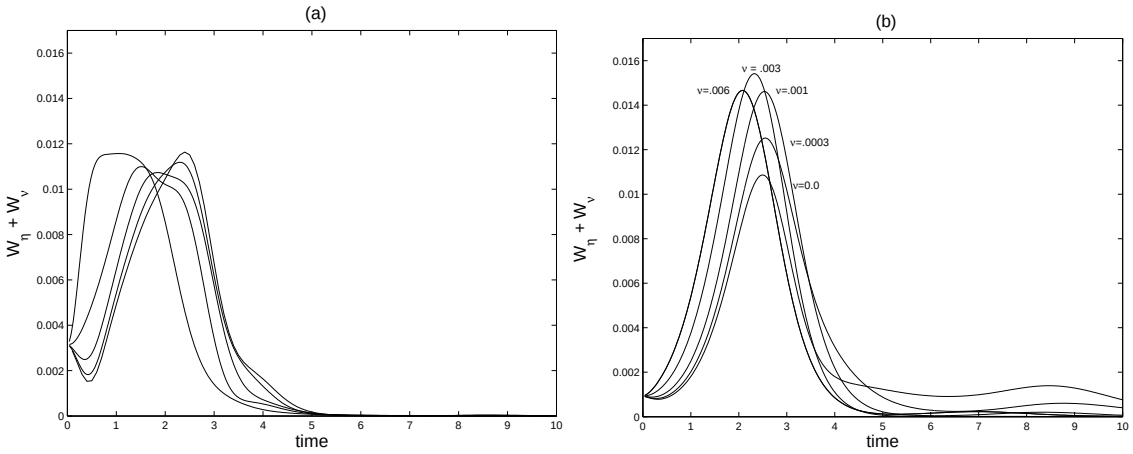

Figure 4.28: The plots show the total dissipation rate versus time for (**a**) non-topological perturbation and (**b**) topological perturbation for variety of ν with $\eta = 0.003$ is fixed.

4.28a and b, give comparable results—they show that viscosity can accelerate the total dissipation rate in the case of a topological disturbance field. In the case of non-reconnection mode, however, it is clear that, although the time to achieve the maximum dissipation rate changes with viscosity, the peak rates remain unaffected by viscosity.

4.6.3 Visco-resistive monotonic decay scaling for $\nu > 0$

The computational results of §4.3.4 indicate that one of most important properties of the X-point problem is the breakdown of equipartition followed by a stage of monotonic decay. We have discussed the monotonic decay of M and K for the resistive case (§4.3.4) in which oscillatory decay of kinetic energy died down and equipartition between M and K vanished as in Figure 4.9. Also we have seen that in the case $\nu > 0$, there is an early disappearance of oscillatory decay for the magnetic energy (see Figure 4.12). In this section we give an approximate matching

argument to deduce the scaling of the monotonic decay rate of the final phase for $\nu > 0$ including effects of the resistivity.

We consider monotonic decay for the global magnetic energy (M), global kinetic energy (K) and the potential field (ψ). We study M and K globally and ψ at the X-point. These monotonic decay rates play different roles, depending on the values the resistivity and viscosity, that is whether $\eta > \nu$ or $\eta < \nu$. Let us assume that the monotonic decay gives the eigenfunction descriptions of flux function ψ and velocity field v as

$$\psi \sim e^{-\alpha t}, \qquad v \sim e^{-\alpha t} \ \text{ as } \ t \longrightarrow \infty, \tag{4.36}$$

where α is the decay rate. Substituting these forms into the momentum (4.5) and induction (4.6) equations gives

$$-\alpha \mathbf{v} = -\nabla^2 \psi \nabla \psi_E + \nu \nabla^2 \mathbf{v} \tag{4.37}$$

and

$$-\alpha \psi = -\mathbf{v} \cdot \nabla \psi_E + \eta \nabla^2 \psi. \tag{4.38}$$

Monotonic decay rate in the case $\nu >> \eta$

In the case $\nu >> \eta$, the final phase gives the inequality $|\nabla \psi| >> |\mathbf{v}|$, because of the very rapid damping of the velocity field compared to the magnetic field. According to our boundary conditions, the inner and outer field can have the values $\psi^i \sim 1$ and $\psi^o \sim \ln r$ respectively where $r \leq 0(1)$. Therefore in the advection region (see §4.3), (4.38) gives the scaling of the outer velocity

$$v^o = \alpha \frac{\psi^o}{r}\,. \tag{4.39}$$

In the diffusion region ($r < r_s$), (4.37) gives the scaling of the inner velocity

$$v^i = \frac{r\psi^i}{\nu} = \frac{r}{\nu} \tag{4.40}$$

η	ν	$\lvert\alpha\rvert$	$\lvert\alpha_A\rvert$
1×10^{-5}	1×10^{-3}	0.0217	0.0217
1×10^{-4}	1×10^{-3}	0.0796	0.0785
1×10^{-4}	3×10^{-3}	0.0486	0.0486
5×10^{-4}	1×10^{-2}	0.0745	0.0733
5×10^{-4}	2×10^{-2}	0.0558	0.0549

Table 4.1:

by comparing terms $\nabla^2\psi\nabla\psi_E$ and $\nu\nabla^2\mathbf{v}$. We can assume for some $r > r_s = (\nu\eta)^{1/4}$

$$\frac{r}{\nu} \to \alpha\frac{\psi^o}{r} = \alpha\frac{\ln r}{r}, \tag{4.41}$$

and hence the monotonic decay rate is

$$\alpha \simeq \frac{(\eta/\nu)^{1/2}}{|\ln(\nu\eta)^{1/4}|} = \frac{(\eta/\nu)^{1/2}}{|\frac{1}{4}\ln(\nu\eta)|}\ , \tag{4.42}$$

where r_s is the visco-resistive length scale. Table 4.1 shows a comparison of some numerically computed decay rates α and their analytic estimates α_A given by (4.42) for $\nu > \eta$. These results are satisfied for both the reconnection and non-reconnection modes.

We know in general the energy separation is followed by a monotonic decay of the magnetic and kinetic energies at the same rate. In the case $\nu >> \eta$, (4.40) reduces to

$$v^i \sim \frac{r^2}{\nu}B^i \tag{4.43}$$

where

$$B^i \simeq \frac{\psi^i}{r}$$

is the magnetic field scale. Substitution of the visco-resistive length scale $r_s = (\eta\nu)^{1/4}$ leads to

$$M \sim \frac{\nu}{\eta}K\ , \tag{4.44}$$

where

$$M = \int \frac{1}{2} B_m^2 dV \quad \text{and} \quad K = \int \frac{1}{2} v_s^2 dV.$$

Our numerical results show that in the final phase, excess magnetic energy (M) and kinetic energy (K) are related by

$$M \simeq \frac{4\nu}{\eta} K \tag{4.45}$$

for $\nu > \eta$, which is consistent with the scaling of (4.44).

Monotonic decay rate in the case $\eta \geq \nu$

Alternatively, in the case $\eta \geq \nu$, in the advection region, (4.38) gives the scaling of the outer velocity

$$\frac{v^o}{\psi^o} \sim \frac{\eta}{r^3} \tag{4.46}$$

and in the diffusion region ($r < r_s$), (4.37) reduces to

$$\frac{v^i}{\psi^i} \sim \frac{1}{\alpha r} \tag{4.47}$$

with ν is fixed. In the case $\eta \geq \nu$, we can see that very rapid damping of the magnetic field compared to the velocity field when $t \to \infty$. Therefore we can assume for some $r > r_s$

$$\frac{\eta}{r^3} \to \frac{1}{\alpha r}, \tag{4.48}$$

and hence the monotonic decay rate is given by

$$\alpha \simeq \left(\frac{\nu}{\eta}\right)^{1/2}, \tag{4.49}$$

with the visco-resistive length scale $r_s = (\eta\nu)^{1/4}$. However, the computational results do not match with the scaling argument of the (4.49). As an example, when $\eta > \nu$, Figure 4.29 shows that the pattern of energy dissipation for various values of η when $\eta \geq \nu$ with $\nu = 0.003$ is fixed . These computational results show the same magnetic and kinetic energy monotonic decay rates for a variety of resistivities

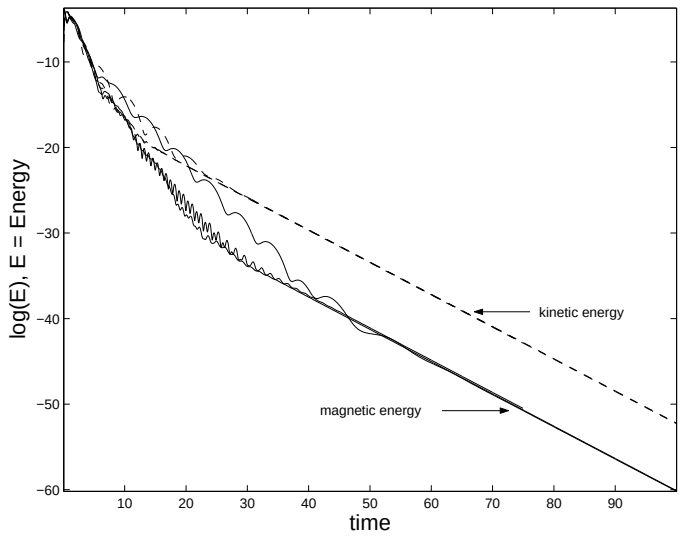

Figure 4.29: The decay of the magnetic and kinetic energies for the non-topological mode for $\eta \geq \nu$ with fixed $\nu = 0.003$. The values, $\eta = 0.003$, 0.005, 0.01 give the same monotonic energy dissipation rates.

$\eta = 0.003$, 0.005, 0.01. Therefore we can argue that when $\eta \geq \nu$, non-oscillatory decay of the magnetic and kinetic energy depend only on the viscosity, but not on the resistivity.

In fact the above results imply the monotonic decay rate $\alpha \sim 1$ with ν is fixed, which is given by applying resistive length scale $r_s \sim \eta^{1/2}$ into (4.48). Therefore, to explain the case $\eta \geq \nu$, we need resistive length scale $r_s \sim \eta^{1/2}$. In summary we can argue, when $\eta \geq \nu$ the required length scale is $r_s \sim \eta^{1/2}$ and when $\nu >> \eta$ the visco-resistive length scale $r_s \sim (\eta\nu)^{1/4}$ applies. The ranges of the length scales for the solar plasmas are given by $\eta^{1/2} < (\eta\nu)^{1/4} < \nu^{1/2}$.

4.7 Summary

We have demonstrated that magnetic and kinetic energy in the X-point collapse problem can be rapidly dissipated by both resistivity and viscosity. In particular the

presence of viscosity can dramatically affect the evolution of X-point disturbances. In the case of non-reconnective disturbances, our results imply that viscosity, in common with resistivity, can provide fast oscillatory dissipation of the excess magnetic energy. In the case of reconnective disturbances, however, the magnitude of the viscous term does become critical. For $\eta \leq \nu$, oscillatory reconnection is suppressed and we have seen that the global magnetic energy decays at a much slower rate than the kinetic energy. However, in the initial stage, a significant fraction of the disturbance field energy is rapidly damped by viscosity. For $\eta > \nu$ fast oscillatory reconnection is regained. Results for both non-topological and topological disturbances show that the maximum energy dissipation occurs when the viscous and resistive coefficients are closely matched.

The solutions of §4.6.2 reviewed here exhibit viscous dissipation rates which scale independently of any positive power of ν ($W_\nu \sim \nu^0$) making them formally "fast". By this we mean that the magnetic field at the edge of the current sheet scales as a negative power of ν. Thus a significant fraction (more than half) of the initial disturbance energy will be transferred to the fluid motion and dissipated by viscosity within a few Alfvén times. For $\nu > 0$ and $\eta = 0$, viscous dissipation operates on the length scale $\nu^{1/2}$, while for $\eta > 0$ and $\nu = 0$, the relevant scale is $\eta^{1/2}$. For $\eta > 0$ and $\nu > 0$, the behaviour can be understood in terms of a visco-resistive length scale $r_s = (\eta\nu)^{1/4}$.

We have also detailed a new model that accounts for the magnetic and kinetic energy separation prior to the monotonic decay. In fact, our results suggest that the behaviour of the system with viscosity included becomes significant when $\nu \geq \eta$. The condition $\nu \geq \eta$ implies that, for comparable magnitudes of the $\mathbf{B}$ and $\mathbf{v}$ fields, the viscous force can dominate the Lorentz force at the smallest length scales, and thus prevent equipartition.

Chapter 5

Hall effects on dynamic magnetic reconnection at an X-type neutral point

5.1 Introduction

In 1879, Edwin H. Hall discovered that when he placed a conducting strip carrying a current in a magnetic field, a potential difference was produced across the strip-transverse to the current and magnetic field directions (Figure 5.1). This potential difference is called the Hall voltage.

In the context of astrophysical MHD, it has recently become clear that Hall current effects may lead to important physical manifestations. The Hall effect is expected to become significant when the dimensionless Hall coefficient d_i (see equation (2.29) in §2.2.4) satisfies

$$d_i > \eta \tag{5.1}$$

where η is the inverse Lundquist number (the dimensionless resistivity) for the plasma. For a typical coronal plasma (i.e. a weakly collisional fluid) this criterion

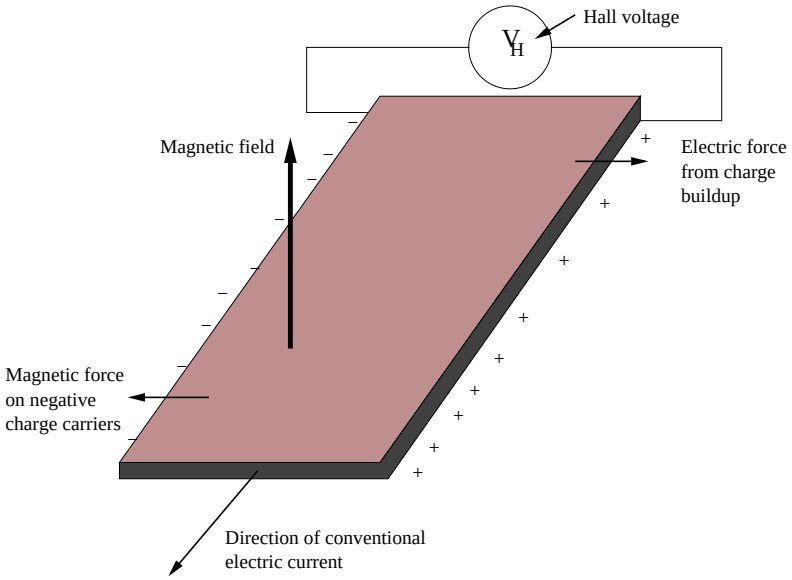

Figure 5.1: If an electric current flows through a conductor in a magnetic field, the magnetic field exerts a transverse force on the moving charge carriers which tends to push them to one side of the conductor.

is easily satisfied since $d_i \simeq 10^{-7}$ and $\eta \simeq 10^{-14}$ (Chapter 2). As a result, in recent years it has become clear that Hall effects may be important for magnetic merging simulations (Birn & Hesse, 2001; Craig & Watson, 2003; Craig et al., 2003).

Recent studies suggest that Hall currents can significantly influence the merging process, by altering the geometry of the reconnecting fields and changing the speed of the reconnection (e.g. Bhattacharjee et al., 1999; Birn et al., 2001; Dorelli, 2003). Unlike classical 'resistive' reconnection, which can be developed in terms of planar two dimensional models, Hall current merging is essentially three dimensional since axial field components are naturally induced by planar reconnecting fields. To what extent the emergence of transient axial fields influences the dynamics of the merging process is not yet fully understood. What can be demonstrated is that Hall currents can either speed up or slow down the merging rate depending on the symmetries of the merging fields (Craig & Watson, 2005).

In Chapter 3, magnetic merging models were discussed using the traditional resistive Ohm's law. In particular, early studies of X-point collapse in line-tied geometries neglected Hall current and electron inertial effects (Craig & McClymont, 1991; Hassam 1992; Craig & Watson, 1992). Later work incorporated the presence of axial field components (McClymont & Craig, 1996), plasma inertial effects (McClements et al., 2004) and viscous dissipation (Craig, Litvinenko & Senanayake, 2005), but the Hall current effect was neglected.

As pointed out previously, the collisional approximation almost certainly breaks down for the small length scale features predicted by low resistivity merging solutions. A recent development to remedy this situation has been to employ a more generalized version of Ohm's law, with specific attention being paid to the Hall term (Craig & Watson, 2003). This version of Ohm's law includes collisionless quantities such as finite electron inertia, electron pressure gradient and the Hall current. A key finding, for example, is that a finite Hall coefficient can increase the reconnection rate, by increments which are independent of the size scale of system (Shay et al 1999, Cassak et al 2006).

In this chapter we investigate the reconnection rate of a disturbed X-type neutral point configuration in the presence of Hall currents. The results will be obtained numerically, but their general validity can be checked by comparison with previous work (e.g. Craig & Watson, 1992). Some of the work in this chapter was published in Astronomy and Astrophysics (Senanayake & Craig, 2006). Here we present a more detailed exposition and include more comprehensive numerical results.

In §5.2, we formulate the X-point reconnection problem in a way which highlights the modifications introduced by the Hall current. In §5.3, we present a computational study in which scaling laws are derived for the decay rate and oscillation frequency of X-point disturbances. In particular, we use our results to find out how the reconnection rate in Hall MHD is related to the system size. The claim that

the Hall reconnection rate, measured in units of the Alfvén time, must be a universal constant which is independent of the system size, has recently been questioned (Bhattacharjee et al., 2005). Hence it is important to know whether the reconnection rate depends on the system size. We also study how Hall currents influence the initial implosive collapse that acts as a precursor for the oscillatory decay.

5.2 MHD with a generalized Ohm's law

We work with the compressible pressureless MHD equations, non-dimensionalized with respect to the reference coronal values given in Chapter 2:

$$B_c = 10^2\text{G}, \qquad l_c = 10^{9.5}\text{cm}$$
$$n_c = 10^9\text{cm}^{-3}, \quad v_A = 10^9\text{cm s}^{-1}.$$

Time is now measured in units of the Alfvén time $\tau_A = l_c/v_A$, which is typically a few seconds in coronal applications. In this formulation, the plasma resistivity is an inverse Lundquist number $\eta << 1$.

We assume that the behavior of such a plasma with velocity $\mathbf{v}$, pressure p, density ρ and magnetic field $\mathbf{B}$ is governed by fluid equations of MHD, namely the continuity equation (2.25),

$$\frac{\partial \rho}{\partial t} + \nabla \cdot (\rho \mathbf{v}) = 0, \tag{5.2}$$

the inviscid momentum equation (2.26)

$$\rho \left(\frac{\partial \mathbf{v}}{\partial t} + (\mathbf{v} \cdot \nabla)\mathbf{v} \right) = -\nabla p + \mathbf{J} \times \mathbf{B}, \tag{5.3}$$

where $\mathbf{J} = \nabla \times \mathbf{B}$ is the current density, and the generalized induction equation (2.27) with $d_e = 0$;

$$\frac{\partial \mathbf{B}}{\partial t} = \nabla \times (\mathbf{v} \times \mathbf{B}) - \eta \nabla \times \mathbf{J} - d_i \nabla \times (\mathbf{J} \times \mathbf{B}) \, . \tag{5.4}$$

We refer to the last two terms on the right hand side as the resistive and Hall terms respectively. The dimensionless coronal values are: $\eta = 10^{-14.5}$ is the plasma

resistivity based on the collisional conductivity, $d_i = 10^{-6.5}$ is ion skin depth (see §2.2.4). Although we neglect the electron inertial effect and viscous effect, these contributions have been explored in recent X-point studied by McClements et al. (2004) and Craig, Litvinenko & Senanayake (2005).

In common with traditional non-Hall current MHD models, the resistivity η provides the only avenue for extracting energy from the magnetic field. The Hall current influences the advection of the magnetic field which is tied mainly to the electron fluid as opposed to the mass-averaged electron-proton gas of conventional MHD. We note that Hall current merging is expected to be important when the reconnection length scale r_s satisfies $d_e << r_s < d_i$ (Fitzpatrick, 2003). Our aim therefore is to study the relative importance of the Hall and resistive terms, and to examine how the geometry of the merging affects both the reconnection and Ohmic dissipation rates.

5.2.1 Linearized equation

In general the continuity, momentum and induction equations need to be supplemented by an equation of state and the divergence constraint $\nabla \cdot \mathbf{B} = 0$. However, since we deal with small displacements in a cold, two and a half dimensional two-species (electron and proton) plasma with $\partial_z = 0$, we can obtain a complete description by linearizing (5.3) and (5.4), and using a flux function representation for the magnetic field,

$$\mathbf{B}(x, y, t) = \nabla\psi \times \hat{\mathbf{z}} + Z\hat{\mathbf{z}}. \tag{5.5}$$

It is convenient to split the velocity and magnetic fields into planar and axial components, namely

$$\mathbf{v}(x, y, t) = (\mathbf{V}, W), \qquad \mathbf{B}(x, y, t) = (\partial_y\psi, -\partial_x\psi,\, Z), \tag{5.6}$$

where $\mathbf{V} \cdot \hat{\mathbf{z}} = 0$. We let

$$\psi(x, y, t) \rightarrow \psi_E(x, y) + \psi(x, y, t), \tag{5.7}$$

and linearize about the planar, background field $\mathbf{B}_E = (\partial_y \psi_E, -\partial_x \psi_E)$. Neglecting the plasma pressure, the momentum equation (5.3) becomes

$$\frac{\partial \mathbf{v}}{\partial t} = \mathbf{J} \times \mathbf{B}_E. \tag{5.8}$$

The planar and the $\hat{\mathbf{z}}$ components of equation (5.8) are

$$\frac{\partial \mathbf{V}}{\partial t} = -\nabla^2 \psi \, \nabla \psi_E. \tag{5.9}$$

and

$$\frac{\partial W}{\partial t} = (\mathbf{B}_E \cdot \nabla) \, Z, \tag{5.10}$$

respectively. Uncurling the $\hat{\mathbf{z}}$ component of (5.4), we find the planar field components reduce to

$$\frac{\partial \psi}{\partial t} + \mathbf{V} \cdot \nabla \psi_E = \eta \nabla^2 \psi - d_i (\mathbf{B}_E \cdot \nabla) \, Z. \tag{5.11}$$

The axial field component is given by

$$\frac{\partial Z}{\partial t} = (\mathbf{B}_E \cdot \nabla) W + \eta \nabla^2 Z + d_i (\mathbf{B}_E \cdot \nabla) \, \nabla^2 \psi \, . \tag{5.12}$$

The system (5.9) to (5.12) provides our basic model for describing X-point, Hall current reconnection.

5.2.2 Preliminary comments

In the absence of the Hall term ($d_i = 0$), it is possible to consider a purely planar problem with $Z = W = 0$. In this case the current density, namely

$$\mathbf{J} = (0, \, 0, \, -\nabla^2 \psi) \, , \tag{5.13}$$

comprises only an axial "reconnection" current. In the presence of the Hall term ($d_i > 0$), an axial magnetic field is generated (see equation 5.12) by Hall current. It follows that the current density

$$\mathbf{J} = (Z_y, -Z_x, -\nabla^2\psi) \ , \tag{5.14}$$

now develops planar components in addition to the axial current component. Merging is now completely defined by the planar equations (5.9) and (5.11). For d_i finite however, gradients of the reconnection current, in the direction of the equilibrium field, will drive a growth in the Z-field (5.12) which, via equation (5.10), will generate an axial velocity W. Growth in the axial fields can be expected to feed back on the flow field and slow the merging process. In general both the reconnection rate,

$$\frac{\partial\psi}{\partial t} = \eta|\mathbf{J}_0| \tag{5.15}$$

where $\mathbf{J}_0$ is the current density at the merging point, and the Ohmic dissipation rate

$$W_\eta = \eta \int J^2 dV = \eta \int (Z_x^2 + Z_y^2 + (\nabla^2\psi)^2) dV, \tag{5.16}$$

will be affected by the growth in Z. We can estimate the conditions under which the Hall term becomes important by comparing

$$\eta\nabla^2\psi \sim d_i(\mathbf{B}_E \cdot \nabla)Z$$

in (5.11). Assuming the Z-field is induced from (5.12) by the Hall current, we require

$$\frac{\partial Z}{\partial t} \sim d_i(\mathbf{B}_E \cdot \nabla)\nabla^2\psi$$

where $\mathbf{B}_E = (x, -y, 0)$ (see (5.19)). Eliminating Z from above two forms, we have the scaling quantity

$$\kappa = \tau\frac{{d_i}^2}{\eta} \geq 1 \tag{5.17}$$

where τ is a typical merging timescale. This condition differs considerably from the elementary expectation (5.1). Even so, for τ of order unity (Alfvénic merging), this

condition is easily met in the case $\eta \simeq 10^{-14.5}, d_i \simeq 10^{-6.5}$. Hence, we have good reasons for including Hall currents in the reconnection models based on collisional conductivities.

5.3 X-type neutral points with Hall current

We now investigate the X-point reconnection dynamics in the presence of Hall current effects. In §5.3.1, the three-dimensional magnetic field intensity is derived by working with the planar flux function ψ and axial component of Z. The numerical problem for a given perturbation field ψ in Cartesian coordinates, is formulated mathematically in §5.3.2. We begin by examining the decay rate and oscillation frequency for various values of d_i taking fixed values of resistivity η in §5.3.3. The size dependence of the Hall MHD reconnection rate is considered in §5.3.4. The resistive and Hall current contributions to the reconnection rate are investigated in §5.3.5. We also examine whether the Ohmic dissipation rate increases with d_i. The structure of the reconnection current is investigated in §5.3.7.

5.3.1 Initial and boundary conditions

As in Chapter 4, we imagine an X-type neutral point with constant resistivity in a uniform density background plasma ρ_0. Although the early work on the X-point problem with the pure resistivity was described analytically by invoking a cylindrical mode description, we find it more convenient to employ a rectangular boundary when evaluating the directional derivatives associated with the Hall term $d_i(\mathbf{B}_E \cdot \nabla)$.

The equilibrium background magnetic field is taken as

$$\psi_E = xy, \qquad -1 \leq x, y \leq 1 \tag{5.18}$$

corresponding to

$$\mathbf{B}_E = (x, -y, 0) \tag{5.19}$$

in rectangular Cartesian coordinates. The field is immersed in an uniform density plasma and anchored by line-tying to rigid outer walls, where $\mathbf{v} = 0$ and the potential ψ is fixed. The setting boundary condition for Z is very important because it will effect the stability of numerical code for large values of d_i. We used Newton forward and backward difference formulas to achieve numerical accuracy close to the outer boundary. For an example, the Z field at the boundary line $x = 1$ is given by

$$Z(1, y) = 2Z(1 - \Delta x, y) - Z(1 - 2\Delta x, y), \quad -1 \leq y \leq 1$$

where Δx is grid spacing in the range $-1 \leq x \leq 1$.

Initially the equilibrium field is subject to a spectrum of finite-amplitude disturbances. Here and in what follows we assume initial conditions in which only the planar field is disturbed:

$$\mathbf{V}(x, y, 0) = 0 \quad \text{and} \quad Z(x, y, 0) = 0. \tag{5.20}$$

The initial flux function with perturbation field is taken as

$$\psi(x, y, 0) = xy + A(1 - x^2)(1 - y^2) \tag{5.21}$$

as shown in Figure 5.2 where $A \simeq 0.1$. Note that the background field defined by $\psi_E = xy$ satisfies the current-free condition $\nabla^2 \psi_E = 0$. The magnetic disturbance field raises the energy of the X-point and changes the intrinsic topology. The plasma responds by accelerating inwards due to the Lorentz force. To regain the equilibrium by resistive relaxation, excess flux in the top-left and lower-right lobes has to be transferred by reconnection through the neutral point. In fact the plasma tends to overshoot on the initial implosion, transferring too much flux to the North-South lobes. This inertial overshoot sets up the conditions required for "oscillatory" reconnection.

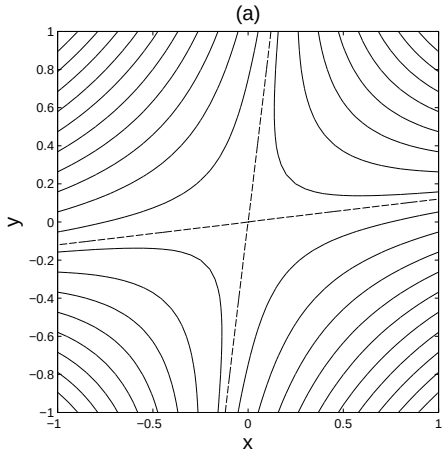

Figure 5.2: Field lines of perturbed X-point configuration with potential field $\psi = xy + 0.1(1-x^2)(1-y^2)$.

5.3.2 Numerical solution with Hall term

Substituting (5.19) into equations (5.9), (5.10), (5.11) and (5.12) gives the system

$$(U, V, W)_t = (-y\nabla^2\psi, -x\nabla^2\psi, -yZ_y + xZ_x), \tag{5.22}$$

$$\psi_t = -xv - yu + \eta\nabla^2\psi - d_i\mathcal{D}Z, \tag{5.23}$$

$$Z_t = \mathcal{D}W + \eta\nabla^2 Z + d_i\mathcal{D}\nabla^2\psi, \tag{5.24}$$

where $\mathbf{V} = (U, V)$ is the planar component, W the axial component of the velocity field and the operator $\mathcal{D} = \mathbf{B}_E \cdot \nabla = x\partial_x - y\partial_y$. Taking the second derivative of (5.23) and (5.24) gives the system

$$\psi_{tt} = (x^2 + y^2)\nabla^2\psi + \eta\nabla^2\psi_t - d_i\mathcal{D}Z_t, \tag{5.25}$$

$$Z_{tt} = \eta\nabla^2 Z_t + \mathcal{D}\left(\mathcal{D}Z + d_i\nabla^2\psi_t\right), \tag{5.26}$$

on eliminating the velocity field. Numerical solutions are obtained in two ways: either by an explicit finite difference replacement of the system (5.22)-(5.24); or by semi-implicit treatment of (5.25)-(5.26). Both systems completely determine the

dynamic Hall current reconnection problem at X-type neutral points based on a generalized Ohm's law.

First, we apply the explicit code for the finite difference solution of system (5.22)-(5.24). This method is simple but, needs a small time step for sufficient stability and accuracy. The computational grid is uniform in both directions. In order to resolve the reconnection region, we choose a minimum of eight grid points in the region of localized current. Second, we apply the simulation code for the semi-implicit treatment of (5.25)-(5.26), as described in Appendix A. Our results in Chapter 5 are based on the system (5.22)-(5.24).

5.3.3 Decay rate and oscillation frequency

Recall that, as discussed in Chapter 4, in the case $d_i = 0$, the reconnection problem can be reduced to the analytic X-point solution of Craig & McClymont (1991; 1993) and Hassam (1992). Figures 5.3a and b provide a side by side comparison of the pure resistive solution, against the Hall model. It is clear that the Hall solution also comprises three distinct phases in the time evolution of ψ. In the pure resistive case, there is an initial implosion in which the disturbance localizes into a quasi-cylindrical current spike of amplitude $J_0 \sim \eta^{-1}$ at the origin. This is followed by a phase of oscillatory reconnection, dominated by the fundamental eigenmode,

$$\lambda = \alpha + i\omega, \quad \alpha \simeq -\frac{\omega^2}{2}, \quad \omega = \frac{\pi}{|\ln \eta|}. \tag{5.27}$$

Finally, after the oscillations have died down, a self-similar mode emerges associated with a very slow monotonic decay. These phases are summarized in Figure 5.3a for the disturbance field (5.21).

As discussed in Chapter 4, independent computations (Craig & Watson 1992; Craig, Litvinenko & Senanayake, 2005) confirm that the eigenmode description remains an excellent approximation when the circular boundary is replaced by a highly conducting square wall.

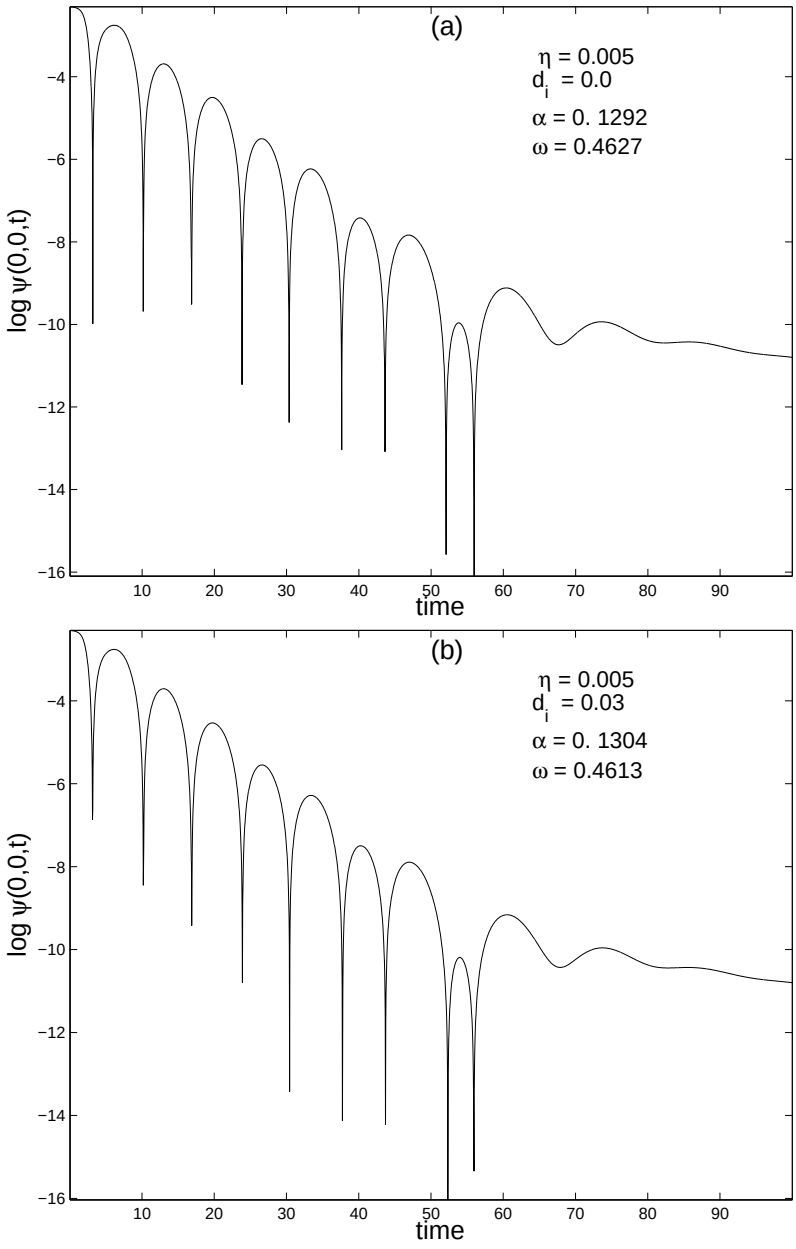

Figure 5.3: (**a**) Decay of the flux function ψ versus time (measure in Alfvén times) when $d_i = 0$, $\eta = 0.005$. (**b**) Decay of ψ when $d_i = 0.03$, $\eta = 0.005$. After a certain number of Alfvén times, both ψ functions cease to oscillate.

In order to determine the decay rate (α) and oscillation frequency (ω) associated with the Hall effect, we compute the oscillation of flux function at the neutral point. Our first observation based on Figure 5.3b, is that the decay of the disturbance field (5.21) when $d_i \neq 0$, maintains the three distinct phases of Figure 5.3a. We begin by examining the decay rate α and oscillation frequency ω for various values of d_i, taking a fixed value of resistivity η. Figure 5.4a, in which $\eta = 0.01$, suggests that there is a linear relation between

$$\ln(\alpha - \alpha_0) \quad \text{and} \quad \ln\left(\frac{d_i}{\eta^{1/4}}\right)$$

where α_0 and α denote decay rates in the case $d_i = 0$ and $d_i > 0$ respectively. The gradient of the line is $\simeq 2$. We also plot the same quantities as in Figure 5.4a, but for various values of η namely $\eta = 0.005$ and $\eta = 0.001$, from which we see the same linear relation emerge. Since Figure 5.4b reinforces this relationship for $\eta = 0.01, 0.005$ and 0.001, we obtain a scaling law for the decay rate

$$\alpha = a_1 \left(\frac{d_i}{\eta^{1/4}}\right)^{r_1} + \alpha_0 \ , \tag{5.28}$$

with $a_1 \simeq 0.1$ and $r_1 \simeq 2$. This relationship holds for $0 \leq \kappa \leq 2$, and confirms that increases in the Hall coefficient enhance the decay rate of the plasma energy ($\kappa = d_i^2/\eta$).

A similar relationship holds for ω. Figures 5.5a and b confirm that oscillation frequency

$$\omega = \omega_0 - a_1 \left(\frac{d_i}{\eta^{1/4}}\right)^{r_1} \ , \tag{5.29}$$

decreases as d_i increases. Note that a_1 and r_1 are all independent of η.

The equations (5.28) and (5.29) determine how the decay rate α and oscillation frequency ω scale with d_i for the resistive range $0.001 < \eta < 0.01$. Do these scalings hold for all other resistivities out of the range $0.001 < \eta < 0.01$? Note that by introducing the normalized decay rate $\Delta\alpha/\alpha_0$ where $\Delta\alpha = \alpha - \alpha_0$, we can also

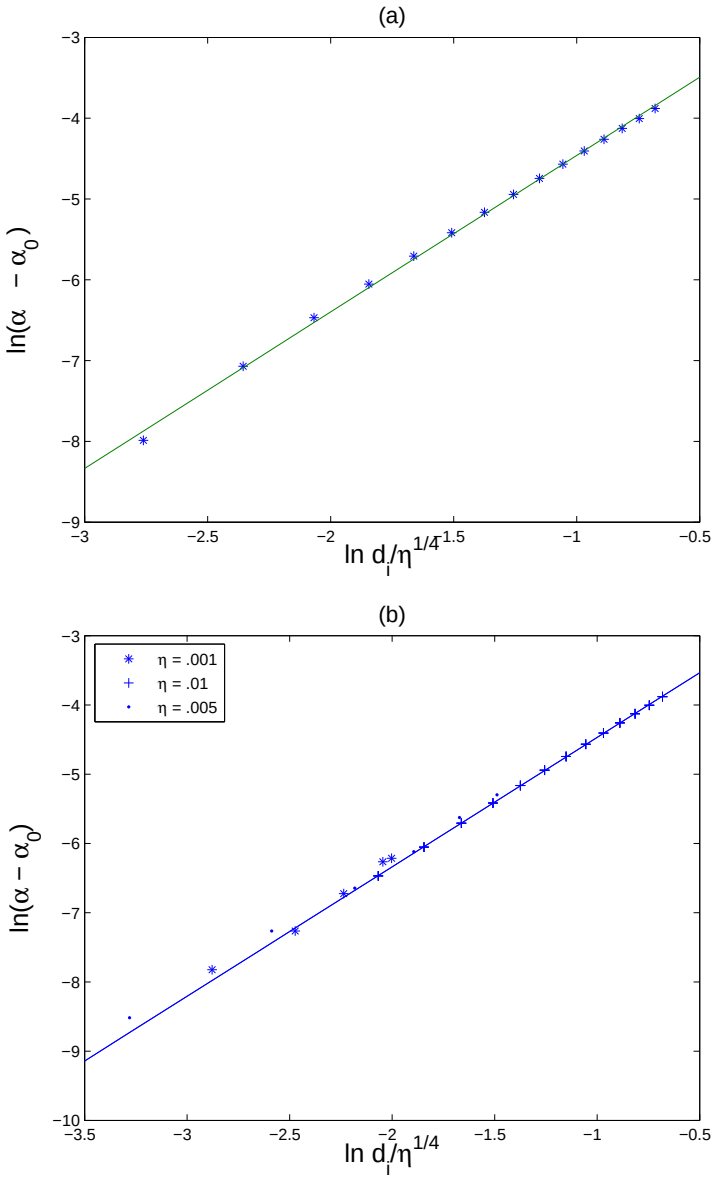

Figure 5.4: Scaling of the decay rate, α, as function of d_i in oscillatory phase for the parameters (**a**) $\eta = 0.01$ with range $0.01 \leq \kappa \leq 2.56$, (**b**) $\eta = 0.01,\ 0.005,\ 0.001$ with range $0.01 \leq \kappa \leq 2.56$, where $\kappa = d_i^2/\eta$. The solid lines are fit to $y = 1.87\,x\ - 2.30$.

obtain a good fit to the form

$$\frac{\Delta\alpha}{\alpha_0} = A\left(\frac{d_i}{\eta^{1/2}}\right)^2 \tag{5.30}$$

with $A \simeq 0.05$ as shown in Figure 5.6. This is broadly consistent with (5.28) over the narrow range of resistivities considered. However, the ratio $d_i/\eta^{1/2}$ in (5.30) is physically more significant parameter than $d_i/\eta^{1/4}$ (Craig & Watson, 2003), as we have noted in equation (5.17). Accordingly, we have more confidence in extrapolating the normalized scaling (5.30) to lower resistivity values rather than formula (5.28).

The above numerical results demonstrate that the decay rate can be increased by inclusion of the Hall effects. Also it is clear that these scalings break the simple analytic relationship between the oscillation frequency and the decay rate found in the resistive problem (5.27). One possible explanation—and one that holds for the related problem of steady state incompressible merging (Dorelli, 2003; Craig & Watson, 2005)—is that the Hall current speeds up the merging rate by enhancing the localization of the current density. This would indeed slow down the oscillation frequency since, by the argument leading to (4.21), the time taken for an Alfvén wave to travel from the outer wall to the diffusion region is increased because r_s is now smaller than its resistive value (see (4.25)). The validity of this argument depends however, on the detailed morphology of the current density, and this can change dramatically when the Hall term is sufficiently large, as we detail below. A further difficulty is that stronger current densities for $d_i > 0$ will increase the tendency for current driven instabilities, especially since ion-acoustic turbulence is likely to be excited for purely collisional merging (Litvinenko & Craig, 2000).

5.3.4 Dependence on the system size

We know that solar flares occur over a variety of length scales (see Chapter 1). It is important to ask therefore to what extent the energy release rate depends on the

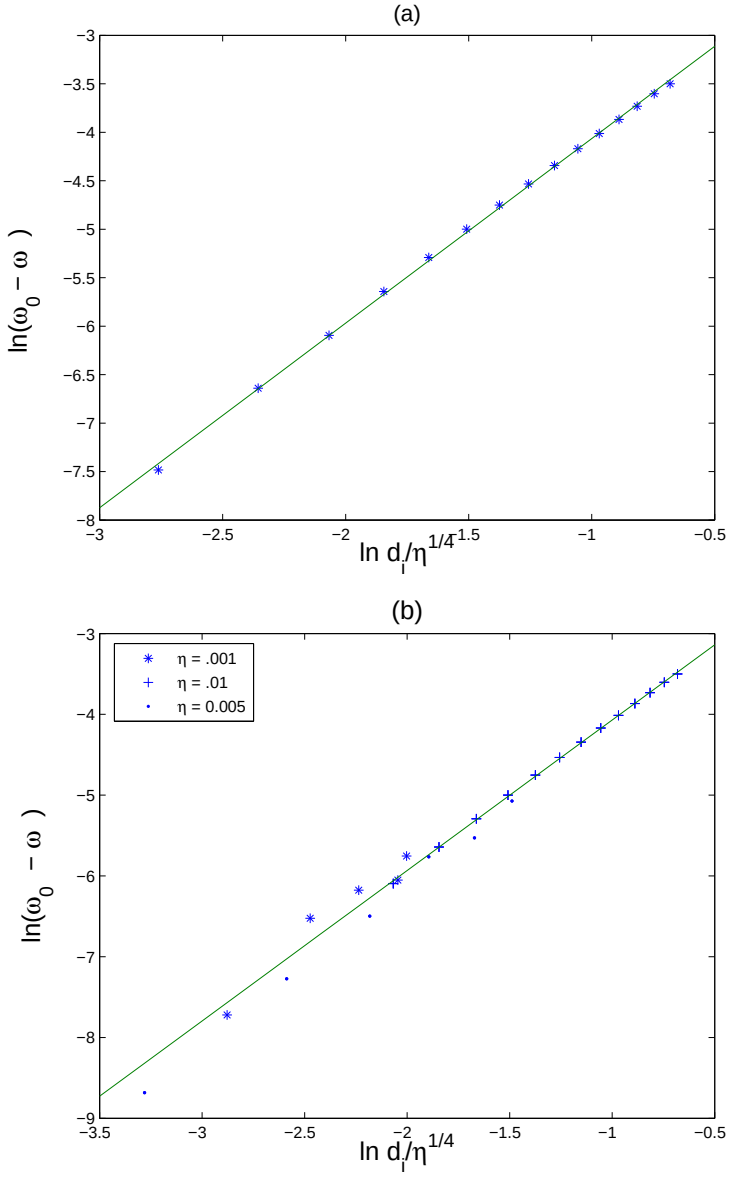

Figure 5.5: Scaling of oscillation frequency, ω, as the function of d_i in oscillatory phase for the parameters (**a**) $\eta = 0.01$ with range $0.01 \leq \kappa \leq 2.56$, (**b**) $\eta = 0.01,\ 0.005,\ 0.001$ with range $0.01 \leq \kappa \leq 2.56$, where $\kappa = d_i^2/\eta$. The solid lines are fit to $y = 1.87\,x\ - 4.5$.

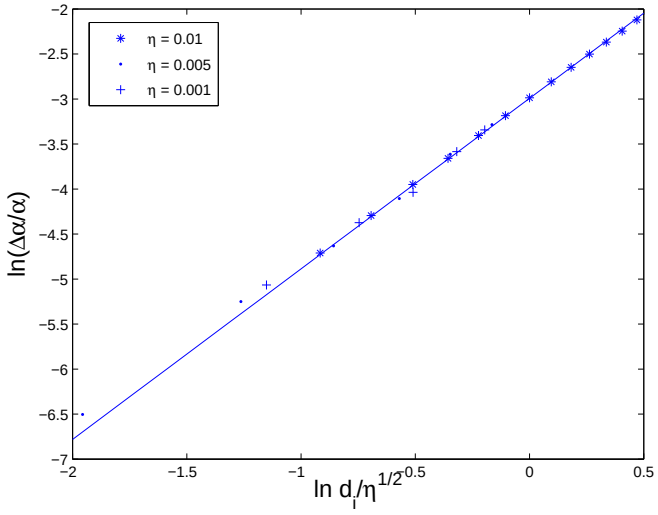

Figure 5.6: The plot $\ln(\Delta\alpha/\alpha_0)$ against $\ln(d_i/\eta^{1/2})$ in oscillatory phase for the parameters $\eta = 0.01,\ 0.005,\ 0.001$ with range $0.01 \leq \kappa \leq 2.56$, where $\kappa = d_i^2/\eta$. The solid line is fit to $y = 1.89x - 2.99$.

size of the system. Because the dimensionless parameters

$$d_i = \frac{c}{l_c\omega_{pi}}, \quad \eta = \frac{c^2}{4\pi v_A l_c \sigma}$$

are functions of the length scale l_c, equation (5.30) implies the scaling

$$\frac{\Delta\alpha}{\alpha_0} \sim \frac{1}{l_c}. \tag{5.31}$$

This means that the increase in the energy decay rate due to the Hall term will reduce as the system size increases. It is not, at least for the X-point system, a universal constant as suggest by Shay et al., (1999). Therefore, the reconnection time at line-tied X-points will be relatively longer for larger systems.

Our reconnection simulation gives length scale $r_s \simeq \eta^{1/2}$. Some other models give different length scales so $r_s \simeq \eta^{1/2}$ cannot be universal. We can however generalize equation (5.30), by taking

$$\frac{\Delta\alpha}{\alpha_0} \sim \left(\frac{d_i}{r_s}\right)^2 \tag{5.32}$$

and asking what scaling for $r_s(\eta)$ would allow a result independent of the system size. Only a very small length scale (with strong collapse), namely $r_s \sim \eta$, would give us a normalized scaling $\Delta\alpha/\alpha_0$ independent of l_c. But there is no evidence for this type of collapse, either in the present simulations , or in independent computations of magnetic merging in other geometries. The most extreme resistive scaling is $r_s \sim \eta^{2/3}$ for the coalescence instability (Biskamp & Welter, 1980; Rickard & Craig, 1993; Knoll & Chacon, 2006), which leads to the size dependence $\Delta\alpha/\alpha_0 \sim l_c^{-2/3}$. Hence, our simulations provide no evidence for idea that the Hall reconnection rate is a universal constant that is independent of the system size.

5.3.5 The initial X-point implosion

In chapter 3 we mentioned that both the reconnection and Ohmic dissipation rates are largely unaffected by resistivity in the purely collisional solution. Specifically, the cylindrical solution (Craig & Watson, 1992) implies that the current density ($\mathbf{J} = -\nabla^2\psi\,\hat{\mathbf{z}}$) at the null, namely

$$J_0 \simeq \frac{1}{\eta},$$

occupies a small circular area $A_s \simeq r_s^2 \simeq \eta$, during the initial implosive phase. These relations suggest that for the initial implosive phase, both the reconnection rate and the Ohmic dissipation rate should be independent of η.

When Hall currents are introduced, the current density is no longer purely axial because planar components are present due to the induction of the Z-field. The development of a strong separator field ($Z(x, y, t)$) is clearly manifested in the planar components of the current density as given by (5.14).

Of course , it is the transport of fresh flux into the reconnection zone that controls the reconnection rate. The planar components which are present due to the induction of the Z-field cannot directly influence the reconnection rate since flux

transfer at the neutral point depends only on the axial current $\nabla^2\psi\,\hat{\mathbf{z}}$. The three plots of Figure 5.7 show a computed reconnection rate $\psi_t = \eta J_0$ during the first ten Alfvén times based on the numerical solution of equations (5.22)-(5.24) for the resistivities $\eta = 0.01$, 0.003 and 0.001. The plots confirm that the peak reconnection rate, (ηJ_0), slightly reduces before enhancing with d_i, achieving a minimum reconnection rate at $d_i = d_i^*$ say. Fitzpatrick (2004) observed broadly similar behaviour in computations of the Taylor problem, but in his case the reconnection rate was independent of d_i, for $d_i < d_i^*$ with scaling $d_i^* \sim \eta^{1/3}$. Also, work by Craig & Watson (2002) and Craig, Heerikhuisen & Watson (2003) show that the planar field is largely unaffected by the Hall term when $d_i << \eta$ and hence the reconnection rate should also be unchanged.

In Figure 5.8a, we plot the logarithm of the reconnection rate against $\log(d_i)$, for three values of η. A salient feature is the systematic shift to the right of the minimum rate as η increases. However, since Figure 5.8b indicates that this shift can be eliminated if the reconnection rate is plotted against $\log(d_i/\eta^{1/3})$, we obtain the tentative result that d_i^* may scale as $\eta^{1/3}$. The reconnection rate then increases for $d_i > d_i^*$ where there is an increasing tendency for the reconnection rate to oscillate as shown in Figures 5.7b & c. The reason of the oscillatory behaviour is that axial current and induce Hall current alternate each other. The development of oscillatory components in Hall current solutions has been noted in previous studies (e.g. Watson & Porcelli, 2004) and may be linked to the development of whistler wave modes in the solution for large $d_i >> \sqrt{\eta}$ (see §5.3.7 below).

Possibly, due to the presence of these oscillatory wave modes, our numerical scheme becomes less reliable for $d_i >> \eta^{1/2}$. However, in common with Fitzpatrick (2004), who invokes an empirical "hyper resistivity" (which may arises as a consequence of the turbulence or magnetic field line braiding) to control the whistler modes, the present results appear consistent with an increase in the reconnection

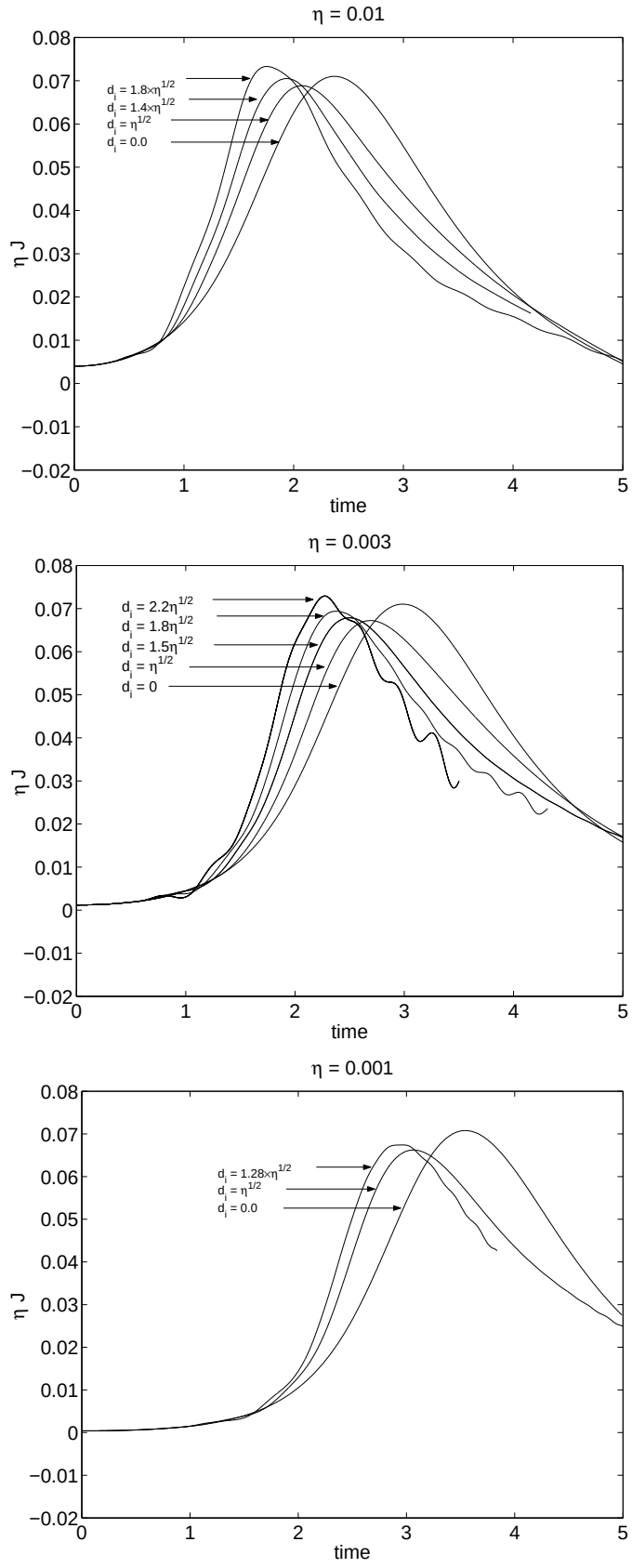

Figure 5.7: Three plots show the reconnection rate, ηJ, versus time for various values of d_i when $\eta = 0.01,\ 0.003$ and 0.001. The oscillation in the axial current (J) at the X-point is due to Hall effects (whistler waves) for large values of d_i.

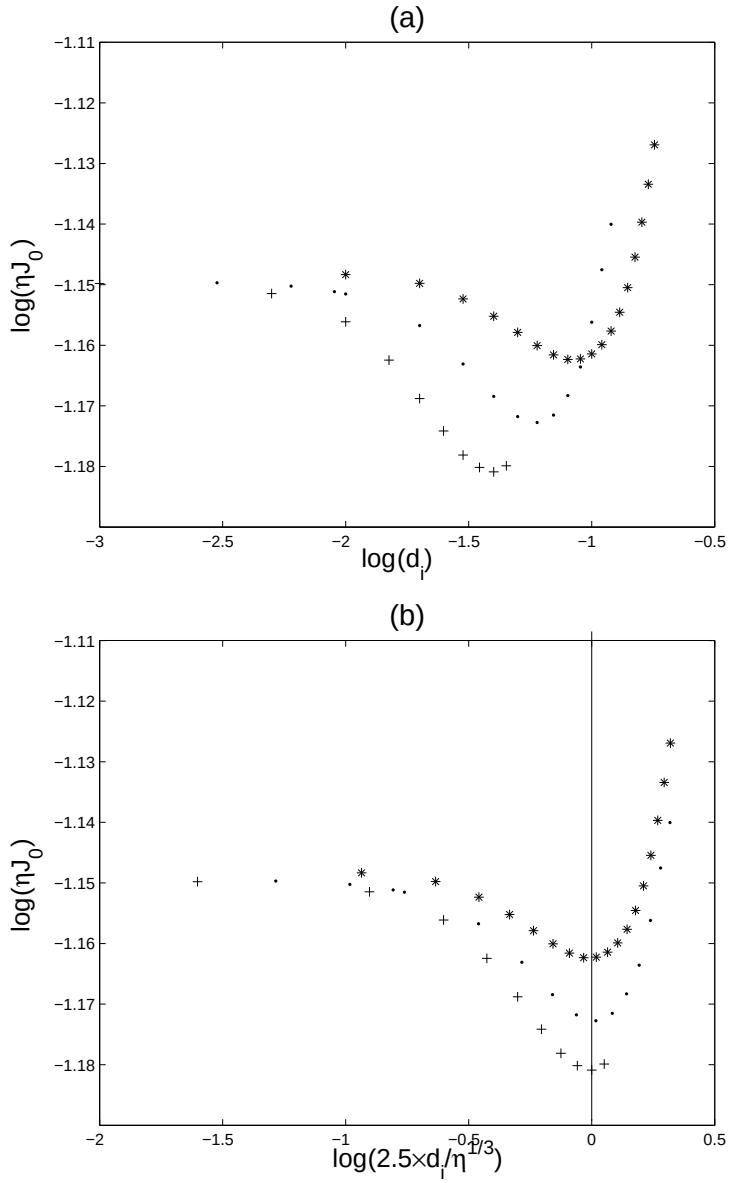

Figure 5.8: (**a**) Scaling of the peak magnetic reconnection rate, ηJ_0, with ion skin depth, d_i, in the linear regime. (**b**) Scaling of the peak magnetic reconnection rate, $\eta J_{\max}$, with $2.5 \times d_i/\eta^{1/3}$. The '$\star$' corresponds to $\eta = 0.01$. The '$\cdot$' corresponds to $\eta = 0.003$. The '$+$' corresponds to $\eta = 0.001$.

rate for $d_i^* \geq \eta^{1/3}$.

5.3.6 Ohmic dissipation rate

In Figure 4.8b of Chapter 4, we showed computations of W_η during the initial X-point evolution for resistive computation. Although the maximum dissipation rates vary with time, the peak rates are in agreement with theory, unaffected by decreases in resistivity (Craig & McClymont, 1991, 1993).

The Ohmic dissipation rate due to the Hall-induced separator field over the domain can be computed using (5.16)

$$W_\eta = \eta \int J^2 dV = \eta \int (Z_x^2 + Z_y^2 + (-\nabla^2 \psi)^2) dV.$$

Figures 5.9a and c represent the axial current ($|\nabla^2 \psi|$) generated by the planar merging field and Figures 5.9b and d represent the planar current ($|\sqrt{Z_x^2 + Z_y^2}|$) generated by the Hall effect. All figures give the current densities for fixed $\eta = 0.005$, but various values of κ such as $\kappa = 0.2$ and 4.0 where $\kappa = d_i^2/\eta$. The current localization is significant for large Hall parameters ($\kappa = 4$) that show a series of current corrugations aligned to the background field (see Figures 5.9c and d). This wave type current structure is discussed in the next section. The development of a planar current sheet, due to the Hall-induced axial field (Z), can lead to enhanced dissipation over the traditional $d_i = 0$ models. It is clear from Figures 5.10a and b that the use of moderate values of d_i allows for enhanced dissipation, especially when $d_i >> \sqrt{\eta}$, as the Hall current layers develop.

5.3.7 Axial current and axial field structure

First, we discuss the modification of the traditional current sheet structure when the Hall term is introduced. In Figure 5.11, we show the purely resistive localization $\eta = 0.005, d_i = 0$ of the axial current at three different Alfvén times. The plots

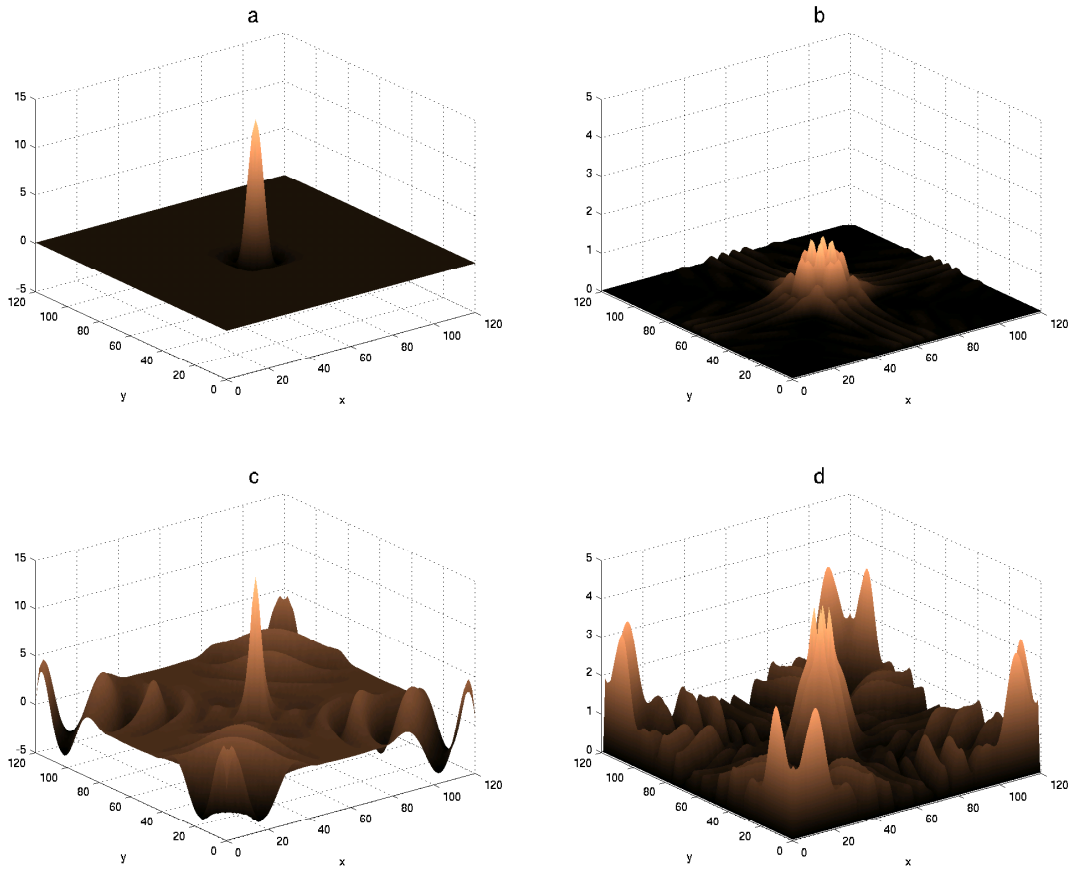

Figure 5.9: The axial current component when (**a**) $\kappa = 0.2$ and (**c**) $\kappa = 4.0$. The magnitude of the planar current when (**b**) $\kappa = 0.2$ and (**d**) $\kappa = 4.0$. Each run is at the time of maximum dissipation for given resistivity $\eta = 0.005$.

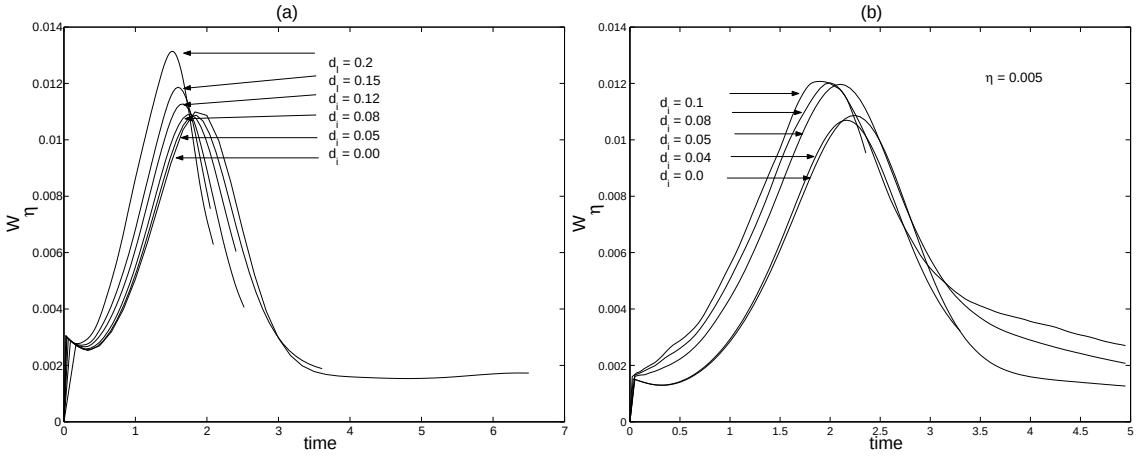

Figure 5.10: Ohmic dissipation rate versus time for various values of ion skin depth. In (**a**) $\eta = 0.01$ and (**b**) $\eta = 0.005$. The dissipation rate is not appreciably changed for small values of Hall term $d_i << \sqrt{\eta}$.

highlight the initial implosive phase as the disturbance field propagates towards the neutral point. As mentioned in §5.3.5, the reconnecting current winds up localized in a quasi-cylindrical spike of area η and amplitude η^{-1} centered on the origin. In particular the current contours close to the diffusion region remain approximately circular for all times up to the time of current maximum ($t \simeq 2$).

In Figures 5.12 and 5.13, we perform identical computations but include the influence of the Hall current for $d_i = \sqrt{\eta}$ and $d_i = 2\sqrt{\eta}$ respectively. It is clear that the morphology of the current changes markedly when the Hall term is added. For $d_i \simeq \sqrt{\eta}$ the contours (Figure 5.12) develop a quadripolar tendency but localization is still achieved by the time of current maximum. Figure 5.13 shows however, that for runs with a sufficiently large Hall parameter $d_i = 2\sqrt{\eta}$, current localization may be significantly compromised. A central spike is still present but the outer field now shows a series of current corrugations aligned to the background field. It is interesting that similar stratifications (for $d_i >> \sqrt{\eta}$) have been observed for in-

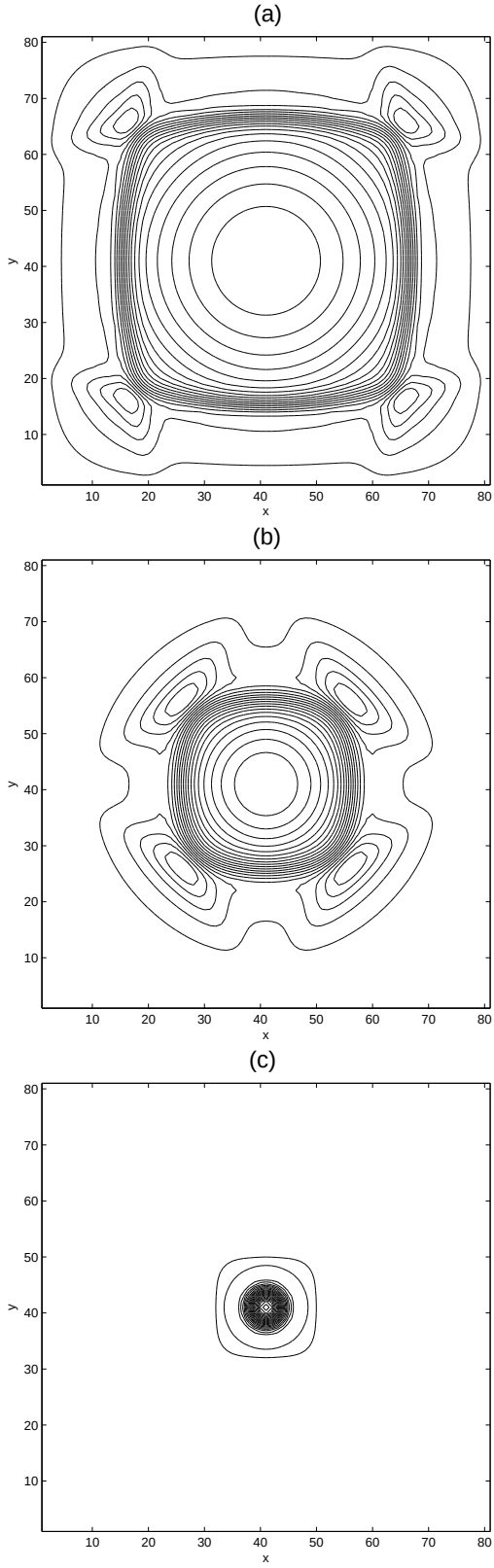

Figure 5.11: Localization of current density ($-\nabla^2\psi\,\hat{\mathbf{z}}$) contours for $d = 0$ and $\eta = 0.005$, after: (**a**) 1/2 an Alfvén time, (**b**) 1 Alfvén time and (**c**) time of maximum current ($t \sim 2$).

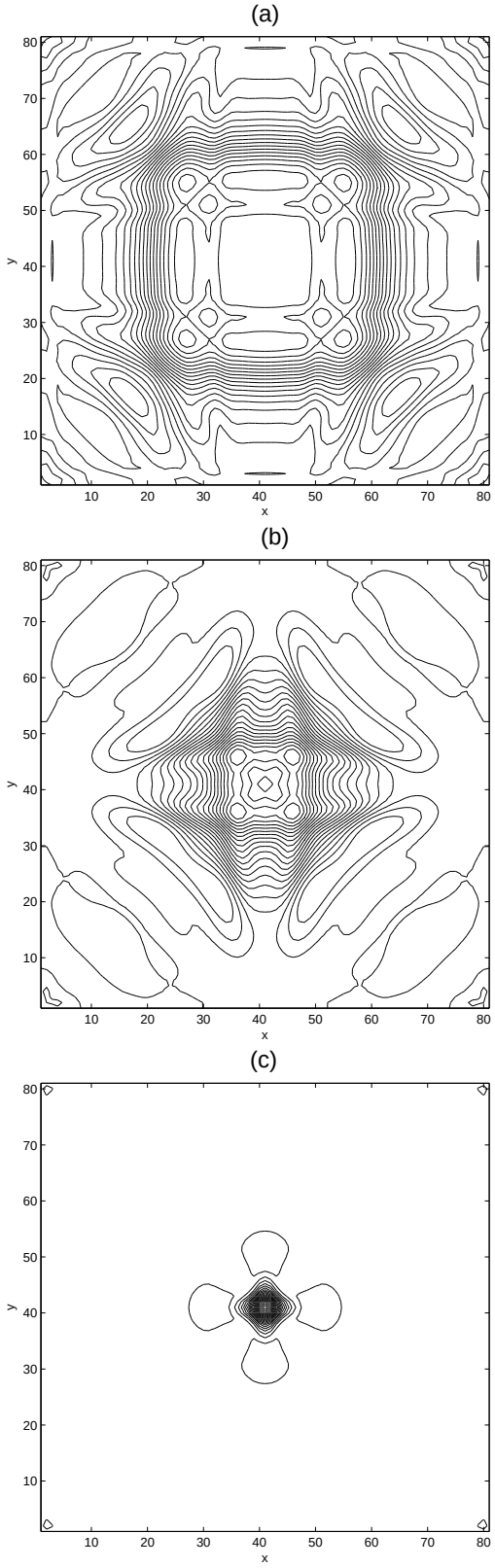

Figure 5.12: Localization of current density ($-\nabla^2\psi\,\hat{\mathbf{z}}$)) contours for $d_i = \sqrt{\eta}$, with $\eta = 0.005$, after: (**a**) 1/2 an Alfvén time, (**b**) 1 Alfvén time and (**c**) time of maximum current ($t \sim 2$).

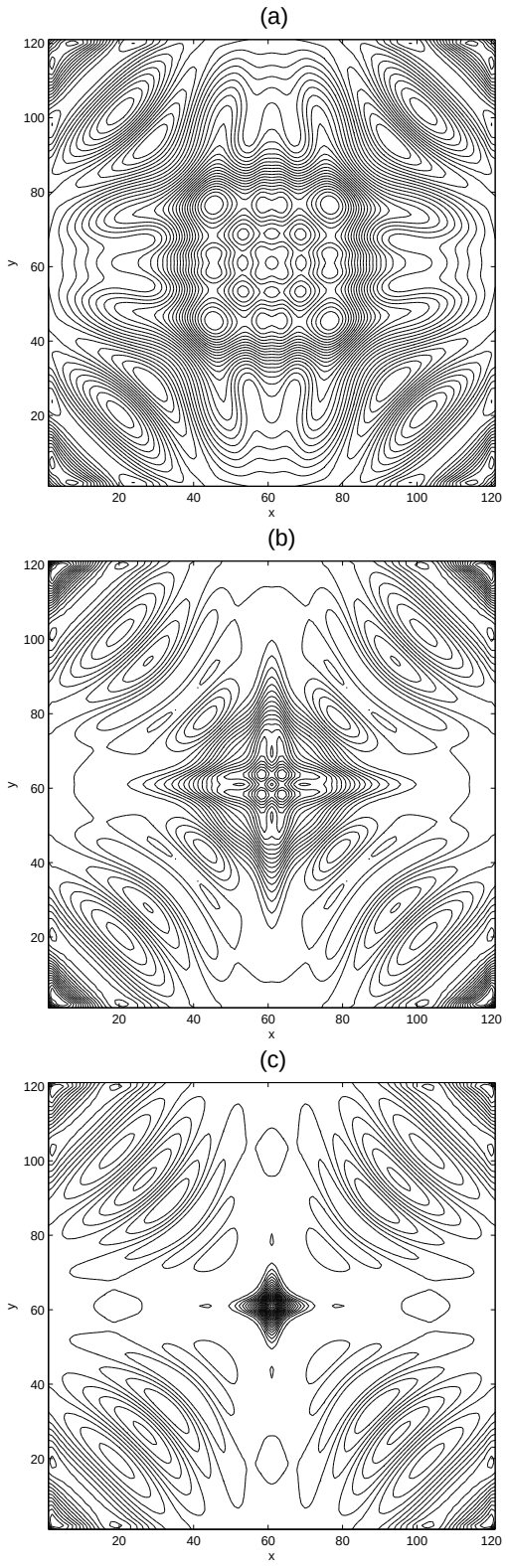

Figure 5.13: Localization of current density ($-\nabla^2\psi\,\hat{\mathbf{z}}$) contours for $d_i = 2\sqrt{\eta}$, with $\eta = 0.005$, after: (**a**) 1/2 an Alfvén time, (**b**) 1 Alfvén time and (**c**) time of maximum current ($t \sim 2$).

compressible, steady state merging in open X-point geometries (Craig & Watson, 2003). Such current corrugations are probably a signature of whistler wave modes whose high frequencies are not effectively damped (Fitzpatrick, 2004) by purely collisional resistivities. Notably, Fitzpatrick and others have, for numerical expedience, added an empirical hyper-resistivity into the system to control these oscillatory wave modes.

We now explore the influence of Hall current on the structure of axial field $Z(x, y)$. Figure 5.14 shows contour of the $Z(x, y)$ field at an early time stage ($t = 0.95$) reconnection process for parameters $\eta = 0.003$ and $d_i = 0.03$. According to the induction argument of §5.2.2, the Z field structure is developed from the directional derivative of the axial current, that is $(\mathbf{B}_E \cdot \nabla) \nabla^2 \psi$. The validity of this argument can be checked by computing the phase relations between the integrated axial current and the induced axial fields. According to equation (5.12), the two phases can be expected to follow same time period shifted by a phase of $\pi/2$. We have plotted in Figure 5.15, the integrated Z field (Z_m) and integrated axial current (J_{zm}) for the time interval $\leq t \leq 40$, over the region Δ enclosed by the sector of the positive quadrant with $y > x$. The measure is defined by

$$X_m = \int_\Delta X(x, y, t) dx dy \tag{5.33}$$

over the region Δ. Once the oscillatory behaviour is established, the measured axial field, represented by solid line remains $\pi/2$ out of phase with the axial current. Figure 5.16 shows the similar argument that the same quantities can be expected for the axial velocity field. The time plot of the integrated axial velocity field (W_m) shown in Figure 5.16, tracks the J_{zm} remarkably accurately. These time measures provide convincing signatures for Hall current reconnection.

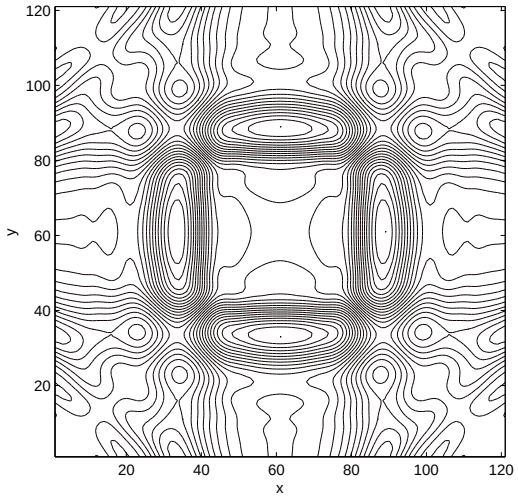

Figure 5.14: Plot of axial field $Z(x, y)$ at $t \simeq 1$. The quadrapolar structure derives from the directional derivatives of the axial current long the X-point field lines ($\eta = 0.003$, $d_i = 0.03$, $\kappa \simeq 1$.)

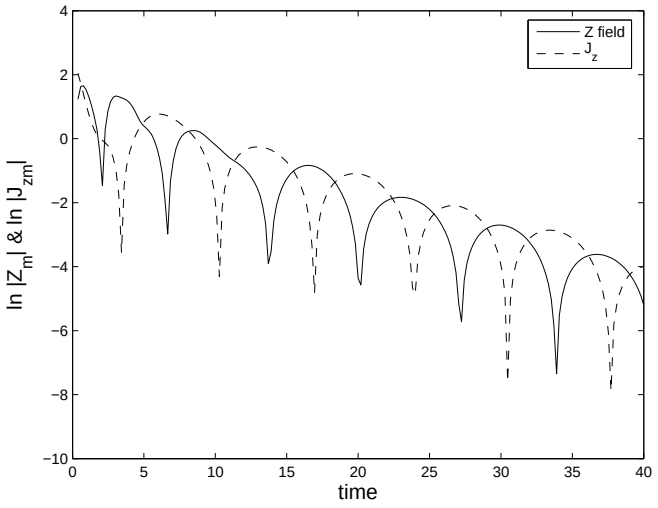

Figure 5.15: Plot shows $\ln |Z_m|$ (solid line) and $\ln |(J_z)_m|$ (dashed line) against time. The traces are approximately 90 degrees out of phase ($\eta = 0.003$, $d_i = 0.03$, $\kappa \simeq 1$).

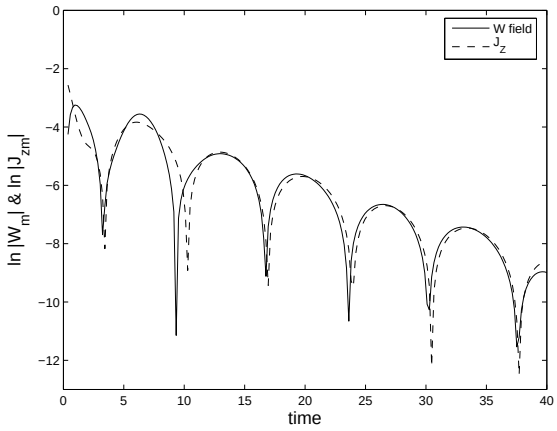

Figure 5.16: Plot shows $\ln|W_m|$ (solid line) and $\ln|(J_z)_m|$ (dashed line) against time for the parameters of Figure 5.15.

5.4 Conclusions

In this chapter we have considered the evolution of X-type neutral points in the presence of Hall currents. The dynamic evolution of X-point system is governed by two small external parameters, the dimensionless resistivity η and the normalized ion skin depth d_i. The results suggest that the Hall current can significantly alter the resistive solution ($d_i = 0$) when

$$d_i{}^2 \geq \eta,$$

a condition which is easily satisfied for collisional coronal plasmas ($\eta \simeq 10^{-14.5}$, $d_i \simeq 10^{-6.5}$). The axial field which is induced by Hall term, feeds back on the system altering the reconnection rate and dissipation rate over the region.

More specifically, our numerical results show that the Hall current can manifest itself in several distinct ways. In Chapter 3 we noted that in purely resistive plasmas ($d_i = 0$), the main dissipation phase is dominated by oscillatory eigenmodes whose frequency and decay rate depend only logarithmically on the plasma resistivity. These modes persist for $d_i > 0$, but the decay rate is notably enhanced and the

oscillation rate is reduced. Scaling laws between ω and α presented in §5.3.3, suggest that the enhanced decay rate (α) may be associated with stronger localizations of the current density for $d_i > 0$. However, the enhanced decay rate is not independent of the system size; it scales as l_c^{-1} suggesting that the Hall current becomes more effective for smaller magnetic structures.

We have also emphasized that Hall currents influence the transient implosion phase which acts as a precursor to eigenmode development. Although the Ohmic dissipation rate resulting from the initial collapse is enhanced, the reconnection rate behaves more ambiguously: it suffers an initial decline before increasing for $d_i^* \geq \eta^{1/3}$ (Figure 5.8b). The structure of the reconnection current also undergoes dramatic changes in this regime: the localized cylindrical currents which dominate the purely resistive calculation, eventually give way to current corrugations, aligned to the background field, which extend throughout the X-point. This behaviour has also been witnessed in computations of incompressible merging in open geometries, and may provide a useful signature for identifying strong Hall current effects (Craig et al., 2003).

In summary, the present X-point computations reveal that Hall currents can influence reconnection rates, Ohmic dissipation rates and the geometry of the reconnecting fields in a variety of ways. Although we have considered only small amplitude disturbances about a planar X-point, it is clear that many of our findings are consistent with Hall current merging studies in other geometries as discussed in Chapter 6. Notably when reconnection rates are enhanced by Hall effects, the current localization becomes more intense and the problem of exceeding the current density thresholds based on the ion-acoustic limit—already a problem in conventional MHD—may be worsened. It follows that the inclusion of Hall effects within a generalized Ohm's law, may still be insufficient to provide a realistic description of magnetic merging based on collisional resistivities.

Chapter 6

Transient merging solutions based on the generalized Ohm's law

6.1 Introduction

In Chapter 3 we discussed a number of magnetic merging reconnection solutions based on two distinct approaches. The first approach is provided by the X-point collapse model, modified to include viscosity and Hall currents in Chapter 4 and Chapter 5 respectively. In both cases a uniform background density ρ_0 is assumed based on a compressible pressureless plasma. The aim of Chapter 5 was to employ a more generalized version of Ohm's law, with specific attention being paid to the Hall term. This version of Ohm's law also includes collisionless quantities such as finite electron inertia, electron pressure gradient as well as the Hall current.

An alternative approach based on steady-state incompressible merging in an "open geometry" has been developed by many authors over the years (Sweet, 1958; Parker, 1957, 1963; Petschek, 1964; Syrovatskii, 1971; Craig & Henton, 1995). Exact solutions introduced by Craig & Henton (1995) are now available that describe steady-state reconnection in planar geometry.

After Craig & Henton (1995), several authors extended the exact merging solution. A further class of exact collisional resistive "spine current models" was developed by Craig & Fabling (1996), Craig, Fabling & Watson (1997) and Craig & Watson (2000b) but, the analysis was based on the traditional Ohm's law. The generalized Ohm's law was incorporated within a broad class of $2D$ and $3D$ reconnection solutions by Bhattacharjee, Ma & Wang (1999), Shay *et al* (1999), Craig & Watson (2003) and Craig & Watson (2005) including Hall current and electron inertial effects. The latter studies showed analytically that planar merging solutions could be significantly affected only for $d_i^2 > \eta$, where d_i is the non-dimensional Hall coefficient and η the non-dimensional resistivity. Craig et al. (2003) extended these results by testing the analytic prediction using a Hall-MHD code. Their results suggested that the reconnection rate in fact decreases when the merging contains significant shear flows. However, they also suggested that an increase in the reconnection rate was possible in the absence of shear flows.

In this chapter we employ an analytic reduction of the MHD equations to study time dependant incompressible merging in an open reconnection geometry. This approach contrasts with results obtained in the compressible "closed" X-point geometry of Chapters 4 and 5. In particular, in Chapter 5 has shown that the Hall term can provide a series of current corrugations aligned to the background field by the Hall current (Craig & Watson, 2003; Fitzpatrick, 2004). One aim of this chapter is to find some microscopic explanation of this oscillatory behaviour and to show how it links to the "Hall-resistive" length scale. The present approach also allows us to derive an analytic argument for how Hall current merging is influenced by the size of the reconnecting system. This is currently a hot topic in Hall-MHD reconnection research (Shay et al., 1999, Cassak et al., 2006; Bhattacharjee et al., 2005).

We are also interested in whether electron inertia can change reconnection prop-

erties such as field structure, current width and reconnection rate. Even though we find that electron inertia is likely to have little impact on coronal problems, we expect that it can influence the above properties in combination with the Hall current.

In §6.2, we introduce the dimensionless MHD equations with a generalized Ohm's law, as derived in Chapter 2. Solutions with Hall term and electron inertia term are discussed in §6.3 and §6.4 respectively. Here, we introduce a new simulation code which employs implicit time integration that allows larger values of the Hall and electron inertia terms to be economically computed. Further we introduce some qualitative predictions based on the combination of Hall and inertial effects in §6.5.

6.2 MHD with a generalized Ohm's law

We begin by considering the problem of constructing reconnection solutions in an incompressible plasma of uniform mass density ρ. Recall that equations of MHD with Hall effect (d_i) and electron inertial effect (d_e), comprise the continuity equation (2.25)

$$\frac{\partial \rho}{\partial t} + \nabla \cdot (\rho \mathbf{v}) = 0 \tag{6.1}$$

the momentum equation (2.26),

$$\rho \left(\frac{\partial \mathbf{v}}{\partial t} + (\mathbf{v} \cdot \nabla)\mathbf{v} \right) = -\nabla p + \mathbf{J} \times \mathbf{B}, \tag{6.2}$$

and the induction equation (2.27),

$$\frac{\partial \mathbf{B}}{\partial t} = \nabla \times (\mathbf{v} \times \mathbf{B}) - \eta \nabla \times \mathbf{J} - d_i \nabla \times (\mathbf{J} \times \mathbf{B} - \nabla p_e) - d_e \nabla \times \left(\frac{\partial \mathbf{J}}{\partial t} + \nabla \cdot [\mathbf{J}\mathbf{v} + \mathbf{v}\mathbf{J}] \right). \tag{6.3}$$

We also have the divergence constraints

$$\nabla \cdot \mathbf{v} = \nabla \cdot \mathbf{B} = 0. \tag{6.4}$$

These equations are non-dimensionalized with respect to the reference coronal values (see table 2.1), with time being measured in Alfvén times $\tau_A = l_c/v_A$.

In traditional non-Hall current MHD models with $d_i = d_e = 0$, the resistivity η provides the only avenue for extracting energy from the magnetic field. Since we neglect viscosity in this chapter, energy can be removed from the system only by Ohmic dissipation. Since coronal resistivities are always very small, the Ohmic dissipation rate is generally so small that the magnetic field is almost completely frozen into plasma. It follows that topological change by magnetic reconnection can be effective only in regions of high current density.

6.2.1 Planar merging equations

We investigate solutions in so called $2\frac{1}{2}D$ geometry where $\partial_z = 0$. In this case all variables are functions of x and y only, though they may still have three spatial components. Under this assumption, the planar components of the magnetic and velocity fields may be expressed in terms of flux (ψ) and stream (ϕ) functions. Hence we have representations for the $\mathbf{v}$ and $\mathbf{B}$ fields

$$\mathbf{v}(x, y, t) = \nabla\phi \times \hat{\mathbf{z}} + \mathcal{W}\hat{\mathbf{z}}, \tag{6.5}$$

$$\mathbf{B}(x, y, t) = \nabla\psi \times \hat{\mathbf{z}} + \mathcal{Z}\hat{\mathbf{z}}. \tag{6.6}$$

In components $\mathbf{v} = (\phi_y, -\phi_x, \mathcal{W})$ and $\mathbf{B} = (\psi_y, -\psi_x, \mathcal{Z})$, where subscripted variables denote partial derivatives. The symbols $\mathcal{W}$ and $\mathcal{Z}$ represent axial components of the velocity and magnetic field respectively. Note that the current density

$$\mathbf{J} = (\mathcal{Z}_y, -\mathcal{Z}_x, -\nabla^2\psi) \tag{6.7}$$

comprises both axial and planar contributions. From the curl of the momentum equation we note that the planar components of the velocity field satisfy

$$\nabla^2\phi_t + [\nabla^2\phi, \phi] = [\nabla^2\psi, \psi], \tag{6.8}$$

while

$$\mathcal{W}_t + [\mathcal{W}, \phi] = [\mathcal{Z}, \psi]. \tag{6.9}$$

The z-component of Ohm's law gives

$$\psi_t + [\psi, \phi] = \eta\nabla^2\psi + d_i[\psi, \mathcal{Z}] + d_e(\nabla^2\psi_t + [\nabla^2\psi, \phi] + [\mathcal{Z}, \mathcal{W}]), \tag{6.10}$$

while the x and y-components can be combined to give the perpendicular field equation

$$\mathcal{Z}_t + [\mathcal{Z}, \phi] = \eta\nabla^2\mathcal{Z} + [\mathcal{W}, \psi] + d_i[\nabla^2\psi, \psi] + d_e(\nabla^2\mathcal{Z}_t + [\nabla^2\mathcal{Z}, \phi] + [\nabla^2\phi, \mathcal{Z}]). \tag{6.11}$$

In these equations we have employed the Poisson bracket notation defined by

$$[\psi, \phi] = \psi_x\phi_y - \phi_x\psi_y. \tag{6.12}$$

Equations (6.8)-(6.11) completely determine the planar reconnection problem. Note that here we have used the curled from of (6.2) to obtain (6.8) and (6.9), thereby avoiding explicit dependence on the pressure p.

6.2.2 Local and global field decomposition

We now turn to reconnection solutions including guide fields and reconnecting field components. The reconnecting fields are superposed on the large scale background guide fields. The potentials are given by

$$\phi = -\alpha xy + f(x,t), \tag{6.13}$$

$$\psi = \beta xy + g(x,t), \tag{6.14}$$

with $\alpha > 0$ to maintain a global inflow, together with the axial velocity and magnetic fields

$$\mathcal{W} = \gamma xy + W(x,t), \tag{6.15}$$

$$\mathcal{Z} = \delta xy + Z(x,t). \tag{6.16}$$

The planar fields $f(x,t)$ and $g(x,t)$ are advected by the background scalar guide fields αxy and βxy. The axial fields $\mathcal{W}(x,t)$ and $\mathcal{Z}(x,t)$ have guide field components γxy and δxy respectively.

In order to achieve current localization successfully, $|\beta|$ must be in between zero and α (Craig & Watson, 2003). Since α must be chosen to reflect the Alfvénic exhaust speeds of material ejected from the sheet, it cannot be arbitrarily assigned. The condition, $0 \leq |\beta| < \alpha$, ensures strong localization of the disturbance field $g(x,t)$ in contrast with the tendency of the shear magnetic waves (for $\beta > 0$) to propagate energy out of the reconnection region (see §3.2.5). We also know that β determines the curvature of magnetic field lines entering the current sheet (Figure 6.1b). When $\beta = 0$, there is only magnetic annihilation of straight field lines, as illustrated in Figure 6.1a.

Substituting the above forms into the planar system (6.8-6.11) gives (Craig & Watson, 2005)

$$\frac{df}{dt} = -2\alpha f + \beta x g_x - 2\beta g, \tag{6.17}$$

$$\frac{dW}{dt} = \beta x Z_x - \gamma x f_x - \delta x g_x, \tag{6.18}$$

$$\frac{dg}{dt} = \beta x f_x + \eta g_{xx} + d_i\left(\delta x g_x - \beta x Z_x\right) + d_e\left(\frac{dg_{xx}}{dt} + \gamma x Z_x - \delta x W_x\right) \tag{6.19}$$

$$\frac{dZ}{dt} = \delta x f_x + \eta Z_{xx} + \beta x W_x - \gamma x g_x + d_i \beta x g_{xxx} + d_e\left(\frac{dZ_{xx}}{dt} + \delta x f_{xxx}\right) \tag{6.20}$$

where we have introduced the Lagrangian derivative

$$\frac{d}{dt} = \frac{\partial}{\partial t} + \mathbf{v}\cdot\nabla = \frac{\partial}{\partial t} - \alpha x \frac{\partial}{\partial x}. \tag{6.21}$$

We retain axial guide fields γ and δ in this stage for generality—and also to make the system size argument in §6.3.2. However, when computing numerical solutions in §6.3.3 and beyond, we set the axial guide fields to zero by taking $\gamma = \delta = 0$.

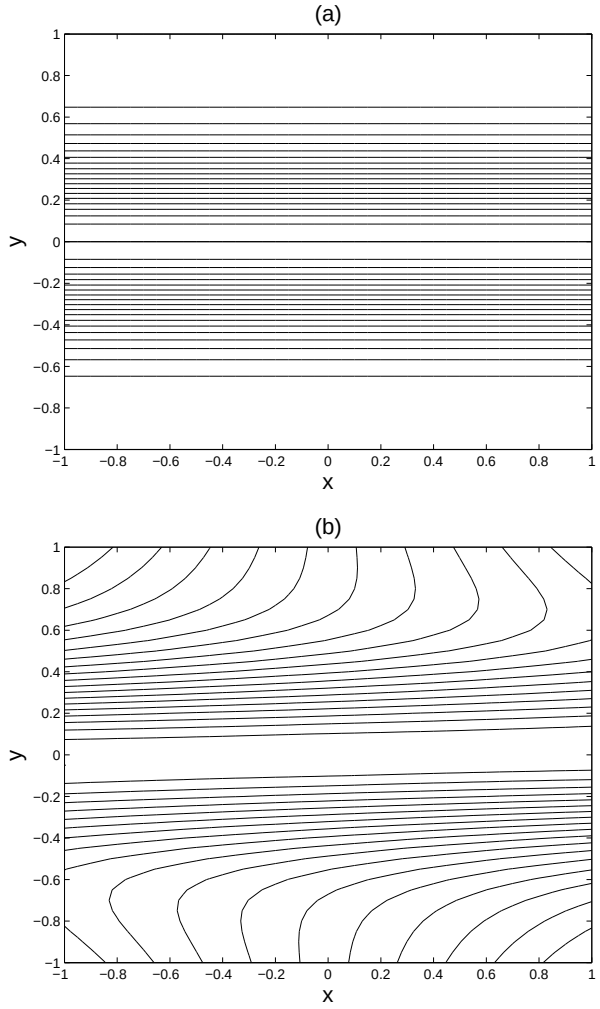

Figure 6.1: Magnetic field lines of an initial magnetic pulse of the form $\psi = \beta xy + g(x,0)$ (**a**) with $\beta = 0$ and (**b**) $\beta = 0.4$ where $g(x,0) = \exp(-7x^2)$. The magnitude of β determines the curvature of the magnetic field lines.

6.2.3 Numerical diagnostics of transient merging solutions

In this chapter, we employ an analytic reconnection model to investigate the effects of Hall currents and electron inertia on the magnetic fields and current properties. We simulate the merging solution numerically based on equations (6.17)-(6.20). We demonstrate

- the increase or decrease of the reconnection rate by altering the thickness of the current sheet,
- the change of the field structure,
- the development of the axial magnetic field,
- the size dependence of the reconnection rate

by the effects of Hall current and electron inertia. First of all we consider the purely resistive case in the absence of Hall current and electron inertial effects. In this simple case, $d_i = d_e = 0$, the planar fields evolve independently of the axial fields so we chose $W = 0$ and $Z = Z_0$ from (6.18) and (6.20) respectively.

We illustrate how the Hall current provides a mechanism by which strong separator fields can be induced by the planar reconnecting field components. Specially, we consider side by side comparison of Hall MHD versus resistive MHD. The induced axial field Z, for $\kappa >> 1$, where $\kappa = d_i^2/\eta$, dramatically modifies the characteristics of the merging, in particular the quasi-one-dimensional current sheets of traditional magnetic merging. The Z field modifies not only the axial current density but also leads to planar current densities in the (x, y) plane. Our last focus, however, is on how electron inertial effects act in tandem with the Hall current.

6.2.4 Numerical methods

In order to solve the governing partial differential equations numerically, we initially used a simple explicit finite difference code to evaluate the time dependent differential equations (6.17-6.20). These equations are numerically solved by a pentadiagonal system (Appendix B). The stability and accuracy of the explicit time integration become more restrictive for larger values of the Hall and inertia terms and necessitates a very small time step. To overcome these difficulties, we also use implicit time integration for larger values of the Hall and inertia terms as given in Appendix A.

The initial form of planar magnetic and velocity fields are

$$g(x,0) = \exp(-Ax^2), \quad f(x,0) = 0 \tag{6.22}$$

where we chose typically $A = 7$. The results to be discussed are insensitive to the form of the initial conditions. Also the axial potential field Z and axial velocity field W can initially be chosen as zero.

6.3 Hall current contribution

We consider in this section, a time dependent solution including Hall currents, but neglecting inertial effects. The equations (6.17)-(6.20) become,

$$\frac{df}{dt} = -2\alpha f + \beta x g_x - 2\beta g \tag{6.23}$$

$$\frac{dW}{dt} = \beta x Z_x - \gamma x f_x - \delta x g_x, \tag{6.24}$$

$$\frac{dg}{dt} = \beta x f_x + \eta g_{xx} + d_i \left(\delta x g_x - \beta x Z_x\right), \tag{6.25}$$

$$\frac{dZ}{dt} = \delta x f_x + \eta Z_{xx} + \beta x W_x - \gamma x g_x + d_i \beta x g_{xxx}, \tag{6.26}$$

with the Lagrangian derivative of (6.21). Equation (6.26) represents the development of the Z field which depends initially on the Hall term. The axial flow field

W is governed by (6.24). If we turn off the axial guide fields γ and δ from (6.24), the structure of the W-field derives from the directional derivative of the Z field only. Hence W-field remains $\pi/2$ out of phase with the axial Z-field (see §5.3.7 in Chapter 5). We can expect development of the axial fields Z and W by Hall current in the case of vanishing axial guide fields. In the case $d_i = 0$, we obtain a purely two-dimensional solution: the magnetic disturbance located in the outer field is advected and localized by the background scalar field αxy as it approaches the origin. As the result, a strong current layer develop at the origin.

6.3.1 Steady-state solution with axial guide fields

The ratio d_i^2/η determines the nature of the Hall merging exact steady-state planar reconnection solution (Craig & Watson, 2003). We will first revisit this argument which was originally based on a steady-state analysis.

Equations (6.26) and (6.25) give the scaling laws

$$Z \sim d_i \beta g_{xx} \tau, \quad Z \sim \frac{\eta g_{xx}}{d_i \beta}$$

which convert to new scaling law

$$(d_i \beta)^2 \sim \frac{\eta}{\tau},$$

where τ is a typical merging time scale. Assuming τ and β are order unity, implies that the Hall current plays a significant role when

$$d_i^2 > \eta. \tag{6.27}$$

The steady-state solutions for disturbance fields are found by substituting forms (6.13)-(6.16) into the planar reconnection equations (6.23)-(6.26). We recall the relation

$$f = -\frac{\beta}{\alpha} g, \tag{6.28}$$

from (3.24) in §3.2.5. A similar argument gives

$$W(x) = -\frac{\beta}{\alpha} Z(x) + \frac{1}{\alpha}\left(\delta + \frac{\beta\gamma}{\alpha}\right) g(x). \tag{6.29}$$

With these particular forms, equations (6.23) and (6.24) are satisfied identically, so that we are left with

$$\mathcal{E} - (\alpha^* + d_i\delta) x g' = \eta g'' - \beta d_i x Z', \tag{6.30}$$

$$-\alpha^* x Z' = \eta Z'' - \frac{\gamma}{\alpha}\alpha^* x g' + \beta d_i x g''' \,. \tag{6.31}$$

Here $\mathcal{E} = \partial\psi/\partial t$ is the flux transfer rate and $\alpha^* = (\alpha^2 - \beta^2)/\alpha$, while the other time derivatives vanish. The important observation is that β and d_i always appear together, meaning that the Hall current has no effect in 1-D merging unless shear flows are present.

6.3.2 Scaling of Hall current effects with system size

We demonstrate here how the system size influences the reconnection rate in exact magnetic reconnection solutions that include Hall current. The scaling property is based on the equations (6.23-6.26) with $\beta = 0$. This is the case of straight field line merging, but with an axial guide field with $\delta > 0$.

Recall that in Chapter 5, we have determined how the system size influences the Hall-resistive reconnection rate in line-tied X-point geometries. The results in §5.3.4 give the scaling

$$\frac{\Delta\alpha}{\alpha_0} \sim \frac{1}{l_c}$$

where $\Delta\alpha = \alpha - \alpha_0$ and α_0 is decay rate in the purely resistive case. The above result is based on the numerical treatment of the X-type neutral point solution. Here however, we now demonstrate the Hall current reconnection scaling based on the exact flux pile-up reconnections models.

We retain the axial guide fields (γ, $\delta \neq 0$), but let $\beta = 0$ which corresponds to the "head-on" annihilation of straight field-lines. From equation (6.30), a simple matching argument leads to the current layer scaling

$$x \sim r_s \simeq \left(\frac{\eta}{\alpha + \delta d_i}\right)^{1/2} \tag{6.32}$$

when x is very small. The Hall term clearly influences the thickness of the current sheet: when $\delta > 0$, the current sheet is thinner and when $\delta < 0$, the current sheet is thicker under the influence of d_i. However, when $\delta = 0$, (6.32) recovers the resistive length scale.

The reconnection rate is given by

$$\eta J_0 \simeq \frac{\eta B_s}{r_s}. \tag{6.33}$$

The resistive and Hall-resistive reconnection rates can be derived by substituting (6.32) into (6.33). When $\delta = 0$, the matching argument (6.32) gives us scaling of resistive reconnection rate

$$\eta J_0(\delta = 0) = B_s \alpha^{1/2} \eta^{1/2}. \tag{6.34}$$

When $\delta > 0$, the current sheet thickness is altered giving the Hall-resistive reconnection rate

$$\eta J_0^*(\delta > 0) = B_s \eta^{1/2} \alpha^{1/2} \left(1 + \frac{\delta d_i}{\alpha}\right)^{1/2}. \tag{6.35}$$

Finally, the increase of reconnection rate $\Delta(\eta J_0) = \eta J_0^* - \eta J_0$ normalized by α_0 is given by

$$\frac{\Delta(\eta J_0)}{\eta J_0} = \frac{\delta d_i}{\alpha} \sim d_i \sim \frac{1}{l_c}\ . \tag{6.36}$$

Once again we find no evidence for the idea that Hall-resistive reconnection rates do not depend on the system size (see §5.3.4).

6.3.3 Profiles of the planar magnetic disturbance field and axial magnetic field

We now return to the Hall current merging problem in the absence of axial guide fields setting $\delta = \gamma = 0$. We demonstrate here how magnetic field profiles are influenced by the Hall current using numerical simulations.

First, we simulate the pure resistive case with no Hall current. According to our computational model, the background field βxy is perturbed by $g(x,t)$ with the initial potential $g(x,0) = \exp(-7x^2)$. Figure 6.2 shows the localization of the $g(x,t)$, along the x-axis. Our simulations show that the gradient of the potential field increases until $t \sim 2$. Even though the velocity potential $f(x,0)$ is initially zero, it builds up to the level $f \simeq -\beta g/\alpha$ during the advection of the disturbance field, as mentioned in Craig, Heerikhuisen & Watson (2003). The planar magnetic field components along the x-axis are given by $B_x = 0$, $B_y = -\partial g/\partial x$. Hence only the B_y component of the planar field is present on the line $y = 0$. In particular, the axial field Z is initially zero and it will remain so in the purely resistive case.

Of particular interest is how Hall current can be incorporated in the exact reconnection solutions, and how the magnetic field in the collisional resistive treatment is modified by the Hall current contribution. Note that only Hall currents can influence the merging process in the case $\beta \neq 0$ of true reconnection.

Figure 6.3 shows $B_y = -\partial\phi/\partial x$ versus x along the line $y = 0$, for various values of κ $(= d_i^2/\eta)$ at the time of maximum peak magnetic field ($t \simeq 2$). The plot of the planar field for a small value of the Hall parameter $\kappa < 1.0$ is virtually identical to the purely resistive solution but, for large Hall parameter ($\kappa > 1.0$) the Hall current significantly modifies the collisional model as the planar magnetic field (B_y) develops oscillations in the outer field (Craig & Watson, 2003). The Hall current increases the amplitude of the sinusoidal oscillations of the outer field and decreases the peak value of the inner field.

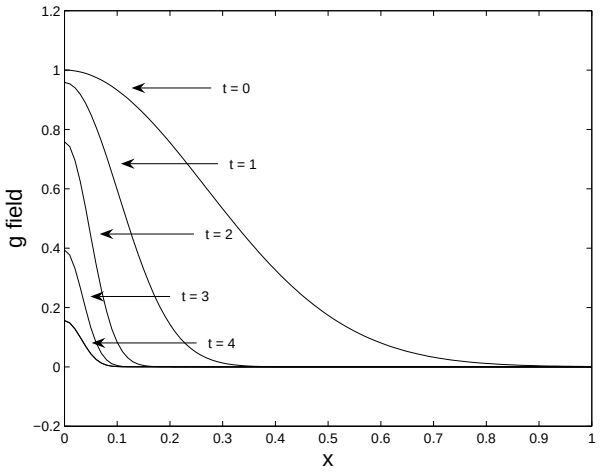

Figure 6.2: The potential field $g(x,t)$ along the line $y = 0$, evolves according to system of equations (6.23-6.26) for several time steps. The solutions are for the parameters values $\alpha = 1$, $\eta = 0.001$, $\kappa = 0$ and $\beta = 0.0$ where $\kappa = d_i^2/\eta$. Note that initially $g = \exp(-7x^2)$.

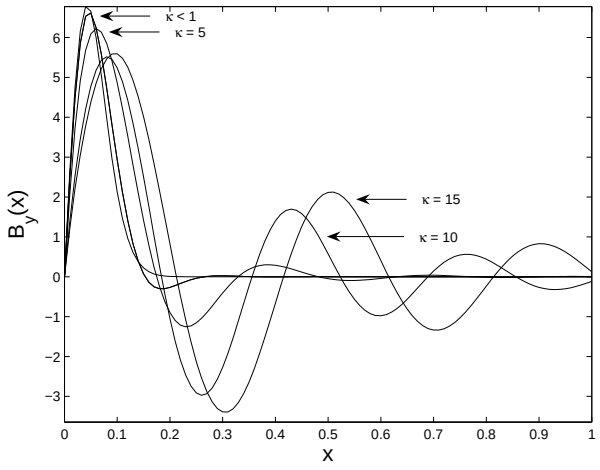

Figure 6.3: The planar field component $B_y = -\partial\psi/\partial x$ along the line $y = 0$, with the effect of the Hall current contribution for $\kappa = 5$, 10, 15 and $\kappa < 1$ where $\kappa = d_i^2/\eta$. The solutions are for the parameter values $\alpha = 1$, $\eta = 0.001$ and $\beta = 0.4$ and $t \simeq 3.0$.

We know that the axial field is only influenced by Hall current in the case of true reconnection ($\beta > 0$). Although the impact of the Hall current on the planar field for $\kappa << 1$ is small, its effects on the Z field are significant. The Z field is induced by the Hall current, achieving maximum field strength when $t \sim 3.5$. Figure 6.4 shows this behaviour for large values of Hall parameter $\kappa = 15$. The outer field begins to oscillate with increasing amplitude and decreasing wave length in the course of time. It is clear from Figure 6.5 that increases in the Hall parameter can increase the magnitude and oscillation of the Z field. The Hall current has a major impact on the axial field for the large values of Hall parameter ($\kappa > 1$).

The plot of the planar and axial magnetic fields along the x-axis gives some evidence of their field structure. For instance, we can expect oscillatory behaviour over the entire outer region, not only along the x-axis. The planar field $B_x = \partial\psi/\partial y$ vanishes along the x-axis, hence we can describe the structure of the planar and axial magnetic fields by considering the only $\hat{\mathbf{y}}$ and $\hat{\mathbf{z}}$ components. Figure 6.6a shows the structure of the fields $B_y = -\partial\psi/\partial x$ and $B_z = Z$ over the x-axis at the time $t = 3.5$. The fields oscillate out of phase in the outer region and the amplitude of the oscillations increase with time (Figure 6.6b).

6.3.4 Current sheet properties with Hall effects

In the case where Hall effects are neglected, the planar magnetic field develops a strong axial current layer throughout the plasma and the current sheet maintains one-dimensionality ($\mathbf{J} = -\nabla^2\psi\hat{\mathbf{z}}$). The axial current localizes toward the region by achieving the maximum current density when $t \simeq 2$. The current density is inversely proportional to the resistivity, as well as current width being proportional to $\eta^{1/2}$ as seen in Figure 6.7. The head-on ($\beta = 0$) reconnection models give a higher current density than sheared ($\beta \neq 0$) models and it is clear that the tendency for flux pile-up is relatively suppressed in the sheared solution.

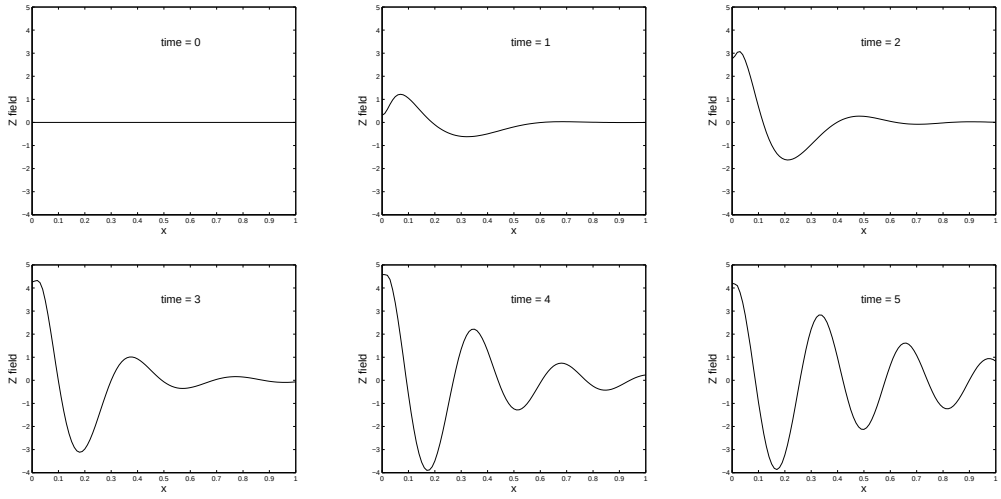

Figure 6.4: The development of Z field under the influence of the Hall current when $\kappa = 15$, evolves according to system of equations (6.23-6.26) for several time steps.

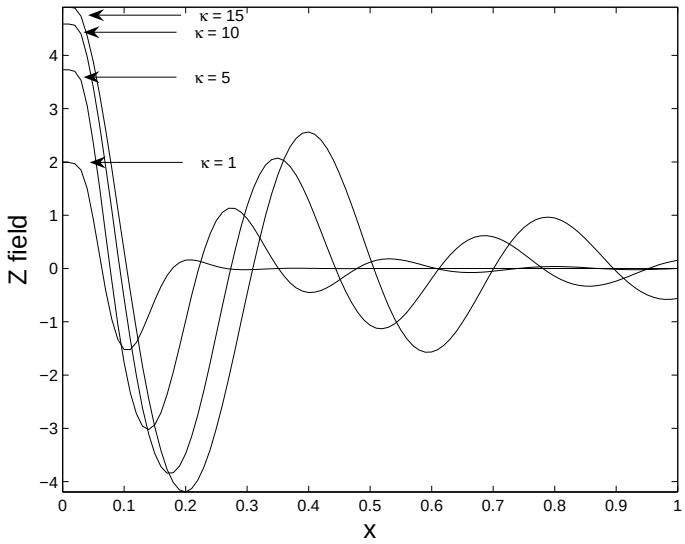

Figure 6.5: The maximum Z field for several values of κ namely $\kappa = 1$, 5, 10, 15. All solutions are for the parameters values $\alpha = 1$, $\eta = 0.001$ and $\beta = 0.4$.

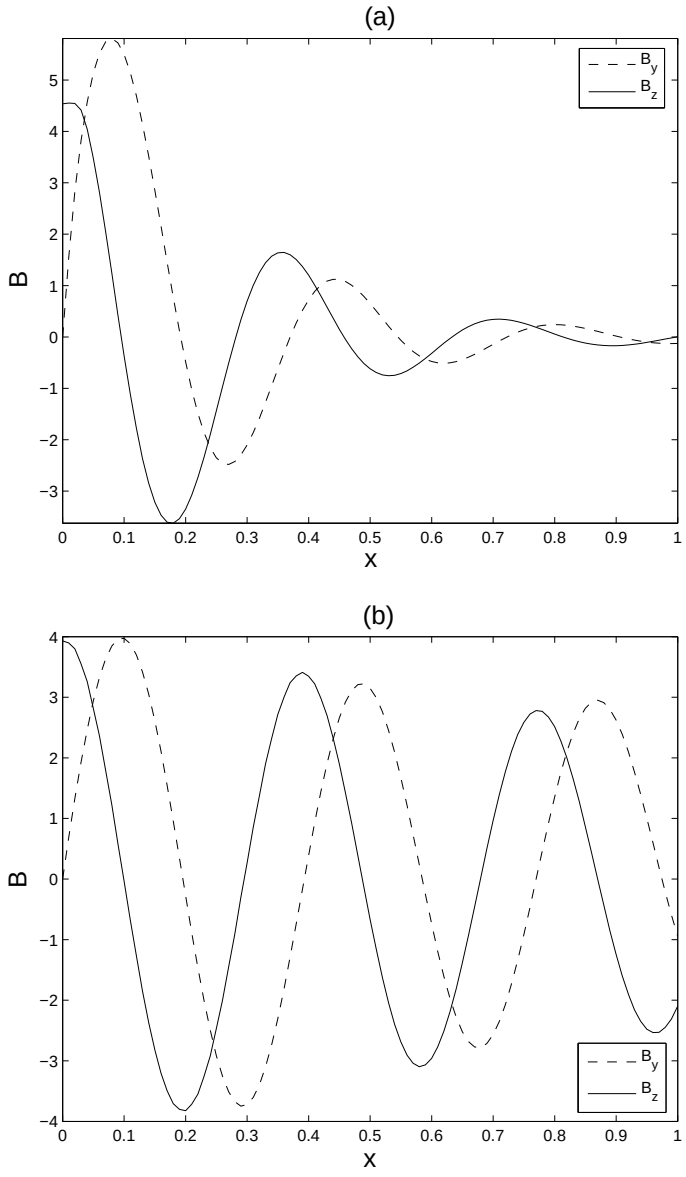

Figure 6.6: The magnetic field components $B_y = -\partial\psi/\partial x$ (dashed line) and $B_z = Z$ (solid line) along the line $y = 0$, evolves according to system of equations (6.23-6.26). Two field components show oscillatory behaviour. The parameter values are $\alpha = 1$, $\eta = 0.001$, $\kappa = 10$ and $\beta = 0.4$ where $\kappa = d_i^2/\eta$. (**a**) $t = 3.5$ and (**b**) $t = 6.3$.

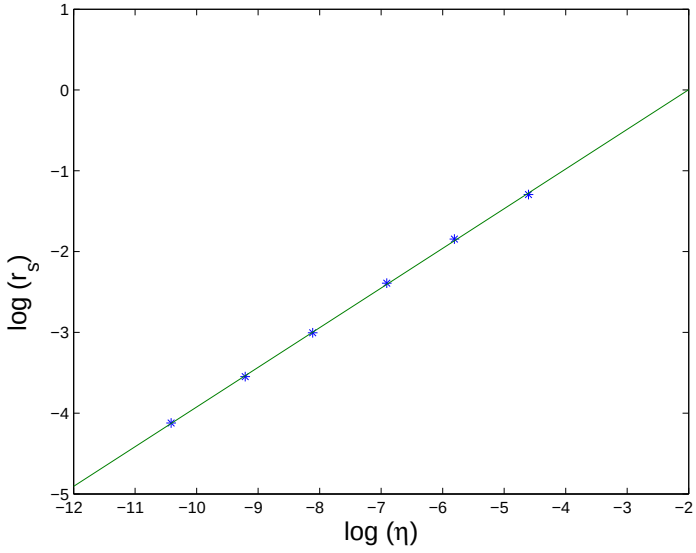

Figure 6.7: The width of the axial current changes with resistive term giving the relation $r_s \sim \eta^{1/2}$. Liner fit: $y = 0.49x + 0.98$.

As already mentioned, the current density

$$\mathbf{J} = (Z_y, -Z_x, -\nabla^2\psi)$$

comprises both axial and planar contributions under the influence of the Hall parameter in planar merging solutions. The current density along the $y = 0$ is given by

$$\mathbf{J} = (0, -Z_x, -\nabla^2\psi).$$

Figures 6.8a & b show the axial current density $J_z = |\nabla^2\psi|$ over the x-axis. It appears that there is a growing tendency to suppress the inner current sheet by Hall effects. For a small value of κ, namely $\kappa = 0.5$, as shown in Figure 6.8a, the current density is virtually indistinguishable from the pure collisional solution. However, for the large values of κ such as ($\kappa = 10$), the outer region magnetic field begins to oscillate sinusoidally and as a result, the strong axial current sheets develop in the outer field (Senanayake & Craig, 2006). At the same time, the planar currents

components develop, but the J_x component is zero along line $y = 0$. The J_y and J_z components generate the oscillatory current in the outer field. There is a continual interchange between J_y and J_z, as shown in the Figure 6.9.

6.3.5 Modification of traditional current sheet width by Hall current

Figure 6.10a shows the scaling of the current sheet width, r_s, with the collisionless ion skin depth, d_i, in the inner region. It can be seen that r_s is independent of d_i for d_i less than some value d_i^* (say). Figure 6.10b is the rescaled version of Figure 6.10a which shows current width increases most rapidly under the influence of the Hall current when $d_i > d_i^*$ where $d_i^* = \eta^{1/2}$. The behaviour shown in Figure 6.10b is compatible with the scaling results (6.27) discussed in §6.3.1 for the steady-state merging solution.

Moreover, when $d_i > \eta^{1/2}$, there is a good evidence from Figure 6.10b for the following Hall-MHD hybrid scaling of r_s

$$r_s \sim d_i^{1/2}\eta^{1/4}, \qquad d_i^2 > \eta. \tag{6.37}$$

These numerical results reveal that the plasma response enters the Hall-MHD regime when d_i exceeds $\eta^{1/2}$. Note that $r_s \sim \eta^{1/2}$ is the length scale of the pure collisional current layer (see Figure 6.7). The d_i can exceed the current sheet width but equation (6.37) confirms that in the Hall-MHD regime, the current width is always less than d_i in the limit $d_i > \eta^{1/2}$ (Fitzpatrick, 2004). A typical plasma with $\eta = 10^{-14.5}$ and $d_i = 10^{-6.5}$ gives the width of the current sheet

$$r_s \sim 10^{-6.75} \sim d_i. \tag{6.38}$$

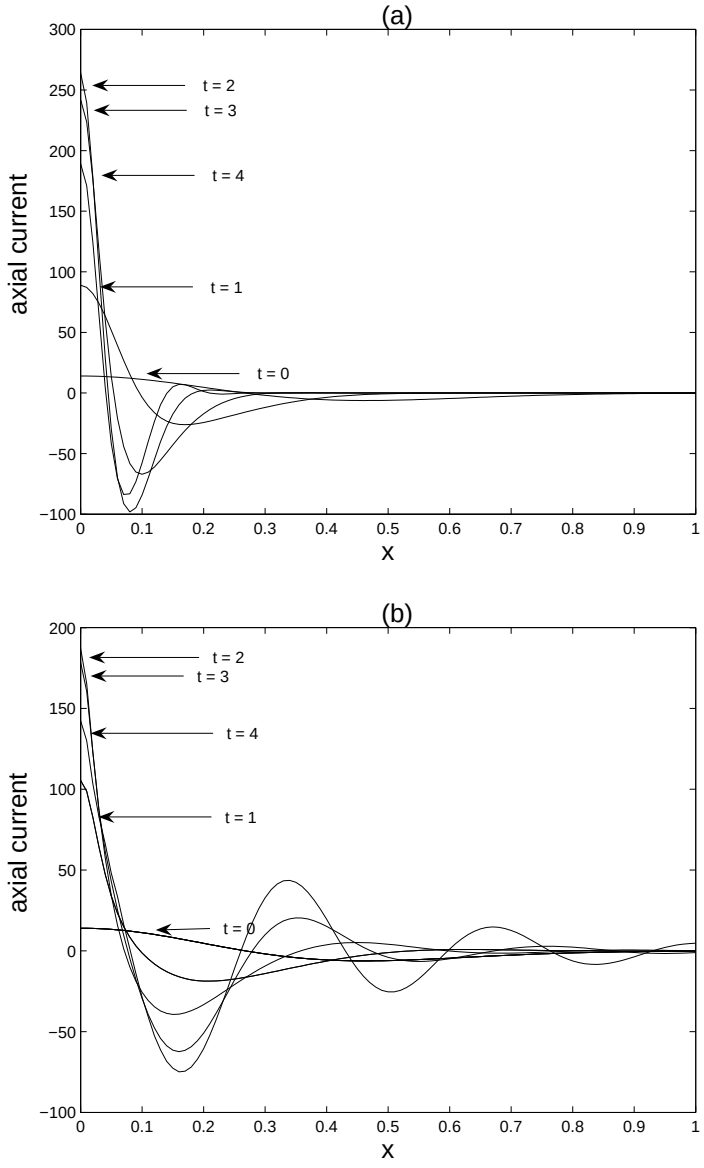

Figure 6.8: The axial current density $J = -\nabla^2\psi\hat{\mathbf{z}}$ along the line $y = 0$, evolves according to system of equations (6.23-6.26) for several time steps. The solutions are for the parameters values $\alpha = 1$, $\beta = 0.4$, $\eta = 0.001$, (**a**) $\kappa = 0.5$ and (**b**) $\kappa = 10$ where $\kappa = d_i^2/\eta$.

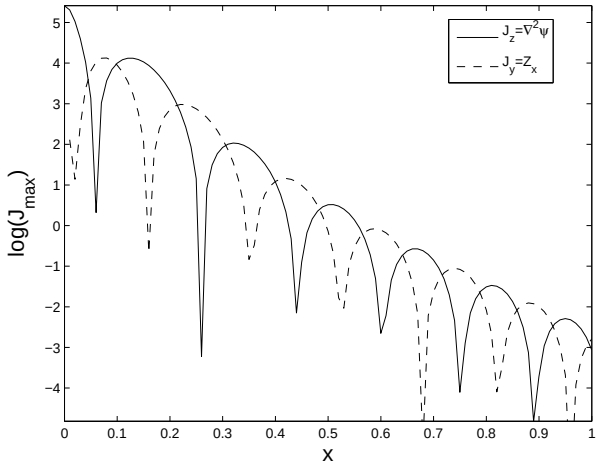

Figure 6.9: The logarithm of axial current density $J_z = |\nabla^2\psi\hat{\mathbf{z}}|$ (solid line) and planar current density $J_y = |\partial Z/\partial x|$ along the line $y = 0$ when $t \simeq 2.5$, evolve according to system of equations (6.23-6.26) for $\kappa = 5$. The solutions are for the parameters values $\alpha = 1$, $\eta = 0.001$, $\beta = 0.4$.

Microscopic interpretation of the Hall current width

The development of the current width, r_s, with the effects of the Hall current can be understood by considering current densities in the diffusion region. The charges moving in the $\hat{\mathbf{z}}$ direction of the current J_z will find themselves in a planar magnetic field $\mathbf{B} = (\psi_y, -\psi_x)$ which would cause them to gyrate by the Lorentz force. As a result, when the Hall coefficient is increased, the axial current component J_z is weakened and the planar current components develops. Figure 6.11 shows this behaviour in the inner region for a relatively large value of Hall coefficient ($\kappa = 15$). The red and green lines represent the axial current, J_z, when $d_i = 0$ and $d_i = 0.1$ respectively. The blue line represents the induce planar current, J_y, when $d_i = 0.1$.

From $0 \rightarrow A$ in Figure 6.11, the axial current component, J_z, decreases and negative current ($-J_y$) develops reaching a maximum during the first quarter of gyration. Figure 6.12 illustrates the change of J_z and J_y due to the Lorentz force.From

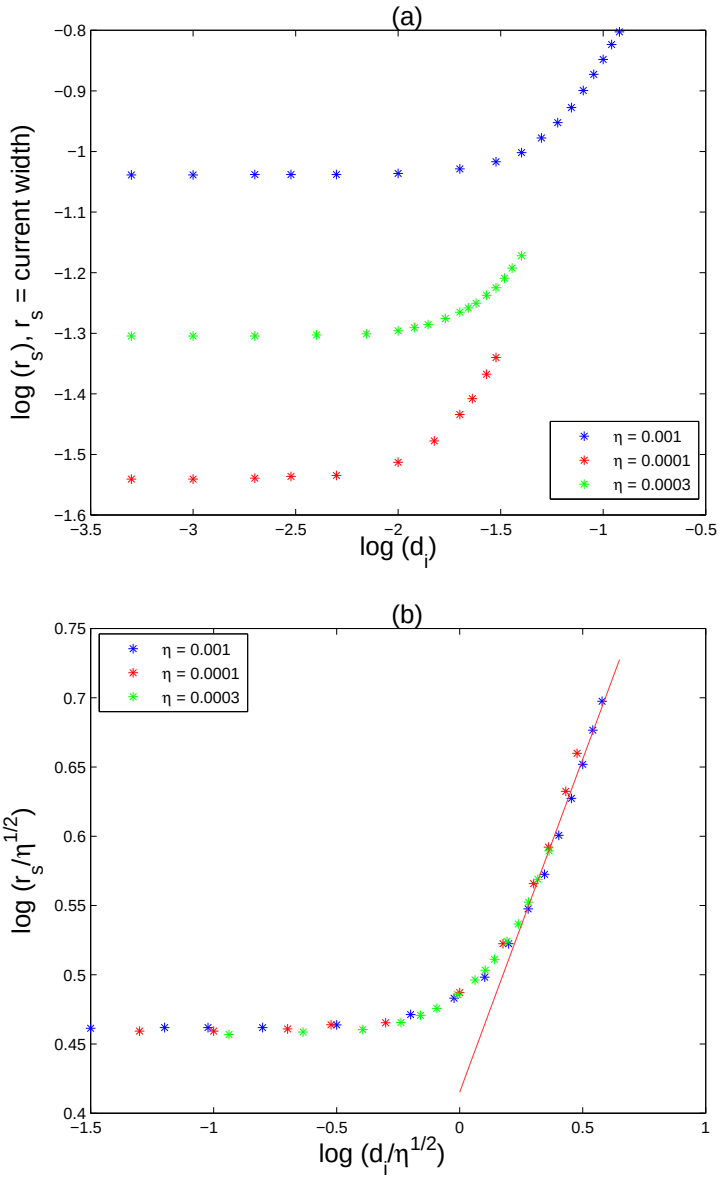

Figure 6.10: (**a**) Scaling of the current width, r_s, with the collisionless ion skin depth, d_i. (**b**) Scaling of the normalized current width, $r_s/\eta^{1/2}$, with the normalized collisionless ion skin depth, $d_i/\eta^{1/2}$. The solid straight line is a fit to $r_s\,\eta^{-1/2} \simeq (d_i/\eta^{1/2})^{1/2}$. Calculations were performed with $\alpha = 1$ and $\beta = 0.4$. The blue, green and red asterisks correspond to $\eta = 0.001$, 0.0003 and 0.0001 respectively.

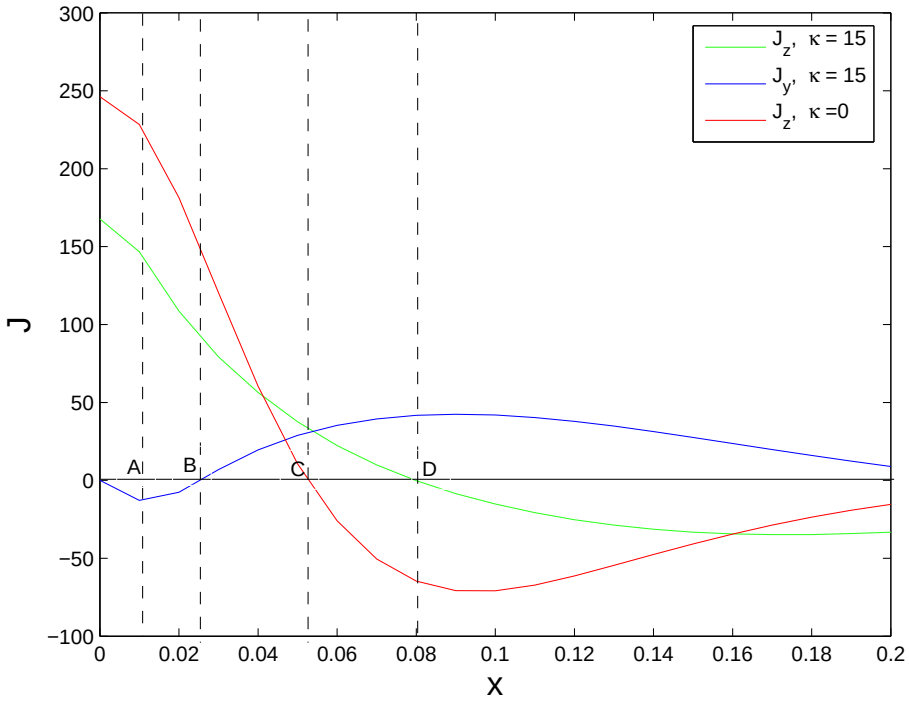

Figure 6.11: The behaviour of the J_z and J_y in the inner region for $\kappa = 15$. The red line corresponds to $J_z = -\nabla^2\psi$, $\kappa = 0$. The blue line corresponds to $J_z = -\nabla^2\psi$, $\kappa = 15$. The green line corresponds to $J_y = -\partial Z/\partial x$, $\kappa = 15$.

$A \rightarrow B$, the second quarter, the magnitude of J_y is reduced to zero and negative axial current is induced; as a result J_z is decreased rapidly (green line). From $B \rightarrow D$, the third quarter, the positive planar current component (blue line) is induced by gyration. In this stage, the induce negative axial current is decreased which means that slowdown the rate of J_z is decreased. As a result, the Hall current effects has lead to an increasing current sheet width and decreasing axial current. Thus OC is the resistive current width and OD is the Hall-resistive current width of the current layer. As discussed in the previous section, J_z and J_y alternate out of phase with each other in the outer region.

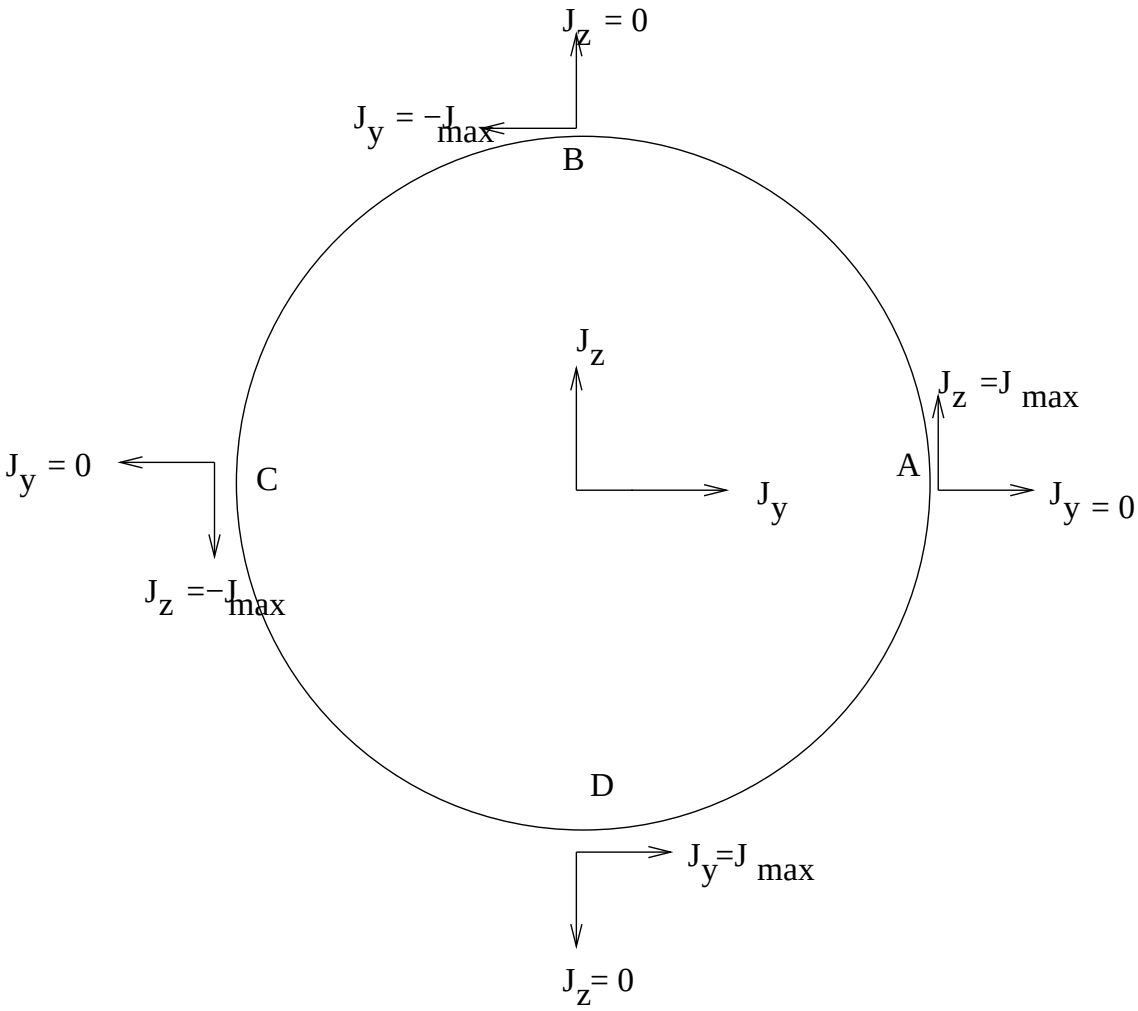

Figure 6.12: The figure explains the induced axial and planar current components J_z and J_y.

6.4 Importance of the inertia term

Although electron inertia, d_e, is known to have a negligible affect on the evolution of magnetic configurations when $d_e << \eta$, several authors have investigated the possible role of the electron inertial effects recognizing that purely resistive MHD cannot provide a full description. McClements et al (2004), for example, have modified the magnetic X-point reconnection solution of Craig & McClymont (1991) and Hassam (1992) to include electron inertial effects.

Putting $d_i = \delta = \gamma = 0$, equations (6.17-6.20) lead to system of equations

$$\frac{df}{dt} = -2\alpha f + \beta x g_x - 2\beta g, \tag{6.39}$$

$$\frac{dW}{dt} = \beta x Z_x, \tag{6.40}$$

$$\frac{dg}{dt} = \beta x f_x + \eta g_{xx} + d_e \frac{dg_{xx}}{dt}, \tag{6.41}$$

$$\frac{dZ}{dt} = \beta x W_x + \eta Z_{xx} + d_e \frac{dZ_{xx}}{dt}. \tag{6.42}$$

First we derive the head on reconnection solutions that include the role of the inertia term by putting $\beta = 0$ into the equations from (6.39)-(6.42). Taking

$$f = -\frac{\beta}{\alpha} g, \quad Z = Z_0$$

(Craig & Watson, 2003) where Z_0 is constant, we can set $W = Z = f = 0$. Now the system (6.39-6.42) is converted to single partial differential equation

$$g_t - \alpha x g_x = \eta g_{xx} + d_e(g_{xxt} - \alpha x g_{xxx}). \tag{6.43}$$

Following Craig & Watson (2003), we note that (6.43) can be solved analytically by taking

$$g(x,t) = A(t)\mathrm{e}^{ik(t)x}. \tag{6.44}$$

where $A(t)$ and $k(t)$ are functions of time only . The partial derivatives of (6.44) are given by

$$\begin{aligned} g_t &= \dot{A}\mathrm{e}^{ikx} + Ai\dot{k}x\mathrm{e}^{ikx} \\ g_x &= Aik\mathrm{e}^{ikx} \\ g_{xx} &= -Ak^2\mathrm{e}^{ikx} \\ g_{xxx} &= -Aik^3\mathrm{e}^{ikx} \\ g_{xxt} &= -\mathrm{e}^{ikx}(\dot{A}k^2 + 2Ak\dot{k} + Aik^2\dot{k}x). \end{aligned} \tag{6.45}$$

Substituting equations (6.45) into (6.43), the terms in x and terms independent of x are given by

$$[1 + d_e k^2]\dot{A}(t) + [\eta k^2 - 2d_e k\dot{k}]A(t) = 0, \quad \dot{k} - \alpha k = 0, \tag{6.46}$$

respectively. The solutions of the above equations are

$$A(t) = A_o \left(\frac{1 + d_e k_o^2}{1 + d_e k^2}\right)^{\nu}, \quad k = k_o e^{\alpha t} \tag{6.47}$$

where

$$\nu = 1 + \frac{\eta}{2d_e\alpha} \ .$$

For $\alpha > 0$, k grows exponentially with time and the amplitude ($A(t)$) of the disturbance $g(x,t)$ decreases monotonically with time. The magnetic field

$$B_y = -g_x = -A(t)k(t)e^{ik(t)x}, \tag{6.48}$$

has the magnitude Ak and this grows until the decay of $A(t)$ becomes appreciable. The field is maximum at the time τ_s when $d(Ak)/dt = 0$ and we find

$$\tau_s = \frac{1}{2\alpha} \ln\left(\frac{\alpha}{(\eta + d_e\alpha)k_0^2}\right) \tag{6.49}$$

corresponding to the wave-number k_s given by

$$k_s^2 = \frac{\alpha}{\eta + d_e\alpha}. \tag{6.50}$$

Since $\alpha > 0$, k_s^2 is always reduced by d_e. Equations (6.49) and (6.50) show that both the wave-number and time for localization decrease with the inertia term. Also,

inertial effects thicken the current sheet. Note that a purely collisional resistivity $\eta \simeq 10^{-14}$ leads to small length-scales and unphysical current densities when inertial effects are neglected. According to equation (6.49), the inertia term is effective at significantly thickening the sheet only if $d_e\alpha \geq \eta$. This condition cannot be achieved in coronal plasmas with $\eta = 10^{-14}$, $d_e = 10^{-16}$ and $\alpha \leq 10$. In any case, the limiting size scale represented by the initially dominated limit $k_s^2 = d_e^{-1}$ obtained by setting $\eta = 0$ in (6.50), still yields an unphysical sheet thickness $x_s \simeq 10^{-8} l_c \simeq 100$ cm. This thickness corresponds to a huge current density $J \simeq 2 \times 10^{10}$ (cgs units). Therefore, for typical coronal plasmas, it seems unlikely that inertia term can significantly reduce the huge current densities predicted by resistive models.

6.4.1 Profiles of planar magnetic disturbance field

We resolve (6.43) using the penta diagonal scheme discussed in Appendix B. Accuracy and stability of the numerical codes can be checked by comparison with analytical solutions given by equation (6.44). Figures 6.13a and b show that the analytic result differs slightly from numerical simulation. Analytically, the solution assumes a continuous sinusoidal wave form in an open geometry. Numerically however, we have to impose some artificial boundary conditions. In particular, we extend the region of merging by a placing a boundary at $x = 3l$ where l is length of the sinusoidal wave. This truncation introduces artifacts which lead to minor discrepancies in the analytic and numerical results.

We demonstrate here how electron inertial skin depth, d_e, controls the planar magnetic field. Recall that the B_x component is zero along the x-axis and the axial magnetic field B_z is zero everywhere. We set $\beta = 0$ which produces magnetic annihilation for the purpose of numerical treatment of the inertia term. We plot the field strength B_y versus x in Figure 6.14a at the time of maximum peak magnetic field for various values of d_e and the peak magnetic strength versus d_e/η in Figure

6.14b. Both plots show continuous reduction of the planar field with increases of the inertia term (d_e/η). We found in the previous section that a sinusoidal outer magnetic field was developed by the Hall term but not by the inertia term, because the Z field is influenced only by Hall current in the case of true reconnection.

6.4.2 Influence of the inertia term on the current sheet

The axial current density $\mathbf{J} = (0, 0, -\nabla^2\psi)$ is influenced by the inertia term. The planar magnetic field is reduced by d_e as shown in the previous section which implied that inertial effects can lead to appreciable reductions in axial current density. Figure 6.15 shows that maximum current at the origin is reduced by larger values of inertia terms. More quantitatively, in Figure 6.16a, we plot the computed normalized current density and the reconnection rate ηJ_0 for various values of d_e/η for given resistivities $\eta = 0.003$, 0.001, 0.0003 and 0.0001 with $\beta = 0$. The lines representing, ηJ_0 versus d_e/η for various values of η, seem to be identical so that the ratio d_e/η determines the nature of the merging solution. Inertial effects are significant when $d_e > \eta$ but in a coronal plasma the inertia term ($d_e \simeq 10^{-16}$) is less than the resistivity ($\eta \simeq 10^{-14}$). The numerical solution also indicates that the inertia term cannot significantly reduce the huge current densities in the solar corona predicted by collisional resistive models.

We also can investigate the role of the inertia term when $\beta \neq 0$. The parameter β specifies the degree of shear in the magnetic and velocity fields. As a result, the tendency for flux pile-up is relatively suppressed in the sheared solution (see §6.3.4). Figures 6.16a and b show us both head on ($\beta = 0$) and shear ($\beta \neq 0$) current densities are suppressed by the inertia term.

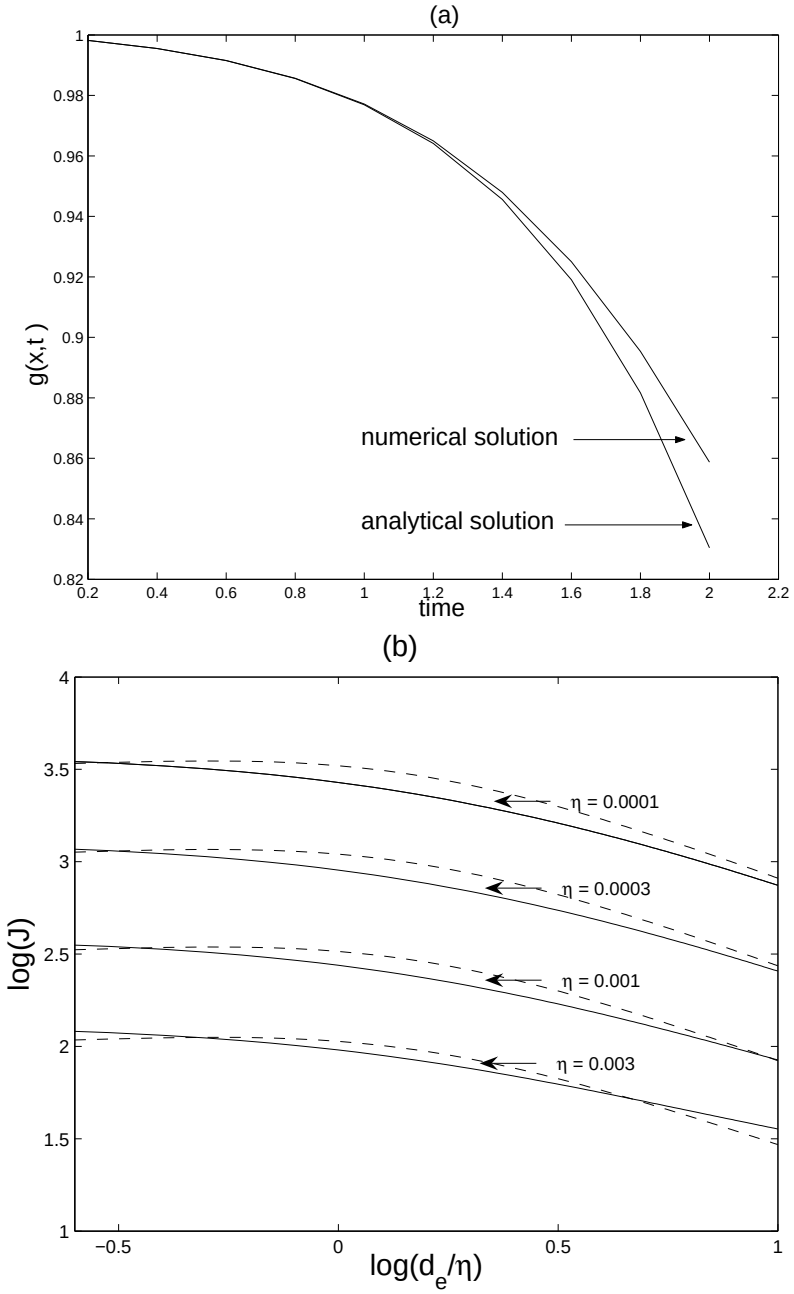

Figure 6.13: The plots show the effect of the electron inertia as the solutions of (6.43). In Figure 6.13b, the solid lines represent the numerical solutions and the dashed line represent the analytical solution. The parameters are $\eta = 0.001$, $d_e = 0.001$, $d_i = \beta = 0$.

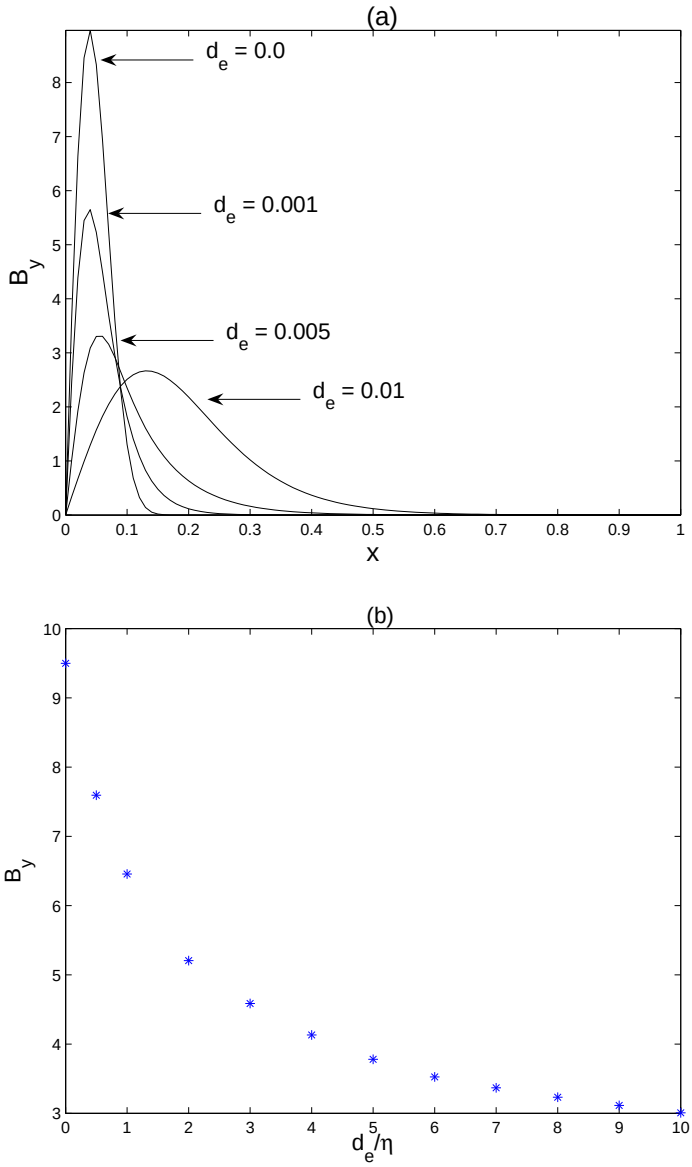

Figure 6.14: The planar field $B_y = -\partial g/\partial x$ of (6.43) for several values of the parameter d_e with $\beta = 0.0, d_i = 0.0$ and $\eta = 0.001$.

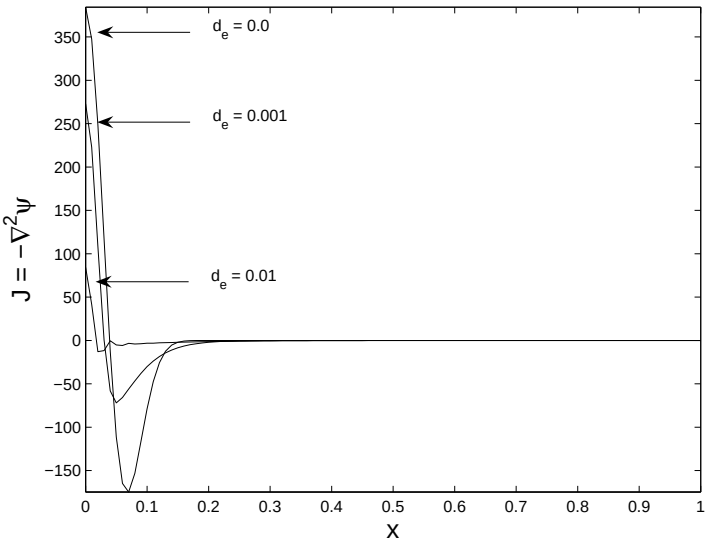

Figure 6.15: The maximum current density of (6.43) for the several values of the parameter d_e with $\beta = d_i = 0.0$.

6.5 Simultaneous effects of Hall electric field and electron inertia

Finally, we briefly consider the time dependent solution including both Hall current and electron inertial effects. We compute the evolution of the magnetic field and current density properties such as reconnection rate using system of equations (6.17)-(6.20) in the absence of the axial guide fields ($\gamma = \delta = 0$).

Recall that in the case $\kappa >> 1$, the field components B_y and B_z began to oscillate with the influence of the Hall current (§6.3.2). Also note that the individual effect of electron inertia does not produce corresponding oscillations because the axial field is always zero.

First we examine Hall-inertial effects for various d_e with fixed d_i and η. Figures 6.17a and b show how oscillations of the planar and axial fields change by the effects of electron inertia. The inertia term d_e can damp the oscillations and reduce

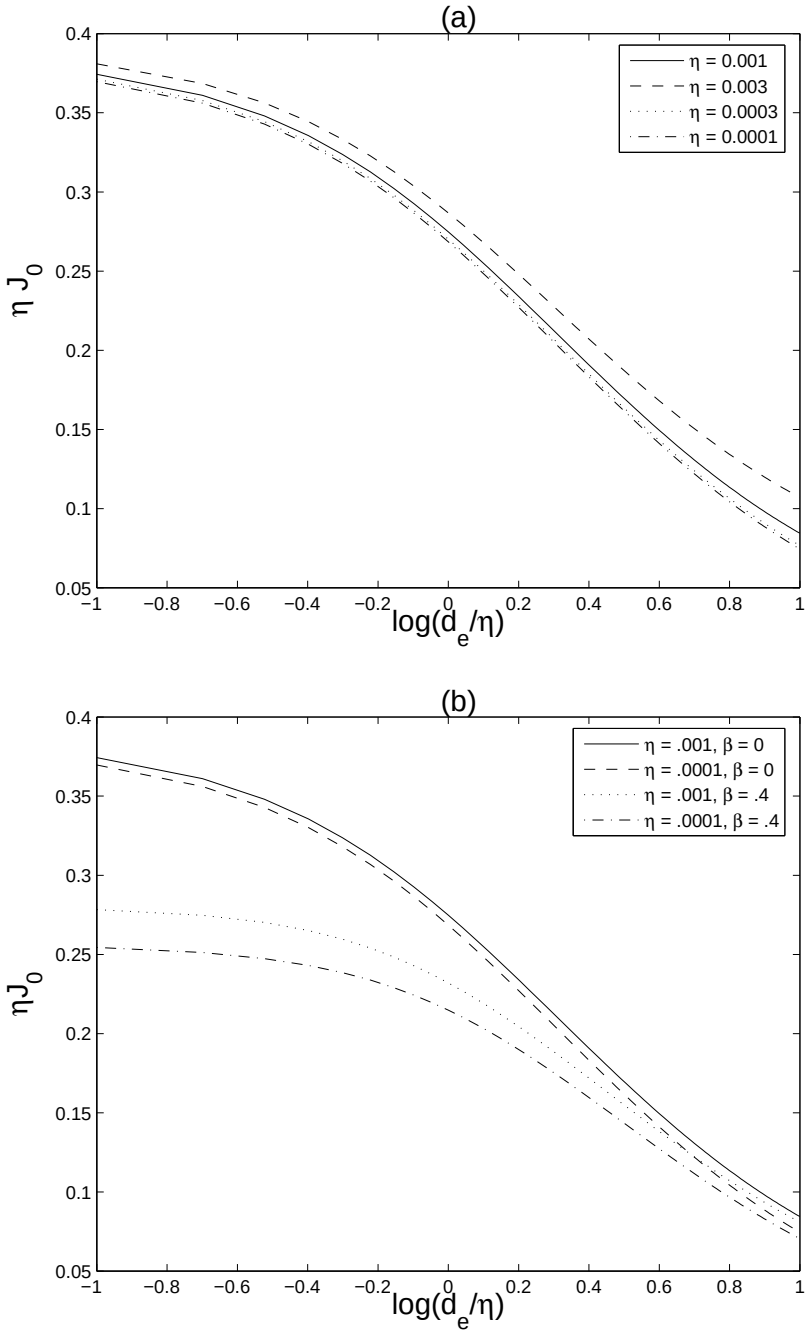

Figure 6.16: The reconnection rate, ηJ_0, versus $\log(d_e/\eta)$, (**a**) when $\beta = 0$ and (**b**) when $\beta = 0$ and $\beta = 0.4$. Figure 6.16b compares the reconnection rates between the head on ($\beta = 0$) and shear ($\beta \neq 0$) reconnections.

the strength of the magnetic fields. More specifically, numerical results show the electron inertial effects become significant when the dimensionless electron inertial skin depth satisfies $d_e > \eta$. In Figures 6.18a and b, we illustrate the reconnection rate with effects of Hall current and electron inertia. In Figure 6.18a, three plots represent the reconnection rate (ηJ_0) versus $\log(d_e/\eta)$ with $\eta = 0.001$ for various values of κ namely $\kappa = 0$, 2.5 and 5. The reconnection rate, ηJ_0, decreases by both the effects of d_i and d_e. Alternatively, Figure 6.18b illustrate the reconnection rate versus d_i for the given values of $d_e = 0.001$ and 0.01. In the case $d_e = \eta = 0.001$, the dotted line shows that the reconnection rate is reduced by Hall currents similar to the case $d_e = 0$. When $d_e = 10\eta$, the solid line shows that the dependence of the reconnection rate on the Hall current is negligible which means that reconnection rate is dominated by the electron inertial effects.

6.6 Conclusions

We have performed a detailed numerical study of the development of transient magnetic merging solutions within the framework of the generalized Ohm's law. More specifically, we have explored the role of a generalized Ohm's law incorporated within a broad class of exact $2D$ and $3D$ reconnection solutions developed analytically by Craig & Watson (2005). This analysis suggests that collisional resistivity and Hall current effects provide far more important contributions to the generalized Ohm's law than the electron inertial effects.

We constructed reconnection numerical solutions in an incompressible plasma of uniform mass density ρ using three distinct approaches. The first approach is a numerical treatment based on the influence of the Hall term. If $d_i > \eta^{1/2}$, Hall currents can significantly alter the morphology of the reconnecting planar field and generate sinusoidal wave type currents in the outer field. Both J_y and J_z continually interchange. This may be linked to the development of whistler wave modes in the

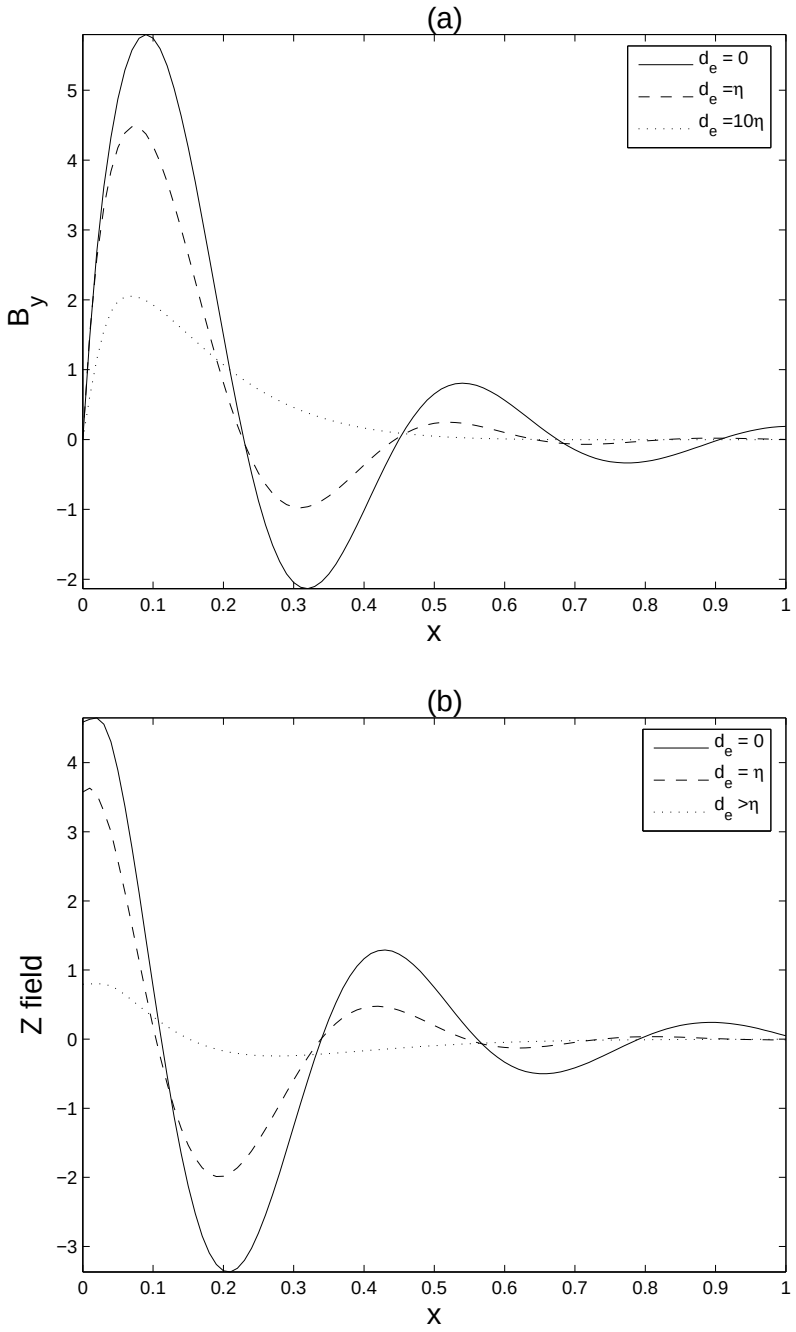

Figure 6.17: (**a**) $B_y = -\partial\psi/\partial x$ versus x and (**b**) $B_z = Z$ versus x along the line $y = 0$, for several values of d_e with a fixed κ. The solutions are for the parameter values $\alpha = 1$, $\beta = 0.4$, $\eta = 0.001$ and $\kappa = 15$. The plots indicate that oscillation in the outer field is destroyed by the electron inertial effect.

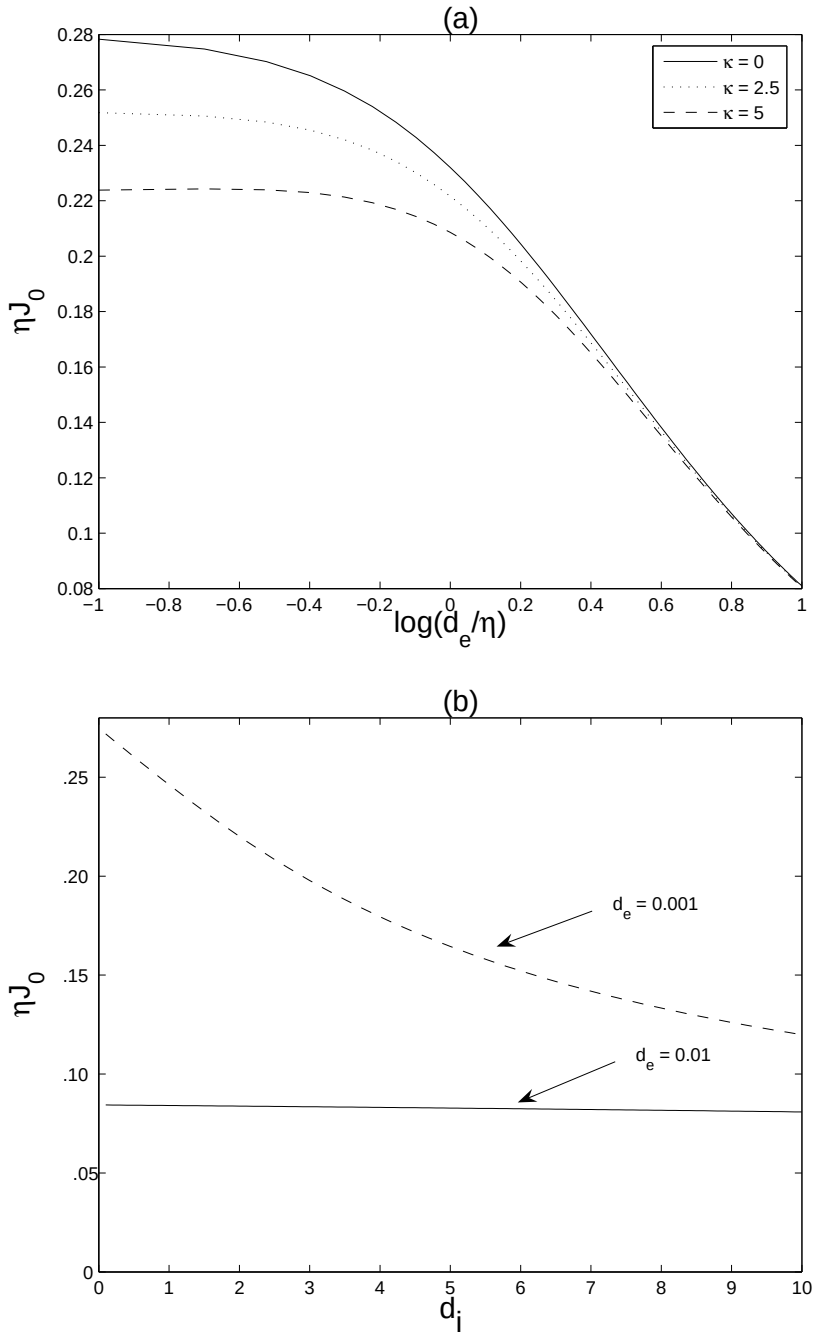

Figure 6.18: (**a**)The reconnection rate versus log (d_e/η) for several values of κ, namely $\kappa = 0$, 2.5, 5. (**b**) The reconnection rate versus d_i for the several values of d_e, namely $d_e = 0.001, 0.01$. The solutions are for the parameters values $\alpha = 1$, $\beta = 0.01$, $\eta = 0.001$ $d_i = 0.001$.

solution for large d_i (e.g. Watson & Porcelli, 2004).

Our results in §6.3.5 suggests that a new Hall-MHD hybrid length scale

$$r_s \sim d_i^{1/2} \eta^{1/4}$$

may be important for $d_i > \eta$. This appears to be a new scaling law for the current sheet width in the present of the Hall current. Also we found that there is no evidence that the current sheet length and the reconnection rate are independent of the system size. However, when axial guide fields are present, the reconnection rate may be increased or decreased depending on the symmetries of the merging problem (for instance the sign of δ).

Secondly, our calculation confirms that the electron inertial effects can significantly alter the resistive solution when

$$d_e \geq \eta,$$

but this condition may not be satisfied for collisional coronal plasmas ($\eta \simeq 10^{-14.5}$, $d_e \simeq 10^{-16}$). McClements et al. (2004) studied the relaxation of magnetic X-point collapse, taking into account the effects of resistivity and electron inertia. This paper shows that a negligible effect on the evolution of the system whenever the electron skin depth, d_e, is less than the resistivity.

Finally, we have included both Hall and inertia terms in the absence of axial guide fields: Hall effects on the planar merging solution are suppressed by the electron inertial influence. Although the reconnection rate, ηJ_0, is decreased by the effects of both d_i and d_e, the Hall current contribution is completely destroyed by the inertia effects for large values of d_e, that is $d_e > \eta$.

Chapter 7

Discussion and summary

7.1 Discussion

Magnetic reconnection provides a way to release magnetic energy in the solar corona. In the past three decades, many theoretical aspects of reconnection have been developed and observational evidence in favour of reconnection has strengthened (Sweet, 1958a, 1958b; Parker, 1957, 1963; Petschek, 1964; Syrovatskii, 1971; Craig & Henton 1995 etc.). But the problem remains as to how reconnection can occur rapidly enough to explain the explosive release of a solar flare.

In the early chapters of this thesis, we discussed two kinds of magnetic reconnection models. One model is based on incompressible magnetic merging in an open geometry that allows plasma to enter and leave the reconnection region. This approach was pursued in the classic studies of Sweet (1958) and Parker (1957, 1963). However we also consider an alternate mechanism based on X-point collapse in a closed geometry. The central aim of this thesis was to include viscosity, Hall current and inertial effects into both these reconnection mechanisms.

In Chapter 4, we considered the effects of viscosity on the X-point collapse problem. In this problem it is important to distinguish between reconnective and non-reconnective X-point disturbances. The key point is that only magnetic recon-

nection is capable of releasing energy bound up in topology into field. In the case of non-reconnective disturbances, our results imply that viscosity, in common with resistivity, can provide fast oscillatory dissipation of the excess magnetic energy. In the case of reconnective disturbances, however, the magnitude of the viscous term does become critical. For example, in the case $\nu \geq \eta$, oscillatory reconnection is suppressed and the global magnetic energy decays monotonically at a significantly slower rate than the kinetic energy. This behaviour is associated with the emergence of a new length scale—the visco-resistive scale $r_s = (\eta\nu)^{1/4}$. For both non-topological and topological disturbances our results show that the maximum energy dissipation occurs when the viscous and resistive coefficients are closely matched. The condition $\nu \geq \eta$ implies that, for comparable magnitudes of the $\mathbf{B}$ and $\mathbf{v}$ fields, the viscous force can dominate the Lorentz force at the smallest length scales, and thus prevent energy equipartition.

We extended the X-type neutral point study in Chapter 5, to explore how the reconnection rate is altered by the presence of Hall currents. Physical considerations suggest that the Hall current can significantly alter the resistive solution ($d_e = \nu = 0$) when

$$d_i > \eta^{1/2},$$

a condition which is easily satisfied for collisional coronal plasmas ($\eta \simeq 10^{-14.5}$, $d_i \simeq 10^{-6.5}$). The variation of reconnection rate ηJ_0 with magnitude of the Hall term leads to the tentative results that when $d_i \sim \eta^{1/3}$ the minimum reconnection rate is achieved, as shown in Figure 5.8. It is interesting that Fitzpatrick (2004) observed broadly similar behaviour for a different geometry. We have also emphasized that for larger Hall parameters, current localization may be significantly compromised due to the development of current corrugations aligned to the background field.

The claim that the Hall reconnection rate must be a universal constant (Shay et al. 1999, Cassak et al 2006), independent of the system size, has been questioned

(e.g. Bhattacharjee et al., 2005). Our results in Chapter 5 also provide no evidence that the reconnection rate is independent of the system size: specifically we found that normalized Hall-reconnection rate is inversely proportional to the system size (5.31).

The final chapter dealt with incompressible merging solutions in an open geometry and included the full effects of the generalized Ohm's law. By including guide fields for the axial components, we were able to confirm analytically that the normalized Hall current reconnection rate was not independent of the system size. We also found that, in the absence of axial guide fields ($\gamma = \delta = 0$), a hybrid scale namely $r_s \sim d_i^{1/2}\eta^{1/4}$ controls the width of the current sheet. Finally, with $\gamma = \delta = 0$, we found that electron inertial effects have the potential to negate the Hall current influence in the regime $d_e > \eta$.

7.2 Suggestions for further work

In this thesis, we extended previous reconnection solutions in several ways. The effects of viscosity on the X-type neutral point are encouraging. Further studies of viscous magnetic reconnection in the solar corona appear to be warranted, in view of the fact that viscous heating can significantly exceed Joule heating at the merging site. However, a more complete tensor description of the viscous term should be introduced due to the anisotropies introduced by the magnetic field (Braginskii, 1965).

Chapter 5 was devoted to the numerical study of Hall-MHD plasmas. The relationship implied by Equation (5.30) confirms that increases in the Hall coefficient enhance the decay rate of the plasma. A convincing theoretical interpretation of equation (5.30) is more difficult however, and it would be interesting to see what kind of relationship existed between the normalized decay rate and the Hall coefficient in more general circumstances. The same comment applies to the relationship between

the normalized Hall-reconnection rate and the system size dependant.

The Hall-MHD simulation code which we have developed in Chapter 5 is not efficient for $d_i > \sqrt{\eta}$ when lower values of resistivity are employed. For example, we can see that wiggles occur in the axial current due to Hall current effects in Figure 5.7 for small values of η (these curves are incomplete as instabilities can occur for large t). Thus there are still some numerical difficulties to overcome especially in the regime $d_i > \sqrt{\eta}$ where the solution is changes its character. Further work could include extensions to the code to improve accuracy and stability, perhaps by the addition of a hyper-resistivity term into the generalized Ohm's law (Fitzpatrick, 2004).

The results in Chapters 5 and 6 reveal that Hall-reconnection rates depend on the global length scale (system size) of the problem. However, the exact analytical solutions of Chapter 6 with $\beta \neq 0$ did not give a clear result for the system size dependency. We suggest further investigation of the system size dependency are appropriate given that some researchers argue that Hall current merging should be independent of the global length scale (Shay et al. 1999, Cassak et al. 2006).

In Chapter 6, we presented only a brief study of the interplay between the Hall current and electron inertial effects. Clearly, a good deal more work is needed to obtain definitive results. However, we should mention that a drawback of all our results—with the notable exception of those controlled by viscous effects—are the unrealistically high values of current density in the current sheet. It seems unlikely that this problem can be overcome using an entirely MHD approach, even one which includes a generalized Ohm's law.

Notations

Latin symbols

A	area of the diffusion region
$\mathbf{B}$	magnetic field
c	speed of light
d_i	dimensionless ion skin depth
d_e	electron inertial skin depth
e	charge of the electron
$\mathbf{E}$	electric field
$\mathbf{J}$	electric current density
J_0	axial current density at neutral point
k_B	Boltzmann's constant
K	global kinetic energy $K = \frac{1}{2}\int v^2 dv$
m_e	electron mass
m_p	proton mass
M	global magnetic energy $M = \frac{1}{2}\int B^2 dv$
n_e	electron number density
n_p	proton number density
p	total thermal pressure, $p = p_e + p_p$
r_s	scaling of the current sheet width (length scale)
S	the boundary surface

t	time
T	Temperature
T_e	electron temperature
T_p	proton temperature
$\mathbf{u}$	inflow speed to diffusion region
$\mathbf{v}$	outflow speed from diffusion region
v_A	Alfven speed, $v_A = B_c/\sqrt{4\pi\rho_c}$
W_η	Ohmic dissipation rate
W_ν	viscous dissipation rate
$\hat{\mathbf{x}}$	units vector along the x-axis
$\hat{\mathbf{y}}$	units vector along the y-axis
$\hat{\mathbf{z}}$	units vector along the z-axis
Z	axial magnetic field

Greek symbols

α	the decay rate
η	plasma resistivity or inverse Lundquist number
ν_{ep}	electron-proton Coulomb collision frequency
ν	kinematic (shear) viscosity
ρ	mass density
σ	electron conductivity
ψ	magnetic potential (flux) function
ϕ	velocity flux function
ω	oscillation frequency
$\mathbf{\Omega}$	vorticity, $\mathbf{\Omega} = \nabla \times \mathbf{v}$

Appendix A

Alternating direction implicit (ADI) method

Here we explain the semi-implicit treatment of equations (5.25) and (5.26) in Chapter 5 given as

$$\psi_{tt} = (x^2 + y^2)\nabla^2\psi + \eta\nabla^2\psi_t - d_i D Z_t, \tag{A.1}$$

$$Z_{tt} = \eta\nabla^2 Z_t + D\left(DZ + d_i\nabla^2\psi_t\right). \tag{A.2}$$

The Taylor expansion of f with respect to x is given by

$$f(x + \Delta x) = f(x) + \frac{df}{dx}|_x \Delta x + \frac{d^2 f}{dx^2}|_x \frac{(\Delta x)^2}{2} + 0((\Delta x)^3), \tag{A.3}$$

or in the discrete form,

$$f_{i+1} = f_i + \frac{df}{dx}|_i \Delta x + \frac{d^2 f}{dx^2}|_i \frac{(\Delta x)^2}{2} + 0((\Delta x)^3). \tag{A.4}$$

In our simulation code, we use the second order accuracy and central difference methods to evaluate the first and second order derivatives,

$$\frac{df}{dx}|_i = \frac{f_{i+1} - f_{i-1}}{2\Delta x}, \tag{A.5}$$

$$\frac{df^2}{dx^2}|_i = \frac{f_{i+1} + 2f_i + f_{i-1}}{(\Delta x)^2} \tag{A.6}$$

The time derivative ordinary differential equation,

$$\frac{df}{dt} = \mathcal{L}(f), \tag{A.7}$$

may also be evaluated in the similar way. The upstream differencing (Euler method) (Cheney & Kincaid, 1994) gives the following time integration scheme,

$$f^{n+1} = f^n + \Delta t \mathcal{L}(f^n). \tag{A.8}$$

The time variable equations (A.1) and (A.2) can be solved numerically by using the alternating direction implicit (ADI) method.

Here we explain the ADI treatment of the partial differential equation

$$\psi_{tt} = A\nabla^2\psi + B(\nabla^2\psi)_t. \tag{A.9}$$

We have used the similar process to solve the equations A.1 and A.2 numerically. In 2D,

$$\nabla^2\psi = \psi_{xx} + \psi_{yy}$$

where , $A = x^2 + y^2$ and $B = \eta$. Equation (A.9) is approximated by the discrete form

$$\begin{gathered}\psi^{n+1} - 2\psi^n + \psi^{n-1} = As^2(\delta_x^2 + \delta_y^2)[\theta\psi^{n+1} + (1-\theta)\psi^n] + \\ Br(\delta_x^2 + \delta_y^2)[\theta(\psi^{n+1} - \psi^n) + (1-\theta)(\psi^n - \psi^{n-1}]\end{gathered} \tag{A.10}$$

where

$$s = \frac{\Delta t}{\Delta}, \quad r = \frac{\Delta t}{\Delta^2}, \quad \Delta = \Delta x = \Delta y$$

and n is the number of time steps. Here we can apply the range of θ as $0 \leq \theta \leq 1$, depending on whether the method is explicit or implicit. As example, when $\theta = 1$, the numerical scheme is fully implicit.

Rearranging (A.10), gives

$$\begin{gathered}[1 - As^2(\delta_x^2 + \delta_y^2)\theta - Br(\delta_x^2 + \delta_y^2)\theta]\psi^{n+1} = 2\psi^n - \psi^{n-1} + As^2(\delta_x^2 + \delta_y^2)(1-\theta)\psi^n \\ + Br(\delta_x^2 + \delta_y^2)[(1-2\theta)\psi^n - (1-\theta)\psi^{n-1}.\end{gathered} \tag{A.11}$$

We calculate the two predictor steps, ψ^{n+1**} and ψ^{n+1*}, at the time steps $n + 1^{**}$ and $n + 1^*$. First we use the fully implicit ($\theta = 1$) predicted values of ψ^{n+1**} which is

$$\psi^{n+1**} = 2\psi^n - \psi^{n-1} + As^2(\delta_x^2 + \delta_y^2)\psi^n + Br(\delta_x^2 + \delta_y^2)(\psi^n - \psi^{n-1}), \tag{A.12}$$

to calculate the predicted value of ψ^{n+1*} through x-direction

$$[1 - (As^2 + Br)\theta\delta_x^2]\psi^{n+1*} = \psi^{n+1**} - (As^2 + 2Br)\theta\delta_x^2\psi^n + Br\theta\delta_x^2\psi^{n-1}. \tag{A.13}$$

Secondly, we calculate the corrected value through the y-direction using first predicted value of ψ^{n+1*}, that is

$$[1 - (As^2 + Br)\theta\delta_y^2]\psi^{n+1} = \psi^{n+1*} - (As^2 + 2Br)\theta\delta_y^2\psi^n + Br\theta\delta_y^2\psi^{n-1}. \tag{A.14}$$

When $\theta = 0$, we get the explicit method, while $\theta = 1$ gives the fully implicit method just considered. When $\theta = \frac{1}{2}$, we get the Crank-Nicolson method. This weighted average approximation is unconditionally stable for $\frac{1}{2} \leq \theta \leq 1$, but in semi implicit method, we required some conditions for stability and accuracy of the codes.

Appendix B

The numerical solutions with Pentadiagonal Systems

In Chapter 6, we find the numerical solutions of incompressible MHD equations with Hall and electron inertia effects. The equations that we solved are:

$$\frac{df}{dt} = -2\alpha f + \beta x g_x - 2\beta g + \nu f_{xx} \tag{B.1}$$

$$\frac{dW}{dt} = \beta x Z_x, \tag{B.2}$$

$$\frac{dg}{dt} = \beta x f_x + \eta g_{xx} - d_i \beta x Z_x + d_e \frac{dg_{xx}}{dt} \tag{B.3}$$

$$\frac{dZ}{dt} = \delta x f_x + \eta Z_{xx} + \beta x W_x + d_i \beta x g_{xxx} + d_e \frac{dZ_{xx}}{dt} \tag{B.4}$$

where we have introduced the Lagrangian derivative

$$\frac{d}{dt} = \frac{\partial}{\partial t} + \mathbf{v} \cdot \nabla = \frac{\partial}{\partial t} - \alpha x \frac{\partial}{\partial x}. \tag{B.5}$$

The form

$$\left(\frac{\partial}{\partial t} - \alpha x \frac{\partial}{\partial t} \right) U = r \tag{B.6}$$

represents the first two equations which can be solved explicitly by using the "Russian method" (Heerikhuisen, 2002; Appendix A). Here $U = (f\ ,\ W)$ and $r = (r_1\ ,\ \ r_2)$ where r_i and r_2 represent the right hand side of (B.1) and (B.2) respectively.

The (B.3) and (B.4) are the third order partial differential equations that can be solved by a semi-implicit method. Five banded matrices often occur in solving third order partial differential equations. The principles illustrated by procedure called "penta" can be applied to matrices that have up to five bands of nonzero elements. The method to solve equations (B.3) and (B.4) by using pentadiagonal system is explained in next the section.

Pentadiagonal Systems

A procedure called *penta* is given here to solve the five-diagonal system (Cheney & Kincaid, 1994): We have involved in procedure "pentadiagonal system" to solve equations (B.3) and (B.4) numerically.

$$\begin{pmatrix}
d_1 & c_1 & f_1 & & & & & & & \\
a_1 & d_2 & c_2 & f_2 & & & & & & \\
e_1 & a_2 & d_3 & c_3 & f_3 & & & & & \\
 & e_2 & a_3 & d_4 & c_4 & f_4 & & & & \\
 & & \ddots & \ddots & \ddots & \ddots & \ddots & & & \\
 & & & e_{i-2} & a_{i-1} & d_i & c_i & f_i & & \\
 & & & & \ddots & \ddots & \ddots & \ddots & \ddots & \\
 & & & & & e_{n-4} & a_{n-3} & d_{n-2} & c_{n-2} & f_{n-2} \\
 & & & & & & e_{n-3} & a_{n-2} & d_{n-1} & c_{n-1} \\
 & & & & & & & e_{n-2} & a_{n-1} & d_n
\end{pmatrix}
\begin{pmatrix} x_1 \\ x_2 \\ x_3 \\ x_4 \\ \vdots \\ x_i \\ \vdots \\ x_{n-2} \\ x_{n-1} \\ x_n \end{pmatrix}
=
\begin{pmatrix} b_1 \\ b_2 \\ b_3 \\ b_4 \\ \vdots \\ b_i \\ \vdots \\ b_{n-2} \\ b_{n-1} \\ b_n \end{pmatrix}$$

procedure penta $(n, (e_i), (a_i), (d_i), (c_i), (f_i), (b_i), (x_i))$
real array $(e_i)_n, (a_i)_n, (d_i)_n (c_i)_n, (f_i)_n, (b_i)_n, (x_i)_n$
integer i, n
real *xmult*
for i = 2 **to** n-1 **do**
    $xmult \leftarrow a_{i-1}/d_{i-1}$
    $d_i \leftarrow d_i$ - $(xmult)c_{i-1}$
    $c_i \leftarrow c_i - (xmult)f_{i-1}$
    $b_i \leftarrow b_i - (xmult)b_{i-1}$
    $xmult \leftarrow e_{i-1}/d_{i-1}$
    $a_i \leftarrow a_i - (xmult)c_{i-1}$
    $b_{i+1} \leftarrow b_{i+1} - (xmult)b_{i-1}$
end do
$xmult \leftarrow a_{n-1}/d_{n-1}$
$d_n \leftarrow d_n - (xmult)c_{n-1}$
$x_n \leftarrow (b_n - (xmult)b_{n-1})/d_n$
$x_{n-1} \leftarrow (b_{n-1} - c_{n-1}x_n)/d_{n-1}$
for i = n-2 **to** 1 **step** -1 **do**
    $x_i \leftarrow (b_i - f_i x_{i+2} - c_i x_{i+1})/d_i$
end do
end procedure *penta*

B.1 The solution of equation (B.3)

The first, second and third order directional derivatives of g are given by

$$\frac{dg}{dx}|_i = \frac{g_{i+1} - g_{i-1}}{2\Delta x}, \tag{B.7}$$

$$\frac{dg^2}{dx^2}|_i = \frac{g_{i+1} + 2g_i + g_{i-1}}{(\Delta x)^2} \tag{B.8}$$

$$\frac{dg^3}{dx^3}|_i = \frac{g_{j+2} - 2g_{j+1} + 2g_{j-1} - g_{j-2}}{2(\Delta x)^3} \tag{B.9}$$

Similarly, first order time derivative of g is

$$\frac{dg}{dt}|_n = \frac{g^{n+1} - g^{n-1}}{2\Delta t}. \tag{B.10}$$

The semi-implicit discrete form of the partial differential equation (B.3) can be written as

$$e(i-2)g_{i-2}^{n+\theta} + a(i-1)g_{i-1}^{n+\theta} + d(i)g_i^{n+\theta} + c(i)g_{i+1}^{n+\theta} + f(i)g_{i+2}^{n+\theta} = b \tag{B.11}$$

where $n+\theta$ is time step. The elements of the penta diagonal system e, a, d, e, f and b are given by

$$\begin{aligned}
x &= i\Delta x, \\
e(i-2) &= \theta\alpha x d_e \Delta t/2, \\
a(i-1) &= d_e\Delta x - \theta\alpha x d_e \Delta t - \theta\alpha x \Delta t(\Delta x)^2/2 + \theta\eta\Delta t\Delta x, \\
d(i) &= -2\Delta x d_e - (\Delta x)^3 - 2\theta\eta\Delta t\Delta x, \\
c(i) &= \Delta x d_e + \theta\alpha x\Delta t d_e + \theta\alpha x(\Delta x)^2\Delta t/2 + \theta\eta\Delta t\Delta x, \\
f(i) &= -\theta\alpha x d_e \Delta t/2, \\
b(i) &= (gb(i+2) - 2gb(i) + gb(i-1))(d_e\Delta x - \eta\Delta x\Delta t(1-\theta)) - (\Delta)^3 gb(i) \\
&\quad -\alpha x(\Delta^2)\Delta t(1-\theta)(gb(i+1) - gb(i-1))/2 + d_e\alpha x\Delta t(1-\theta)(gb(i+2) \\
&\quad -2gb(i+1) + 2gb(i-1) - gb(i-2))/2 - \beta x(1-\theta)(\Delta)^2\Delta t(f(i+1) \\
&\quad -f(i-1))/2 + d_i\beta x(\Delta)^2\Delta t(z(i+1) - z(i-1))/2 - \beta.
\end{aligned}$$

The solution $gn(i)$ is given by

$$gn(i) = (b(i) - f(i)gn(i+2) - c(i)gn(i+1))/d(i).$$

Here, $gb = g^n$, $gn = g^{n+\theta}$, where $0 \leq \theta \leq 1$. The superscript represents the time steps.

B.2 The solution of equation (B.4)

It can be applied the similar method in B.1 to solve the partial differential equation (B.4). The elements of the penta diagonal system, e, a, d, e, f and b are given by

$$x = i\Delta x,$$

$$
\begin{aligned}
e(i-2) &= \theta\alpha x\Delta t d_e/2, \\
a(i-1) &= \Delta d_e - \theta\alpha x\Delta t d_e - \theta\alpha x\Delta t(\Delta x)^2/2 + \theta\eta\Delta t\Delta x, \\
d(i) &= -2\Delta x d_e - (\Delta x)^3 - 2\theta\eta\Delta t\Delta x, \\
c(i) &= \Delta x d_e + \theta\alpha x\Delta t d_e + \theta\alpha x(\Delta x)^2\Delta t/2 + \theta\eta\Delta t\Delta x, \\
f(i) &= -\theta\alpha x\Delta t d_e/2, \\
b(i) &= (zb(i+1) - 2zb(i) + zb(i-1))(d_e\Delta x - \eta\Delta x\Delta t(1-\theta)) - (\Delta x)^3 zb(i) \\
&\quad -\alpha x(\Delta x)^3\Delta t(1-\theta)(zb(i+1) - zb(i-1))/2 + d_e\alpha x\Delta t(1-\theta)(zb(i-2) \\
&\quad -2zb(i+1) + 2zb(i-1) - zb(i-2))/2 - \beta x(\Delta)^2\Delta t(1-\theta)(w(i+1) \\
&\quad -w(i-1))/2.
\end{aligned}
$$

The solution $zn(i)$ is given by

$$zn(i) = (b(i) - f(i)zn(i+2) - c(i)zn(i+1))/d(i),$$

Here, $zb = z^n$ and $zn = z^{n+\theta}$, where $0 \leq \theta \leq 1$. The superscript represent the time steps.

References

[1] Asai, A., Yokoyama, T., Shimojo, M. & Shibata, K., "Downflow motions associated with impulsive nonthermal emissions observed in the 2002 July 23 solar flare." *Astrophysical Journal*, vol. 605, issue 1, p. L77-L80 (2004).

[2] Bentley, R.D & Mariska, J.T., Magnetic reconnection in the solar atmosphere. San Francisco, California: Astronomical Society of the Pacific (1996).

[3] Bhattacharjee, A., Germaschewski, K. and Ng, C.S., "Current singularities: Drivers of impulsive reconnection." *Physices of plasmas*, vol. 12, issue 4, p. 042305 (2005).

[4] Bhattacharjee, A., Ma, Z.W. & Wang, X., "Impulsive reconnection dynamics in collisionless laboratory and space plasmas." *Journal of Geophysical Research*, vol. 104, issue A7, p. 14543-14570 (1999).

[5] Birn, J., Drake, J.F., Shay, M.A., Rogers, B.N., Denton, R.E., Hesse, M., Kuznetsova, M., Ma, Z.W., Bhattacharjee, A., Otto, A., Pritchett, P.L., "Geospace Environmental Modeling (GEM) magnetic reconnection challenge." *Journal of Geophysical Research*, vol. 106, issue A3, p. 3715-3720 (2001).

[6] Birn, J. & Hesse, M., "Geospace Environment Modeling (GEM) magnetic reconnection challenge: Resistive tearing, anisotropic pressure and hall effects." *Journal of Geophysical Research*, vol. 106, issue A3, p. 3737-3750 (2001).

[7] Biskamp, D. & Welter, H., "Coalescence of magnetic islands." *Physical Review Letters*, vol. 44, p. 1069-1072 (1980).

[8] Biskamp, D., Magnetic reconnection in plasmas. Cambridge: Cambridge University press (2000).

[9] Braginskii, S.I.,"Transport processes in a plasma." *Reviews of Plasmas Physics.* 1, 205-311, (1965).

[10] Chapman, S. & Kendall, P.C., "Liquid instability and energy transformation near a magnetic line: A soluble non-linear hydromagnetic problem. *Proceedings of the Royal Society London*, 271, 435-448, (1963).

[11] Cassak, P.A., Drake, J.F. & Shay, M.A., "A model for spontaneous onset of fast magnetic reconnection." *Astrophysical Journal*, volume 644,issue 2, p L145-L148, (2006).

[12] Chapman, S. & Kendall, P.C., " Comment on 'Some exact solutions of the magnetohydrodynamics'." *Physics of Fluids*, 9, 2306-2307, (1966).

[13] Cheney, W. & Kincaid, D., Numerical mathematics and computing. Cole Publishing Company: Pacific Grove, California (1994).

[14] Choudhuri, A.R., The physics of the flud plasmas. United Kingdom at the University press: Cambridge (1998).

[15] Craig, I.J.D., "Current sheet formation and dissipation in general X-point topologies." *Astronomy and Asrophysics*, vol. 283, p. 331-338 (1994).

[16] Craig, I.J.D., "A reconnection model for the distribution of flare energies." *Solar Physics*, p. 202:109-115, (2001).

[17] Craig, I.J.D. & Fabling, R.b., "Exact solutions for steady-state spine and fan magnetic reconnection." *Astrophsical Journal*, 462, p. 969-976, (1996).

[18] Craig, I.J.D., Fabling, R.B. & Watson, P.G. "The power output of spine and fan magnetic reconnection solutions." *Astrophsical Journal*, volume 485,p 383-388, (1997).

[19] Craig, I.J.D. & Fruit, G., "Wave energy dissipation by phase mixing in magnetic coronal plasmas" *Astronomy and Astrophysics*, vol. 440, issue 1, September II, p. 357-366, (2005).

[20] Craig, I.J.D., Heerikhuisen, J. & Watson, P.G., "Hall current effects in dynamic magnetic reconnection solution." *Physics of Plasmas*, vol. 10, No. 8, p. 3120 (2003).

[21] Craig, I.J.D. & Henton, S.M., "Exact solutions for steady state incompressible magnetic reconnection." *Astrophysical Journal*, vol.450, p. 280 (1995).

[22] Craig, I.J.D.& Litvinenko, Y.E., "Current singularities in planer magnetic X points of finite compressibility." *Physics of Plasmas*, vol. 12, issue 3, p. 032301 (2005).

[23] Craig, I.J.D., Litvinenko, Y.E. & Senanayake, T, "Viscous effects in planar magnetic X-point reconnection." *Astronomy and Astrophysics*, vol. 433, issue 3, April III, pp.1139-1143 (2005).

[24] Craig, I.J.D & McClymont, A.N., "Shear wave dissipation in planar magnetic X-points." *Astrophsical Journal*, vol. 481, p. 996-1003, (1997).

[25] Craig, I.J.D & McClymont, A.N., "Dynamic magnetic reconnection at an X-type neutral point." *Astrophysical Journal*, Part 2 - Letters (ISSN 0004-637X), vol. 371, April 10, p. L41-L44 (1991).

[26] Craig, I.J.D & McClymont, A.N., "Linear theory of fast reconnection at an X-type neutral point." *Astrophysical Journal*, Part 1 (ISSN 0004-637X), vol. 405, no. 1, p. 207-215 (1993).

[27] Craig, I.J.D. & McClymont, A.N., "Magnetic energy release in dynamic fan reconnection models." *Astrophysical Journal*, vol. 510, p. 1045-1052 (1999).

[28] Craig, I.J.D. & Watson, P.G., "Fast dynamic reconnection at X-type neutral points." *Astrophysical Journal*, Part 1 (ISSN 0004-637X), vol. 393, no. 1, July 1, p. 385-395 (1992).

[29] Craig, I.J.D. & Watson, P.G., "Flare-like energy release by flux pile-up reconnection." *Solar Physics*, volume 191, p. 359-379, (2000).

[30] Craig, I.J.D. & Watson, P.G., "Optimized magnetic reconnection solutions in three dimensions." *Solar Physics*, volume 194, p. 251-268, (2000).

[31] Craig, I.J.D.& Watson, P.G., "Magnetic reconnection solutions based on a generalized Ohm's law." *Solar Physics*, vol. 214, issue 1, p. 131-150 (2003).

[32] Craig, I.J.D. & Watson, P.G., "Exact models for Hall current reconnection with axial guide fields." *Physics of Plasmas*, vol. 12, issue 1, p. 012306 (2005).

[33] Cravens T.E., Physics of solar system plasmas. Cambridge: Atmospheric and space science series (1997).

[34] Davies, B., Integral tranforms and their applications. New York: Springer, (2002).

[35] Dorelli, J.C., "Effects of Hall electric fields on the saturation of forced antiparallel magnetic field merging." *Physics of Plasmas*, vol. 10, No. 8, p. 3309 (2003).

[36] Dugey, J.W., "Conditions for the occurrence of electrical discharges in astrophysical system." *Phil. Mag* 44, p. 725-738, (1953).

[37] Dugey, J.W., "The neutral point discharge theory of solar frares. A reply to cowling's criticism." *Electromagnetic phenomena in cosmical physics.*" IAU Symp. 6, ed. B. Lehnert (Cambridge University Press, Cambridge), (1958).

[38] Fabling, R.B. & Craig, I.J.D., "Exact solution for steady-state planar magnetic reconnection in an incompressible viscous plasma." *Physics of Plasmas*, 3, p. 2243-2247, (1996).

[39] Fabling, R.B., Exact magnetic reconnection solutions in three dimensions. Ph.D. thesis, University of Waikato (1997).

[40] Fitzpatrick, R., "Scaling of forced magnetic reconnection in the Hall-magnetohydrodynamic Taylor problem." *Physics of Plasmas*, vol. 11, No. 3, p. 937 (2004).

[41] Foukal, P.V., Solar astrophysics. Wiley-vch: Verlag Gmbh & Co. KGaA (2004).

[42] Giovanelli, R.G., " A theory of chromospheric flares." *Nature*, 158, 81-82, (1946).

[43] Golub, L.& Pasachoff, M.J., Solar corona. Cambridge: Cambridge University press (1997).

[44] Gordon D.H., Laboratory for astronomy and solar physics NASA/Goddard Space Flight Center. http://hesperia.gsfc.nasa.gov/sftheory (viewed 15^{th} September 2004).

[45] Hassam, A.B., "Reconnection of stressed magnetic fields." *Astrophysical Journal*, Part 1 (ISSN 0004-637X), vol. 399, no. 1, p. 159-163 (1992).

[46] Heerikhuisen, J., Coronal magnetic energy release by current sheet reconnection. Ph.D. thesis, University of Waikato (2002).

[47] Hollweg, J.V., "Viscosity and the Chew-Goldberger-Low equations in the solar corona." *Astrophysical Journal*, Part 1 (ISSN 0004-637X), vol. 306, July 15, p. 730-739 (1986).

[48] Hollweg, J.V., "Resonance absorption of magnetohydrodynamic surface waves: viscous effects." *Astrophsical Journal*, 320:875-883, (1987).

[49] Hoyle, F., Some recent researches in solar physics. Cambridge University Press, Cambridge (1949).

[50] Knoll, D.A. & Chacon, L., "Coalescence of magnetic islands in the low-resistivity, Hall-MHD regime." *Physical Review Letters*, vol. 96, issue 13, id. 135001 (2006).

[51] Leon, G. & Jay, M.P., The Solar Corona. United Kingdom at the University press, Cambridge (1997).

[52] Litvinenko, Y.E. & Craig, I.J.D., "Flare energy release by flux pile-up magnetic reconnection in a turbulent current Sheet." *Astrophysical Journal*, vol. 544, issue 2, p. 1101-1107, (2000).

[53] Litvinenko, Y.E. & Craig, I.J.D., "Magnetic energy release in flux pile-up merging." *Solar Physics*, vol. 189, p. 315-329, (1999).

[54] Loughhead, R.E., Bray, R.J. & Tappere, E.J. "Improved observations of sunspot umbral dots." *Astronomy and Astrophysics,* vol. 79, p. 128-131, (1979).

[55] McClements, K.G., Thyagaraja, A., Ayed, N.B., Fletcher, L., "Electron inertial effects on rapid energy redistribution at magnetic X-points." *Astrophysical Journal*, vol. 609, issue 1, p. 423-438 (2004).

[56] McClymont, A.N. & Craig, I.J.D., "Dynamical finite-amplitude magnetic reconnection at an X-type neutral point." *Astrophysical Journal*, vol. 466, p. 487 (1996).

[57] McKenzie, D.E., "Supra-arcade downflows in long-duration solar flare events." *Solar Physics*, vol. 195, issue 2, p. 381-399 (2000).

[58] McKenzie, D.E. & Hudson, H.S.,"X-ray observations of motions and structure above a solar flare arcade." *Astrophysical Journal*, vol. 519, issue 1, p. L93-L96 (1999).

[59] McLaughlin, J.A. & Hood, A.W., "MHD wave propagation in the neighbourhood of a two-dimensional null point." *Astronomy and Astrophysics*, vol. 420, p. 1129-1140 (2004).

[60] Micheel, S., The Sun: An introduction astronomy and astrophysics library. New York (1989).

[61] Nelkon, M. & Parker, P., Advanced level physics. London: Heinemann Educational books (1984).

[62] Ofman, L., Morrison, P.J. & Steinolfson, R. S., "Magnetic reconnection at stressed X-type neutral points." *Astrophysical Journal*, vol. 417, p. 748 (1993).

[63] Park, W., Monticello, D.A. & White, R.B., "Reconnection rate of magnetic fields including the effects of viscosity." *Physics of Fluids*, 27, 137-149, (1984).

[64] Parker, E.N., "Sweet's mechanism for merging magnetic fields in conducting fluids." *Journal of Geophysical Research*, 62, p. 509-520, (1957).

[65] Parker, E.N., "The solar flare phenomenon and theory of reconnection and annihilation of magnetic fields." *Astrophysical Journal Supplement*, 8, 177-211, (1963).

[66] Parker, E.N., "Comments on the reconnection rate of magnetic fields." *Physics of Plasmas*, vol. 9, p. 49-63, (1973).

[67] Parker, E.N., Spontaneous current sheets in magnetic fields. Oxford University Press (1994).

[68] Petschek, H.E.,"Magnetic field annihilation." *Physics of Solar Flares*, ed. W.N. Hess (NASA SP-50, Washington DC) p. 425-439, (1964).

[69] Pontin, D.I. & Craig, I.J.D., "Dynamic three-dimensional reconnection in a separator geometry with two null points." *Astrophysical Journal*, volume 642, issue 1, p. 568-578 (2006).

[70] Priest, E.R., Solar Magnetohydrodynamics. Dordrecht, Holland; Boston: D. Reidel Pub. Co.; Hingham, MA (1984).

[71] Priest, E.R. & Forbes, T., Magnetic reconnection: MHD theory and applications. Cambridge: New York : Cambridge University Press, (2000).

[72] Physicsweb (1999), New light on the solar corona. http://physicsweb.org/ articles/news/3/8/5, (viewed 25^{th} July 2006).

[73] Richtmyer, R.D. & Morton, K.W., Difference methods for initial-value problems. New York: Interscience (1967).

[74] Rickard, G.J. & Craig, I.J.D., "Fast magnetic reconnection and the coalescence instability." *Physics of Fluids*, vol. 5, no. 3, p. 956-964 (1993).

[75] Roberts, P.H., An Introduction to magnetohydrodynamics. Longmans, White Friars press, London (1967).

[76] Senanayake, T. & Craig, I.J.D., "Hall effects on dynamic magnetic reconnection at an X-type neutral point" *Astronomy and Astrophysics*, vol. 451, issue 3, June I , p. 1117-1124 (2006).

[77] Shay, M.A., Drake, J.F., Rogers, B.N. & Denton, R.E., "The scalling of collisionless, magnetic reconnection for large system." *Geophysical Research Letters*, vol. 26, issue 14, p. 2163-2166 (1999).

[78] Sonnerup, B.U.Ö., "Magnetic field reconnection in a highly conducting incompressible fluid." *Plasma Physics*, 4, p. 161-174, (1970).

[79] Sonnerup, B.U.Ö. & Priest, E.R., "Resistive MHD stagnation-point flows at a current sheet." *Plasma Physics*, 14, 283-294, (1975).

[80] Spiegel, M.R., Schaum's outline of theory and problems of Fourier analysis. New York: McGraw-Hill (1974).

[81] Spitzer, L., Physics of fully ionized gases. New York: John Wiley & Sons (1962).

[82] Sweet, P.A., " The neutral point theory of solar flares." *Electromagnetic Phenomena in Cosmical Physics*, IAU Symp. 6, ed. B. Lehnert (Cambridge Univesity Press, London) p. 123-134, (1958a).

[83] Sweet, P.A.,"The production of high-energy particles in solar flares." *Nuovo Cimento Supplement*, 8, Ser X, 188-196, (1958b).

[84] Syrovatsky, S.I., "Formation of currentsheets in a plasma with a frozen-in strong magnetic field." *Soviet Physics*, JETP 33, p. 933-940, (1971).

[85] Uberoi, M.S,, "Some exact solutions of the magnetohydrodynamics" *Physics of Fluids*, 6, 1379-1381, (1963).

[86] Uberoi, M.S,, "Reply to comments by S. Chapman and P.C. Kendall, *Physics of Fluids*, 9, 2307, (1966).

[87] Velikovich, A.L., Whitney, K.G., Thornhill, J.W., "A role for electron viscosity in plasma shock heating" *Physics of Plasmas*, vol. 8, issue 10, p. 4524-4533, (2001).

[88] Watson, P.G., The relaxation of perturbed magnetic X-type neutral points. MSc dissertation, University of Waikato (1990).

[89] Watson, P.G.& Craig, I.J.D., "Fast magnetic reconnection via jets and current microsheets." *Astrophysical Journal*, vol. 590, issue 1, p. L57-L60 (2003).

[90] Watson, P.G. & Porcelli, F., "Exact steady state reconnection solutions in weakly collisional plasmas." *Astrophysical Journal*, 617, p. 1353-1360, (2004).

[91] Whitney, K.G., Thornhill, J.W., Velikovich, A.L., Apruzese, J.P., Deeney, C., Coverdale, C.A., "Modeling shock wave generation in olliding plasmas." http://flux.aps.org/meetings/YR00/DPP00/abs/S160106. (viewed 25^{th} July 2006).